Interactions of lipid membranes with chitosan and epsilon-toxin: a biophysical approach

Submitted by Skye Claire May Marshall to the University of Exeter

as a thesis for the degree of

Doctor of Philosophy in Physics

In May 2021

Signature: …………………………………………………………………

This thesis is dedicated to my mum,

Helen Marshall.

Your consistent support is the reason this exists.

<u>Acknowledgements</u>

I would like to thank:

Dr. Peter Petrov for being a stable rock throughout the years of this PhD. For his enthusiastic science conversations and teachings, funny stories (told through chuckles), pastoral listening ear, constructive feedback and quality checking my presentations and thesis drafts. And Professor Peter Winlove for science lessons and for listening when I was struggling.

My mum, Helen Marshall, who was instrumental in providing enthusiastic and positive feedback, to the point where I would look forward to sending my work to her. There is no underestimating positivity. She is the most wise and intelligent person I know, picking up on all the in-depth science whilst maintaining the bigger picture in her head, so she could read my drafts and have effective discussions about it with me.

Dr. Beth McGill for being a brilliant travel partner, lab companion and housemate. For being a mum in the week and a drunk in the streets. For laughing along through her extreme anxiety of missing flights, losing luggage, bending rules, and still laughing through the fear of the arthropods I so earnestly bring to her. She was an essential helper in lab experiments that required more hands than I own.

Dr. Monika Bokori-Brown for providing stocks of epsilon toxin, for guidance on the time it takes to produce a protein in the lab, saving me from some of the many rabbit holes I ventured into. And for being an enthusiastic world expert in biological toxins.

Dr. Bob-Dan Lechner for Langmuir trough and x-ray lessons and for being able to work the longest shifts at the synchrotrons. For spontaneous bursts of song and for being enthusiastic about seeing Glasgow (despite the freezing rain) and visiting my island.

Dr. Fay Manning for being an excellent leader in the Women in Physics group and an inspiration in being brave. Where a quiet or feminine voice is quickly put down or interrupted, she is unafraid to ask questions and be assertive. She works hard to maintain a mental barrier against negative societal messaging, despite being fully cognisant of unfair and offensive behaviour by others. It is a daily decision to be brave, and Fay's example makes the decision easier. She also contributed greatly through scientific discussion and consultation over schematic figures.

Abstract

Cell membranes function as physical barriers, as well as interactive interfaces, between the highly regulated and controlled environment inside the cell and the rapidly changing and potentially harmful environment outside the cell. The physical arrangement of lipids has a large contribution to the physical properties of the membrane, which in turn affect its interaction with external influences. This thesis aims to investigate the effects of two exogenous, membrane-active, biological substances on cell membranes and membrane models.

Epsilon toxin (Etx) is a potent cytolytic agent which acts by forming pores in a host cell membrane, causing cell lysis. The mechanism of action of pore-forming toxins can be divided into three stages (binding, oligomerisation, and pore-formation) the details of which are not well known for Etx. This project aims to characterise the interaction of Etx with lipid membranes by assessing toxicity of mutated Etx variants (Y42A, Y43A, and H162A) at each stage of action.

Chitosan is a polysaccharide with many unique applications involving cell membranes. It is known to affect the membrane but does not form pores, the interaction instead being thought to be associated with the physical state of the lipids within the membrane. This action was investigated by observing the changes to mammalian cell representative mixtures of lipid monolayers in a Langmuir trough, firstly by measuring surface pressure changes, then by measuring x-ray reflectivity and diffraction.

The results of Etx action on cell membranes have shed light on the complexity of binding mechanisms that Etx can employ in RBCs. We found that the H162A variant, previously thought to be non-toxic, became active at physiological temperature and we explain this through discussion of thermal fluctuations in the lipid environment. The observations of chitosan and lipid monolayers showed that it is strongly attracted to the inner leaflet lipid mixture, through electrostatic, H-bonding and hydrophobic interactions, disrupting lateral order and stiffening the monolayer. This could have medical implications in cases where chitosan is used as a medicine or as a drug delivery system to cells, where the strong attraction to the inner leaflet may cause chitosan to penetrate through the outer leaflet.

Contents

List of figures

1 <u>Introduction</u>

1.1 Thesis outline

This PhD looks at interactions of biomolecules and lipid membranes in two parts. The first part will focus on the pore forming protein, epsilon-toxin (Etx), and the second part on the polysaccharide, chitosan. These two molecules were chosen due to the following rational: The initial approach to the project was to look at a pore-forming protein released by the *Entamoeba histolytica* pathogen, however, it proved more efficient to enter a collaboration looking at the Etx pore-forming protein instead. In order to still address *E. histolytica* virulence, chitosan was chosen as it is a central component to the pathogen's life-cycle.

1.2 Aims and objectives

The overall aim of this project was to take a biophysical approach to investigate the interactions of lipid membranes with two exogenous membrane-active biomolecules: Etx and chitosan. The biological effects of Etx on red blood cells (RBCs) were characterised using microscopy and western blots and the physical event of pore-formation recorded using electrophysiology. The physics of chitosan interactions with lipid monolayers was characterised using viscoelasticity measurements and x-ray analysis. The specific thesis objectives were:

1) To examine haemolytic effects of Etx with RBCs

2) To investigate the importance of selected amino acids in the three stages of Etx pore-formation in RBCs

3) To characterise chitosan induced changes in surface pressure and viscoelasticity of lipid monolayers, using a Langmuir trough

4) To obtain structural information of the interaction of lipid monolayers with chitosan using x-ray techniques

1.3 Background

1.3.1 The cell membrane

Cell membranes separate and connect the life-forming infrastructure that make up a cell from the external environment. In other words, they are both a physical boundary and an interactive interface. Therefore, their structure and functions are highly

regulated and important for maintaining life. It is now recognised that the membrane plays a key role in a large number of important functions such as communication, transport and metabolism [1]. As the membrane is an important line of defence against foreign substances invading the cell, it is a central area to examine in relation to infectious disease studies. Many disease-causing pathogens release toxins that target the cell membranes of the host they have infected.

1.3.2 Structure of membranes

Cell membranes are complex structures consisting of a bilayer of phospholipids, interspersed with various membrane proteins and cholesterol, and a cytoskeleton just beneath. Singer and Nicholson (1972) proposed the fluid mosaic model of a membrane bilayer which describes the free lateral diffusion of proteins and phospholipids within the membrane [2].

A phospholipid is made up of a hydrophilic headgroup and a hydrophobic acyl chains (tails) region, causing the tails to face inward and the headgroups to face out from the bilayer. Membrane proteins perform multiple functions and can be transmembrane or attached to either the inner leaflet (IL) or outer leaflet (OL). The cytoskeleton is the network of protein filaments that maintains the mechanical integrity of the cell. Although this is not part of the membrane, it has been shown to affect its functions, such as endocytosis, rigidity and bending [3].

There are four main types of lipids found in mammalian cells. Looking at the human RBC, the most common lipids are phosphatidylethanolamine (PE) (~18 %), phosphatidylcholine (PC) (~17 %), sphingomyelin (SM) (~18 %), and phosphatidylserine (PS) (~7 %), together with cholesterol (~23 %) [4]. The complexity of membrane structure is further increased by the asymmetry of the lipid species between the IL and the OL. The human RBC OL is comprised mainly of SM and PC, whereas the IL major lipid species are PE and PS [5] (Figure 1.1).

Highlighting the importance of specific lipid composition, there is an enzyme, flippase, which maintains the required leaflet asymmetry and an enzyme, scramblase, which moves PS to the outer leaflet to activate blood clotting factors [6]. Therefore, it is important that PS stays on the IL unless a clot is needed.
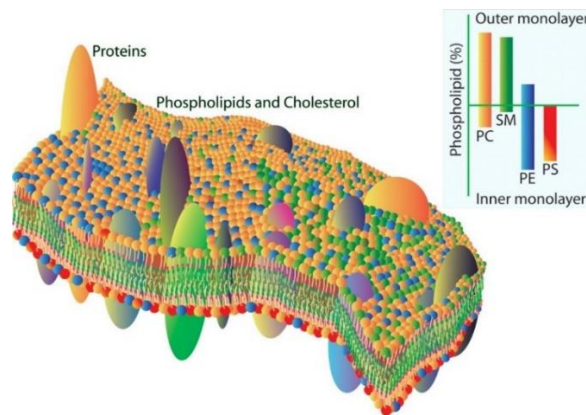
Figure 1.1 Complexity of the RBC membrane. Inset describes the contributions of the four main lipids to the IL and OL. Asymmetry of the leaflets can also be seen within the main image by looking at the headgroup colours [6].

1.3.3 Chemistry of lipids

Phospholipids are the most common form of lipid, and they have a general structure of two non-polar fatty acid chains, connected by esterification to a polar headgroup, consisting of a glycerol backbone esterified to a phosphate which is esterified to a small molecule 'base', as schematically shown in Figure 1.2 [7].
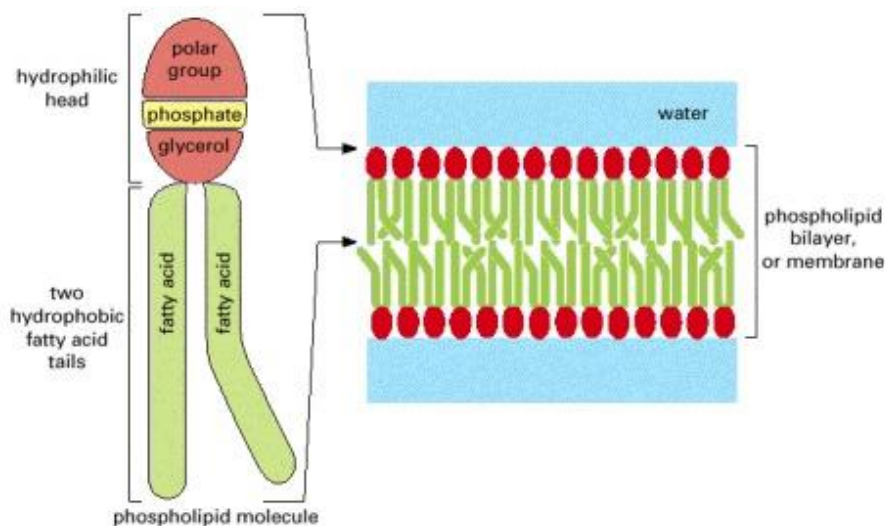
Figure 1.2 General structure of a phospholipid (left) and the natural orientation in water due to hydrophilic and hydrophobic regions (right) [4].

Fatty acids which are esterified (where the OH group is lost in order to bind to the lipid backbone) are called acyl chains. Acyl chains in mammalian lipids can differ in the number of carbons in the chain (16 to 22) and in level of saturation (containing up to six double bonds) [6]. This study has mainly used lipids with saturated palmitic acid which is a commonly found acyl chain in animal cell membranes, with 16 carbons and no double bonds (16:0) [8].

Saturated lipids are used preferably over unsaturated lipids in the laboratory because they are less susceptible to oxidation. Unsaturated acyl-chains on phospholipids are vulnerable to oxidation (Kuypers 2007). When oxidized the acyl chain has a different structure, causing a change to local lipid packing (Kuypers 2007).

The phosphate is a large group which is negatively charged at neutral pH [7]. A differentiating factor between headgroups is the base attached to the phosphate, such as choline (in PC), or ethanolamine (in PE) (these bases contain the positively charged nitrogen). The polarity of headgroups is what causes them to be hydrophilic (Figure 1.3).

The ubiquitous component to mammalian cell membranes, cholesterol, is an amphipathic sterol with a large hydrophobic region and a small hydroxyl, hydrophillic region [7]. Its large hydrophobic region causes it to locate alongside lipid acyl chains in the hydrophobic inner region of lipid bilayers (Figure 1.3).
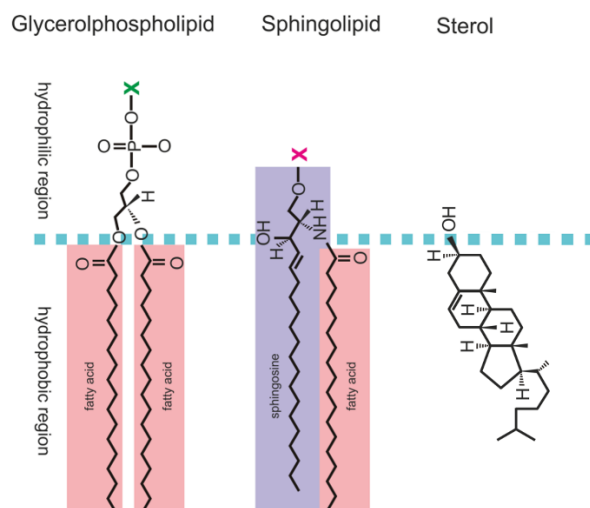
Figure 1.3 Molecular components of lipids orientated into hydrophilic and hydrophobic regions. For the lipids used in this study, the green X attached to the glycerolphospholipid represents choline, ethanolamine or serine and the pink X attached to the spingolipid represents phosphocholine (making SM). The sterol shown is cholesterol [9].

1.3.3.i   Lipid types used in this study

Dipalmitoyl phosphocholine (DPPC) contains two palmitoyl fatty acid acyl chains and a choline attached the phosphate group (Figure 1.5). DPPC is cylinder shaped with similar width of headgroup and acyl chains regions [10] (Figure 1.4). Dipalmitoyl phosphoethanolamine (DPPE) has a free amino acid group which is positively charged at neutral pH [7]. Dipalmitoyl phosphoserine (DPPS) has a protonated amine group which is positively charged [7] (Figure 1.5). DPPS is also cylinder shaped, similar to DPPC [10].

Sphingomyelin (SM) is a major constituent of nerve cells and RBCs and is found mainly on the OL. SM interacts closely with cholesterol, together forming lipid rafts. SM is within the phosphosphingolipids class of sphingolipids (the other class is glycosphingolipids) [7]. It contains the phosphorylcholine headgroup, like PC, and is also zwitterionic but its does not have the glycerol backbone: instead it is built on a sphingosine molecule [7] (Figure 1.5). SM is inverted-cone shaped [10] (Figure 1.4).
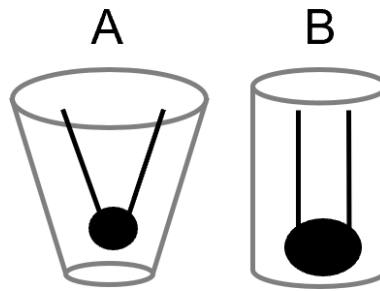
Figure 1.4 Lipid shapes formed due to relative headgroup and acyl chain sizes. A) cone-shaped and B) cylinder shaped.

Diphytanoyl phosphatidylcholine (DPhPC) lipids were identified in archaebacteria and are used in laboratory experiments as a more mechanically stable alternative to DPPC, when working with lipid bilayers [11]. Methyl groups attached to the carbons in the acyl chains stabilise the bilayer (Figure 1.5), causing the lipids to have a lower chain melting transition temperature than DPPC.
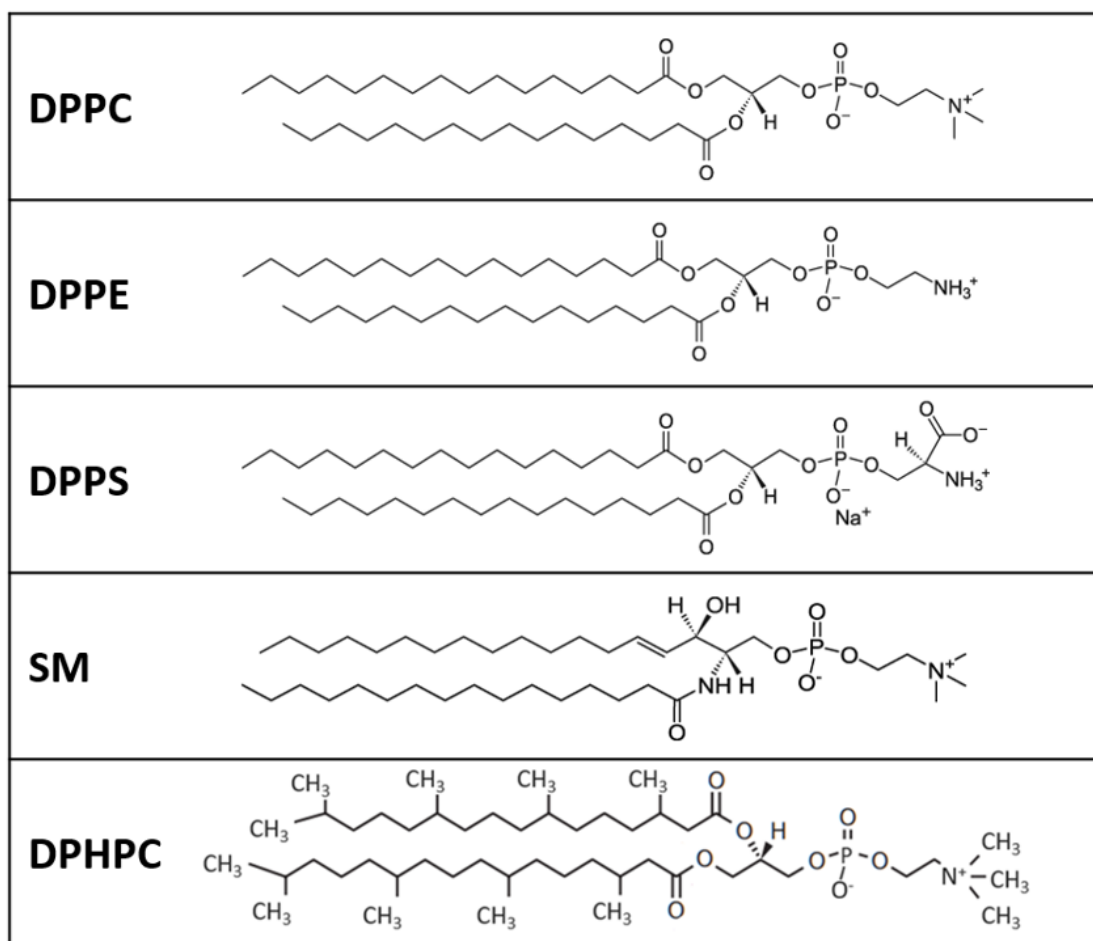
Figure 1.5 Molecular structures of lipids used in this study. Images from the Avanti website (avantilipids.com) where the lipids were purchased, apart from DPhPC image which is from Wang *et al.*, (2012) [12].

1.3.4 Membrane proteins

Membrane proteins are central to cell function with an estimated 30 % of all proteins produced by the cell being destined for the membrane [4] and they account for approximately 50 % of the mass of the membrane [13]. They are hugely important for cell signalling functions and are targets for a large number of therapeutics. Membrane proteins can associate with the cytosol-facing side or the extracellular facing side, and many span across the entire 5 nm lipid bilayer (Figure 1.6). These trans-membrane proteins have domains that extend beyond the lipids, facilitating interaction with extra- and/or intra- cellular molecules. In addition to these trans-membrane proteins, there exists membrane-anchored proteins which also extend beyond the lipids, into the extra-cellular environment.
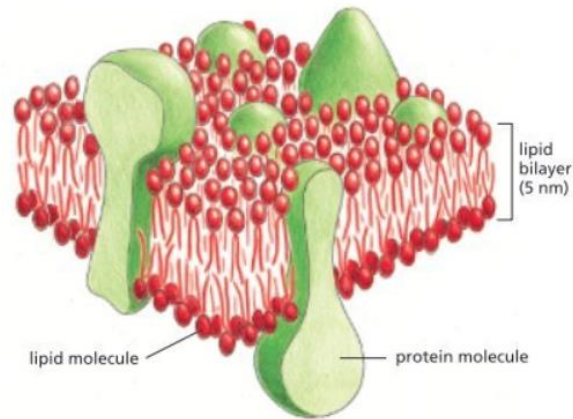
Figure 1.6. Membrane proteins amongst the lipid bilayer of a cell membrane [4].

1.3.5 Hydrophobic effect

The hydrophobic effect is referred to frequently in this thesis and it describes the aggregation of non-polar molecules due to water repulsion [14, 15]. This effect is responsible for the spontaneous organisation of lipids in aqueous environments and the affinity of hydrophobic, membrane-active molecules to the centre of the lipid bilayer.

1.3.6 Lipid rafts

Lipid rafts, ordered structures rich in sphingolipids and stabilised by cholesterol, are thought to exist within the membrane [16] (Figure 1.7). These domains differ from the rest of the membrane in their physical properties, adding again to membrane complexity [16]. The high concentration of cholesterol both thickens and stiffens the membrane in these areas and induces protein sorting [17]; lipid rafts possess a high degree of orientational order compared to the surrounding lipid phase, often referred to as liquid disordered phase. These lipid rafts are likely to be dynamic and transient features of living cells, which form to facilitate certain functions needed such as organising proteins for signal transduction or for transporting proteins away in membrane vesicles [4]. It is now thought that membrane microdomains are transient in both time- and length- scales, which makes them difficult to detect in experimental settings.
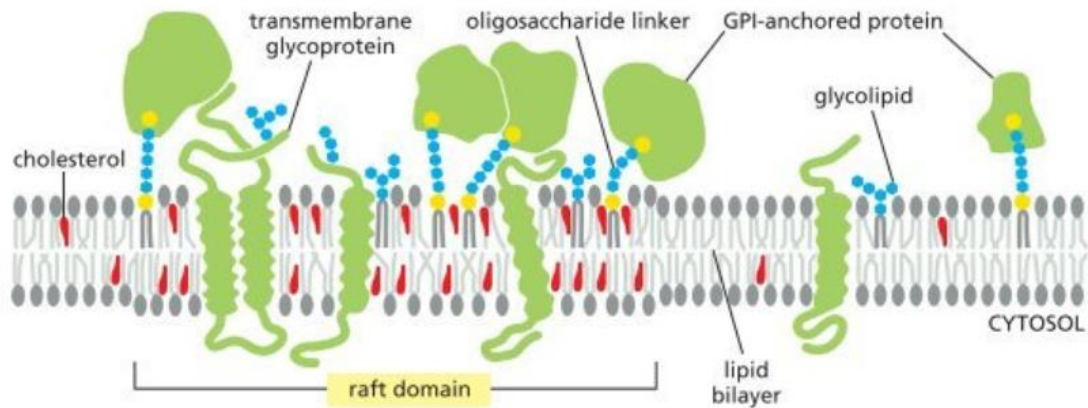
Figure 1.7 Lipid raft domain within a cell membrane. Green figures represent membrane proteins and grey represents all lipids [4].

1.3.7 Pore-forming proteins

Pore-forming proteins are ubiquitous in nature and are used by many pathogens to lyse host cells: in these cases they are classed as toxins. They lyse host cells by punching a hole in the membrane, causing massive disruption to the osmotic balance between the extra- and intra- cellular environment. The result is that the cell swells with too much water, and the membrane rips apart under the pressure.

Bacterial pathogens are especially known to produce a variety of pore-forming toxins [18]. Some well-known examples include *Escherichia coli* (haemolysin), *Mycobacterium tuberculosis* (ESAT-6)*,* and *Streptococcus pneumoniae* (pneumolysin). These all release pore-forming toxins which mediate spread of disease in the host [19-21]. Unfortunately, these bacteria have all demonstrated drug resistance [22-24]. As pore-forming toxins are a common component to them all, these proteins are important to study in terms of human health (e.g. informing development of novel antimicrobials).

Pore-forming proteins are also produced by humans and are important components of the immune system. For example, perforin is a common protein released by T-cells and destroys infected or malignant cells by creating pores thereby preventing the spread of the infection [25]. In fact, there are organisms from every kingdom of life that have evolved an ability to compromise the selective permeability of the cell membrane barrier [18]. It is therefore important to have knowledge of how these toxins work as well as to establish a wide range of methods to characterise these systems.

Pore-forming proteins begin as soluble monomers and need to undergo several steps to create a pore in a membrane. The three main steps are 1) monomer binding to the host cell membrane (either to a receptor or through hydrophobic interaction with the lipids), 2) oligomerisation of monomers by passive diffusion, and 3) conformational change of the oligomer, which forms a pore through the membrane [26] (Figure 1.8).
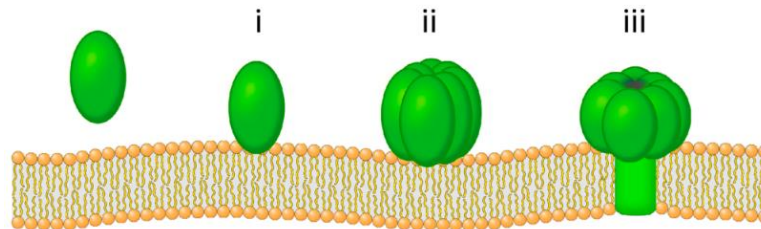
Figure 1.8 Overview of the three stages to pore-formation by pore-forming proteins [26].

The mechanistic steps of pore formation by toxins are not fully characterised. As each step includes physical interactions (mechanical, electrostatic, viscous), the physical properties of the membrane (electrical properties, visco-elasticity and phospholipid composition and phase state) all play a significant role in controlling cytolytic activity.

The Petrov group (led by Dr. Peter Petrov, department of Biophysics, the Physics Building, University of Exeter, EX4 4QL) have examined some membrane-targeting toxins using biophysical methods to characterise both the process of toxin-membrane interaction and the properties of the membrane which affect the cell susceptibility to pore forming toxins. It is now important to widen the scope of this approach to include other (bacterial and/or parasite) toxins.

The RBC provides a simple and well-characterised example of a cell membrane and its susceptibility to the streptococcus toxin, pneumolysin, has been recently investigated [27]. These experiments were conducted to understand why, in a single population of RBCs, there were vast variations in the time taken for cell lysis by pneumolysin [27]. The toxin was found to insert preferentially into stomatocytes over discocytes indicating an effect of membrane curvature on toxin binding [27]. In addition, the toxin preferentially bound to spikes on echinocytic RBCs showing a preference for areas in the membrane of high curvature [27]. The electrostatic surface and dipole potentials of the membrane also had an effect on the time taken for lysis

by the toxin where a more negatively charged membrane increased resistance [27]. An interesting correlation between the membrane elastic modulus and susceptibility to toxin was also observed, making stiffer cells, perhaps surprisingly, more susceptible to lysis by the toxin.

Interestingly, this study unexpectedly revealed that diabetic RBCs are less susceptible to pneumolysin and perfringolysin O toxins than healthy cells [27]. This was attributed to oxidative modifications of the RBC membrane because of the higher level of reactive oxidative species in the diabetic milieu. This is an example where characterising membrane physical properties can provide a first-base understanding of a system and open up further channels of investigation.

Toxin interactions can vary depending on the type of lipids involved, such as the shape of lipids creating curvature and permeability. The double-chained lipids found in the cell membrane can be assigned to three groups based on their shape: truncated cones, inverted truncated cones, and cylinders [28]. Because of these differences in molecular geometry, some lipids can induce local changes in the membrane curvature as well as its permeability [10].

A study of a bacterial toxin, suilysin, characterised the formation of pores in the membrane from incomplete rings (hemi-pores) of toxin oligomers inserting into the membrane [29]. A similar arc-type of pore-formation was found with pneumolysin where incomplete rings of toxin monomers were able to create pores through the mechanism of the lipid bilayer receding back and becoming part of the edge to the pore (Figure 1.9A) [30]. With complete rings, they observed that the lipid bilayer recedes from one side to the other suggesting a stepwise process of toxin insertion and forces on the lipid membrane (Figure 1.9B). The physical properties behind this movement were not addressed in this study, further highlighting the need for biophysical examination of the pore-formation process.
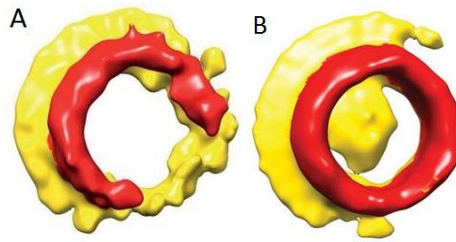
Figure 1.9 Images of pore structure obtained by cryo-electron tomography. A) arc-type pore formation, and B) complete ring pore formation with the lipid bilayer receding back to one side. Membrane indicated in yellow and lipids in red. [30]

1.4 Epsilon toxin

In the first part of this thesis, interactions between a pore-forming toxin and the membrane are investigated. We chose to work with pore-forming toxins because they are very destructive virulence factors used by many pathogens for the specific purpose of punching a hole in the host cell membrane. The epsilon toxin was chosen due to its extreme potency and involvement in multiple sclerosis in humans.

The pore forming protein Epsilon toxin (Etx) is produced by the pathogenic intestinal bacteria *Clostridium perfringens* which is a gram-positive anaerobic spore forming bacteria. Known to produce at least 17 toxins [31], *C. perfringens* have been classified into five toxinotypes (A to E) which each have a mixture of two to three of the major *Clostridial* toxins (α, β, ε (Etx), and ι) [32, 33]. Etx is produced by *C. perfringens* toxinotypes B and D.

Etx is a highly toxic protein responsible for causing fatal enterotoxaemia in sheep goats, foals and calves. Although not much is known about the extent to which these bacteria are found in human intestines, the toxin has been implicated in the development of multiple sclerosis (M.S.) in humans [34-36]. Due to its high potency (the lethal dose of epsilon toxin in mice is 50 ng/kg), Etx is classed as a category B potential bioweapon by the United States government Centres for Disease Control and Prevention (CDC) creating the need for human vaccine research, design and production [37].

1.4.1 The aerolysin-like proteins family (structural characteristics)

Like most *Clostridium* toxins, Etx is a heptameric, pore-forming β-toxin, within the aerolysin family, which also includes *Aeromonas* aerolysin and *Clostridium septicum*

alpha toxin [38]. The aerolysins initially exist as soluble monomers which bind to target cell membranes and oligomerise to form a heptameric (consisting of seven monomers) pore complex [39]. The Etx pore is probably a general diffusion pore [40]. Cells affected by Etx swell until osmotic stress causes lysis [41].

1.4.2 Etx monomer

The mass of the monomer is approximately 35 kDa [41, 42] and three domains have been identified: the receptor-binding domain, the pore-forming module, and the cap domain [43] (Figure 1.10). These three domains have been likened to domains two, three, and four in the related β-toxin, aerolysin, because of their similar structure, and therefore likely functions [44]. The receptor-binding region, also known as domain one, spans from amino acid 1-62 and 199-234 [42] and includes some key residues previously identified for binding [45, 46]. The pore-forming module, also known as domain two, is rich in β-strands which undergo huge conformational change to punch a hole through the host cell membrane. The cap domain, otherwise known as domain three, is where the C-terminal peptide is cleaved off for activation of the toxin. Once the C-terminal peptide is removed, the monomers are able to oligomerise [39, 42].

Figure 1.10 The ribbon structure of the Etx monomer [47]. The N-terminal and C-terminal ends are marked in domain one and domain three, respectively.

1.4.3 Etx pore complex

The structure of the heptameric Etx pore was recently described using electron microscopy, finding it is 98 Å (angstroms) deep, 24 Å in diameter of the inner pore and 120 Å diameter of the structure (Figure 1.11) [42]. The depth of the membrane-spanning region is approximately 30 - 35 Å [42]. They found that the membrane inserting region is residues 119 - 148 as they interact with micelle lipids as seen in unfiltered electron microscopy (EM) maps [42]. There are several tyrosine residues, which have a hydrophobic side chain, that are located just above the membrane which have been identified previously as important in receptor binding (Tyr 42, 43, 49, 209) (Figure 1.12c) [42]. The apparent mass of the pore-complex, as determined by gel electrophoresis, is approximately 155 kDa [41, 42].
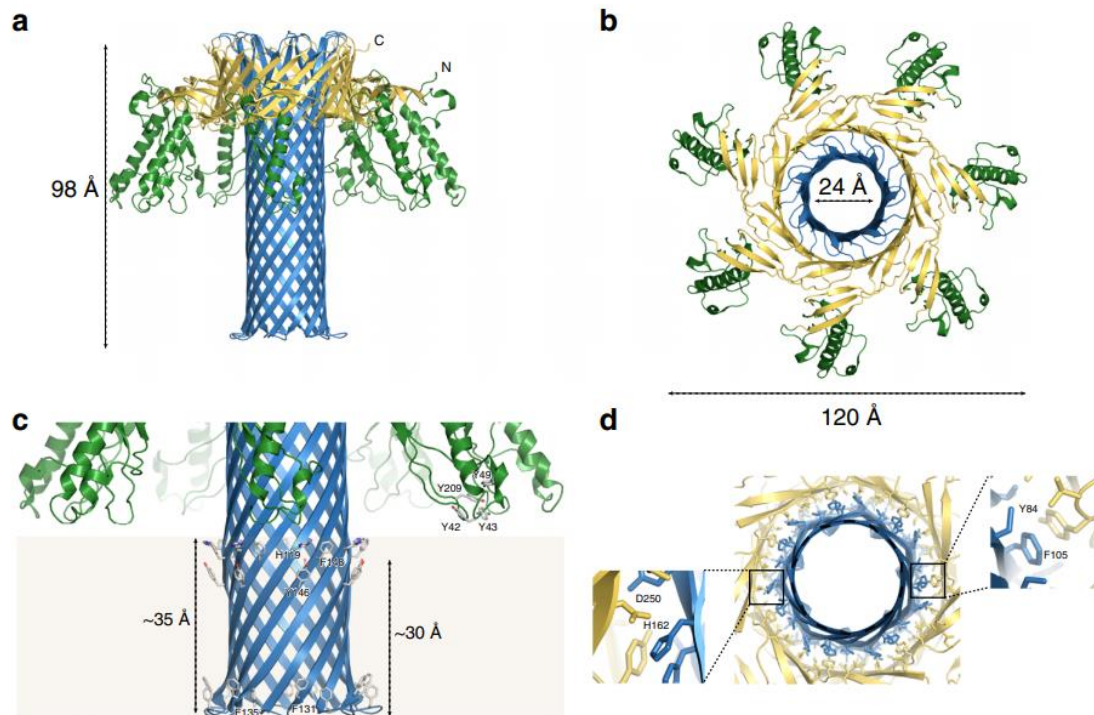
Figure 1.11 Etx pore structure in cartoon representation. a) The pore with the fully unravelled β-barrel is 98 Å deep. b) Projected view from above (extracellularly) showing inner pore diameter. c) The transmembrane section of the β-barrel represented with shading and tyrosine (Y) amino acids in the receptor-binding domain (green) are shown. d) Insets to show interaction of amino acids in the pore-forming module (blue) with the cap domain (yellow). [42]

1.4.4 Susceptible cells

Etx has previously been shown only be toxic to certain cell lines e.g. MDCK cells where it targets lipid raft areas of membranes, also known as detergent-insoluble microdomains [48]. However, in recent years Etx has demonstrated toxicity to other cell lines such as the human renal adenocarcinoma cell line, ACHN [49].

The specificity of Etx suggests that activity depends on specific receptors on its target cells. Many studies have tried to identify the cell receptor for this toxin. The current candidate receptors are myelin and lymphocyte protein (MAL) [35] and the lesser mentioned, hepatitis A virus cellular receptor 1 (HAVCR1) [46]. MAL was shown to be the receptor required by transfecting Etx-resistant cells, Chinese hamster ovary (CHO), with hMAL-GFP plasmids [35]. Fluorescence-activated cell sorting (FACS)

showed that Etx bound to cells expressing hMAL-GFP and not to GFP-only expressing CHO cells [35].

1.4.4.i The MAL receptor

MAL is a protein which resides in lipid rafts of renal epithelium, myelin, and T-lymphocyte cells as well as in many other cell types [35, 50]. MAL is important for maintaining lipid raft domains [51], which is interesting because of the finding that Etx targets lipid raft domains in MDCK cells [48].

1.4.4.ii Red blood cell susceptibility

In addition to susceptible cell lines, Etx can rupture human RBCs, however, the mechanism of this haemolysis remains unclear. One study has evidenced that an Etx pore could activate purinergic (P2) receptors causing Ca^{2+} influx which, in addition to the flux of K^+ and Cl^- through the Etx pore, induces haemolysis [52]. Another mechanism has since been suggested where Etx-pores cause the cell to swell, causing ICln chloride channels to activate in order to reduce osmotic stress: these channels then become inhibited by the iron leaked through the pore as well as by copper leaked from nearby T-cells under attack [53].

It is uniquely difficult to probe for membrane proteins of RBCs because they do not have DNA, RNA, or indeed a nucleus, and therefore protein expression cannot be predicted from DNA or RNA sequencing. In starting this study, it was unclear whether RBCs exhibited a MAL receptor. However, a MAL receptor in the human erythroleukemia (HEL) cell line, which represents an early life-stage of RBCs which still possess a nucleus, has since been reported [54]. In addition, there is some evidence of an isoform of MAL, MAL C, found in RBCs [53]

1.4.4.iii Hydrophobic interactions

Etx has also been shown to form pores in artificial lipid membranes without protein receptors [40, 55, 56]. The receptor-binding domain of the Etx monomer is mainly hydrophobic, containing several amino acids with hydrophobic side chains. Uncharged areas can be seen in the map of charges of the Etx pore in Figure 1.12 [42]. These regions would be attracted to the acyl chain region of lipid bilayers and indeed hydrophobic interaction of Etx and artificial lipid bilayers have been previously recorded [40, 56].

33
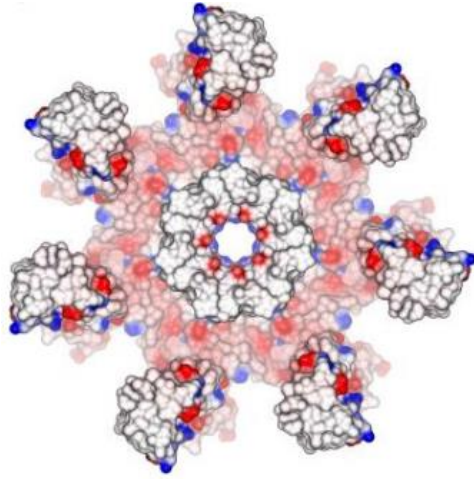
Figure 1.12 Etx pore as viewed from the intracellular side of a membrane. Negative charges indicated in red, positive charges indicated in blue and uncharged (hydrophobic) regions shown in grey [42].

In summary, specific details of the three stages involved in the action of Etx – binding, oligomerisation and pore formation leading to lysis of the cell, are still emerging. Further clarification of these is required to enable identification of the specific amino acids involved in each stage. This would enable production of specific variants that would retain enough features of the wild type to produce an immune response but without toxicity, the ideal formula for a vaccine.

1.5 Chitosan

The PhD began with the aim of investigating virulence factors produced by the parasite, *Entamoeba histolytica*, during infection in the human host. Initial work involved trying to produce the virulence factor, amoebapore, in the laboratory. However, the techniques proved ineffective (see Appendix 2) and the virulence factor, chitosan, was focussed on instead. This makes up the second part of this thesis.

We chose to work with chitosan because it is synthesised by the important human pathogen, *Entamoeba histolytica,* to facilitate its transition into the cyst stage of its life cycle, which is the stage responsible for transmission and thus an important target for amoebiasis control [57]. Not only is it a component of *E. histolytica* cyst walls but it is found in *Mucor rouxii* walls and *Saccharomyces cerevisiae* spores as well [58].

The physical effects of chitosan being deposited on mammalian lipid membranes are not well characterised. In addition, the need to understand chitosan interactions with cell membranes is in fact more general because chitosan is used in several different medical contexts, such as wound dressing and drug delivery, and in most of these processes, chitosan comes into contact with lipid membranes. It is therefore important to understand direct interactions between this polysaccharide and mammalian lipid membranes.

Chitosan is derived from chitin which is the second most common naturally occurring polymer after cellulose [59]. Chitin is found naturally in the exoskeleton of crustaceans and insects. Chitin is highly insoluble; however, chitosan is soluble in weak acidic solutions.

1.5.1 Structure and properties

Chitosan is a large (50-190 kg/mol), cationic polysaccharide formed by *N*-deacetylation of chitin (Figure 1.13). Chitin is insoluble; however, when converted to chitosan it becomes soluble in a weak acid. Chitosan is a linear chain with a backbone of hydroxyl groups and amino groups, the latter of which become protonated in the weak acidic solution, resulting in the polymer having a net positive charge [59, 60].

The degree of deacetylation of chitin can vary with different manufacturing methods. The number of unchanged, acetyl (CH_3CO) moieties (X in Figure 1.13) decreases with deacetylation. These acetyl moieties are uncharged, and therefore the solubility of chitosan also decreases with deacetylation. Most importantly, the acetyl groups create pockets of hydrophobicity in the polymer which can cause the polymer to coil in such a way to hide these from an external aqueous environment [61]. They are also likely to facilitate hydrophobic insertion into the hydrophobic acyl chains region of lipid membranes.
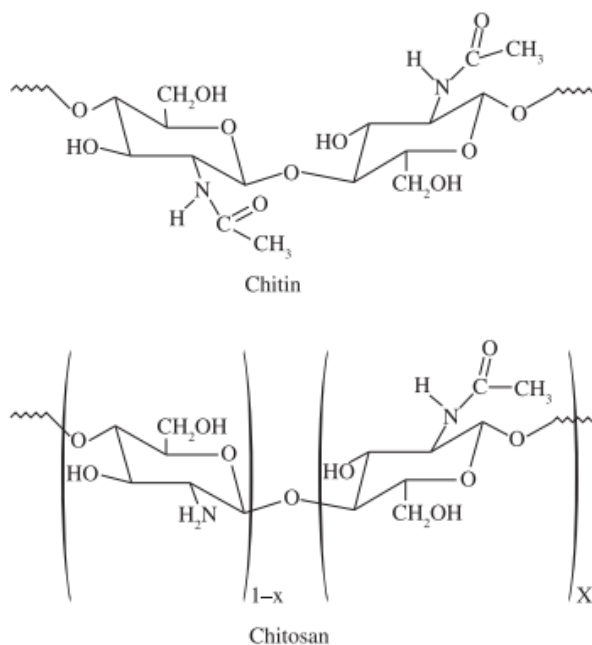
Figure 1.13 Molecular structures of chitin and chitosan [62]. 1-x denotes the moieties that have undergone *N*-deacetylation whereas x marks the moieties that evaded deacetylation.

1.5.2 Applications

Chitosan has a variety of unique biological applications. It is used as a haemostatic dressing due to its effect on RBCs causing agglutination, which is useful as it is independent of the clotting cascade [63]. It has a broad range of antibacterial and antifungal activity, effective against both gram negative and positive bacteria [62]. Further, it is used in supplements to reduce obesity due to its ability to bind dietary lipids and thus prevent intestinal lipid absorption [64].

1.5.3 Chitosan-lipid interactions

Wydro *et al.*, (2007) [65] showed that chitosan adsorbed to lipids, fatty acids and cholesterol and that each monolayer expanded with chitosan. However, the monolayers were modified in a way that more compact monolayers of stearic acid and cholesterol were loosened and less compact monolayers of unsaturated lipids were tightened [65]. Therefore, Wydro and colleagues suggest that chitosan interaction is both electrostatic and hydrophobic and hydrogen bonds are formed.

Pavinatto *et al.*, (2007) [66] showed that chitosan caused expansion and decrease of both the static dilatational modulus, ε, and the dynamic dilatational modulus, as measured by axisymmetric shape drop analysis, indicating an added "soft" component to the DMPA monolayers. When the monolayer was compressed, some chitosan was released [66]. Vibration spectroscopy and surface potential measurements indicated that chitosan induced ordering of DMPA alkyl chains [66].

The lipid species DPPC and DPPG and their interactions with chitosan have been examined in several studies, with the general findings that chitosan causes monolayer expansion and a decrease in static elasticity (ε) with larger effects seen with the negatively charged DPPG lipids [61, 67-71]. The effect of chitosan on the dynamic elasticity (E) varies between DMPA, DPPC, and DPPG monolayers [66, 72]. In summary, chitosan is known to interact with lipids and can affect the physical state of monolayers. However, the mechanism of this process has not yet been examined using the mixture of lipids and cholesterol which is representative of mammalian cells.

Table 1.1 Relevant findings from some key papers looking at the interaction of chitosan with monolayers. Symbol ε denotes the static dilatational elastic modulus and the symbol E denotes the dynamic dilatational elastic modulus.

First author, year, citation	Monolayer type	Measurement	Technique	Finding
Pavinatto *et al.*, 2005 [69]	cholesterol	area/molecule	n/a	expansion
		surface pressure	pressure-area isotherms	
		morphology	brewster angle microscopy	larger cholesterol domains
Wydro *et al.*, 2007 [65]	Unsaturated fatty acids	area/molecule	n/a	expansion
		ε	pressure-area isotherms	decrease
Pavinatto *et al.*, 2007 [66]	DMPA	area/molecule	n/a	expansion
		ε	pressure-area isotherms	decrease
		E	pendant-drop	decrease
Pavinatto *et al.*, 2007 [72]	DPPC	area/molecule	n/a	expansion
		ε	pressure-area isotherms	no relevant decrease
		E	pendant-drop	increase at lower surface pressure
	DPPG	area/molecule	n/a	expansion
		ε	pressure-area isotherms	no relevant decrease
		E	pendant-drop	large increase

First author, year, citation	Monolayer type	Measurement	Technique	Finding
Pavinatto et al., 2010 [61]	DPPC	area/molecule	n/a	expansion
		ε	pressure-area isotherms	decrease
	DPPG	area/molecule	n/a	expansion
		ε	pressure-area isotherms	major decrease
Krajewska et al., 2013 [67]	DPPG	area/molecule	n/a	more expansion with lower pH and higher temperature
		surface pressure	pressure-area isotherms	
		ε	pressure-area isotherms	decrease
Krajewska et al., 2013 [68]	DPPC	area/molecule	n/a	small expansion
		ε	pressure-area isotherms	small change
Pavinatto et al., 2016 [70]	DPPC	area/molecule	n/a	expansion
		ε	pressure-area isotherms	decrease
		acyl chain conformation	vibration spectroscopy	penetrated to acyl chains
				reduced order in acyl chains
	DPPG	area/molecule	n/a	expansion
		ε	pressure-area isotherms	decrease
		lipid surface density	vibration spectroscopy	decrease
		acyl chain density		no change
		acyl chain conformation		penetrated to acyl chains
				reduced order in acyl chains
Oliveira et al., 2020 [71]	DPPC	area/molecule	n/a	small expansion
		ε	pressure-area isotherms	decrease
		acyl chain conformation	vibration spectroscopy	lipid domains preserved (when chitosan added to expanded monolayer)
				lipid domains suppressed (when chitosan added to compressed monolayer)
	DPPG	area/molecule	n/a	distinct expansion
		ε	pressure-area isotherms	large decrease
		acyl chain conformation	vibration spectroscopy	lipid domains suppressed (when chitosan added to expanded monolayer)
				lipid domains preserved (when chitosan added to compressed monolayer)

1.6 Summary of knowledge gaps

The Etx protein functional domains have been well described, however, much remains to be learnt about which amino acids are important and/or essential for each stage of pore-formation. This is made difficult by the pronounced variation in toxicity between cell types. A number of studies have identified amino acids required for Etx binding to the membranes of commonly used laboratory cell-lines, such as CHO and MDCK. However, investigations into individual amino acids important for pore-formation in RBCs is lacking in the literature. This thesis addresses this knowledge gap by testing variants of Etx on RBCs, isolated RBC membranes, and synthetic lipid bilayers.

Although there are several studies looking at chitosan interaction with lipid monolayers, investigative studies with chitosan and mammalian-representative lipid monolayers are lacking. Therefore, monolayers made up of lipid species that represent both the IL and OL components of mammalian cells, were used in this thesis. Rheological (visco-elasticity) and structural information were obtained to describe the interactions with chitosan.

This thesis is structured such that there is one methods chapter, three results and discussion chapters, a conclusions chapter, and finally, an appendix. The first results and discussions chapter contains the exploration of Etx action on cells and membrane models, and the second and third contain the analysis of chitosan interactions with lipid monolayers.

2 <u>Methods</u>

2.1 Research into cell membranes

New developments in science are revealing both the fundamental importance of cell membranes in all biological systems, but also the astonishing complexity of their structure and function. This very complexity makes them difficult to mimic in a laboratory setting for investigation. Cell membranes are basically composed of a double layer of phospholipids, cholesterol, and proteins, but what makes them so complex is the abundance of lipid and protein species, heterogeneity of arrangement, and diversity of interactions between these basic components.

In many cases, the composition of membrane components determines the physical properties of the membrane, such as shape, permeability, viscoelasticity and electrical potential. Biological processes are often dependent on these physical properties and any changes to the state of the membrane, such as by external membrane-active substances, can change the functions which that cell can perform. Conversely, the inherent susceptibility of cells to external substances is often dependent on the physical state of the membrane. For example, Bokori-Brown *et al.* (2016), [27] demonstrated that the membrane dilatational elastic modulus, ε, correlates with cell susceptibility to *Streptococcus pneumonia* toxin.

A common biological approach to investigate which parts of a protein contribute to its activity (e.g. toxicity) is to produce a version of the protein (a recombinant variant) in the laboratory, with a targeted amino acid change. The amino acid candidates for mutation are normally selected through knowledge of the exposed amino acids from the protein's predicted, or actual, crystal structure. The chemical properties of the amino acids, such as polarity and molecular structure are also taken into account in this decision [73].

However, to a physicist, the biological approach leaves a lot of a lot of unanswered questions, especially at a mesoscopic level where physical properties can have high impact. Does the protein change the physical properties of the membrane? Does it change lipid organisation in the membranes? What physical mechanism explains differences in toxicity? Are there certain properties of membranes that make them more susceptible (e.g. membrane fluidity, elasticity or electrostaticity)? Which areas

of the cell membrane are kinetically favourable for protein insertion? Can we define a characteristic which explains why one cell is resistant while another is not?

These questions of membrane interactions can be investigated using biophysical approaches and techniques. The complexities of the biological cell can be broken down into specific parameters which, when tested in a well-defined experiment, can be standardised for comparison between systems. Such systems are frequently referred to as biological models.

The individual parameters cannot completely describe the complex, biological situation which exists in living cells, but they are reliable and quantitative building blocks characterising the physical state and physical interactions in the model system which may help to explain the respective processes in the real biological system. When several parameters, in a variety of models, are investigated, a more accurate picture of how each physical property contributes to the interaction in question is formed. There are several established methods for this building-block type of investigation using lipid membrane systems, artificial lipid bilayers, and RBCs. This thesis uses a biophysics approach to investigate a pore-forming toxin, Etx, and a polysaccharide, chitosan, on cell membranes.

2.2 Epsilon toxin experiments

This section describes the experimental systems used to address the first part of the thesis: investigating the interaction of Etx with cell membranes. This includes objective 1 (to examine haemolytic effects of Etx with RBCs) and 2 (to investigate the importance of selected amino acids in the three stages of Etx pore-formation in RBCs).

2.2.1 Epsilon toxin variants description

Recombinant Etx protein was produced and purified by Monika Bokori-Brown at the University of Exeter. Several variations of the toxin were produced using site-directed mutagenesis of the *etxD* gene. The recombinant proteins were His-tagged, meaning that there were several histidine (H, or His) amino acids added to facilitate separation from other proteins in the protein purification step. His-tags can be placed at the carboxyl terminal (C-terminal, or CT) or the amino terminal (N-terminal, or NT) of the protein.

CT His-tagged toxins were used because they lose their His-tag during the activation step, as cleavage occurs at the CT end of the protein, therefore these variants more accurately represent the wildtype (WT) Etx, as produced by *Clostridium perfringens*. Activation by trypsin cleaves amino acids from both the N-terminal and C-terminal ends of the protein, however, our variants do not include the N-terminal amino acids of the WT that would be cleaved.

Single amino acid mutations in the receptor-binding domain were directed at amino acid numbers 42 and 43 which were converted from tyrosine (Y) to alanine (A) and named Y42A and Y43A, respectively. These amino acids were chosen for mutation because of their accessible location in the receptor-binding domain [46], and their aromatic side chains (meaning their partial hydrophobicity places them in regions with potential for interaction [73]) (Figure 2.1). In addition, a previous study found evidence towards possible glycan binding sites in the Y42 region [45]. Lastly, the Y43 amino acid has been shown to be important for Etx toxicity in MDCK cells [45, 46] and has been directly implicated in binding to the hMAL receptor [35].

The final epsilon toxin variant contained a mutation to the amino acid number 162 in the pore-forming module, where an H was replaced by an A (Figure 2.1). This variation was therefore named H162A. As this mutation had been shown to allow receptor binding but prevent any pore-formation, it was previously used as a background mutation (a 'safety stop') for testing receptor binding site mutations in the laboratory [45]. However, H162A cytotoxicity on RBCs had not previously been reported and therefore this variant was evaluated alongside the receptor-binding domain mutation variants in all experiments.
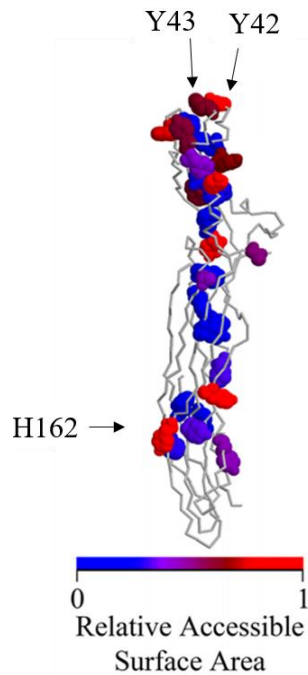
Figure 2.1 Etx mutation sites in the monomer. Amino acids with aromatic side chains (Histidine, Tyrosine, Phenylalanine, and Tryptophan) are shown in space-filling representation and the relative exposure of these amino acids are indicated by the colour scale. Ribbon diagram created by Ivie and McClain [46] with annotations added for this thesis.

Several previous studies [45, 46] have used a numbering notation which excludes the first 13 N-terminal amino acids, which are cleaved in activation (and not included in our Etx variant sequences). However, in this thesis the Etx protein variants will be referred to using numbering that includes the first 13 N-terminal amino acids. The sequences of the recombinant Etx variants, as well as the native Etx protein, are shown in Figure 2.2. Methionine (M) is at the start to induce translation and Glycine (G) is added immediately after because cleavage of M is more likely to happen when the amino acid following is small in size, such as with G [74].

```
Native     MKKNLVKSLAIASAVISIYSIVNIVSPTNVIAKEISNTVSNEMSKKASYDNVDTLIEKGR  60
WT         -----------------------------------------MGKASYDNVDTLIEKGR  17
Y42A       -----------------------------------------MGKASYDNVDTLIEKGR  17
Y43A       -----------------------------------------MGKASYDNVDTLIEKGR  17
H162A      -----------------------------------------MGKASYDNVDTLIEKGR  17
                                                    **************

Native     YNTKYNYLKRMEKYYPNAMAYFDKVTINPQGNDFYINNPKVELDGEPSMNYLEDVYVGKA 120
WT         YNTKYNYLKRMEKYYPNAMAYFDKVTINPQGNDFYINNPKVELDGEPSMNYLEDVYVGKA  77
Y42A       YNTKYNYLKRMEKAYPNAMAYFDKVTINPQGNDFYINNPKVELDGEPSMNYLEDVYVGKA  77
Y43A       YNTKYNYLKRMEKYAPNAMAYFDKVTINPQGNDFYINNPKVELDGEPSMNYLEDVYVGKA  77
H162A      YNTKYNYLKRMEKYYPNAMAYFDKVTINPQGNDFYINNPKVELDGEPSMNYLEDVYVGKA  77
           *************  *******************************************

Native     LLTNDTQQEQKLKSQSFTCKNTDTVTATTTHTVGTSIQATAKFTVPFNETGVSLTTSYSF 180
WT         LLTNDTQQEQKLKSQSFTCKNTDTVTATTTHTVGTSIQATAKFTVPFNETGVSLTTSYSF 137
Y42A       LLTNDTQQEQKLKSQSFTCKNTDTVTATTTHTVGTSIQATAKFTVPFNETGVSLTTSYSF 137
Y43A       LLTNDTQQEQKLKSQSFTCKNTDTVTATTTHTVGTSIQATAKFTVPFNETGVSLTTSYSF 137
H162A      LLTNDTQQEQKLKSQSFTCKNTDTVTATTTHTVGTSIQATAKFTVPFNETGVSLTTSYSF 137
           ************************************************************

Native     ANTNTNTNSKEITHNVPSQDILVPANTTVEVIAYLKKVNVKGNVKLVGQVSGSEWGEIPS 240
WT         ANTNTNTNSKEITHNVPSQDILVPANTTVEVIAYLKKVNVKGNVKLVGQVSGSEWGEIPS 197
Y42A       ANTNTNTNSKEITHNVPSQDILVPANTTVEVIAYLKKVNVKGNVKLVGQVSGSEWGEIPS 197
Y43A       ANTNTNTNSKEITHNVPSQDILVPANTTVEVIAYLKKVNVKGNVKLVGQVSGSEWGEIPS 197
H162A      ANTNTNTNSKEITANVPSQDILVPANTTVEVIAYLKKVNVKGNVKLVGQVSGSEWGEIPS 197
           ************* **********************************************

Native     YLAFPRDGYKFSLSDTVNKSDLNEDGTININGKGNYSAVMGDELIVKVRNLNTNNVQEYV 300
WT         YLAFPRDGYKFSLSDTVNKSDLNEDGTININGKGNYSAVMGDELIVKVRNLNTNNVQEYV 257
Y42A       YLAFPRDGYKFSLSDTVNKSDLNEDGTININGKGNYSAVMGDELIVKVRNLNTNNVQEYV 257
Y43A       YLAFPRDGYKFSLSDTVNKSDLNEDGTININGKGNYSAVMGDELIVKVRNLNTNNVQEYV 257
H162A      YLAFPRDGYKFSLSDTVNKSDLNEDGTININGKGNYSAVMGDELIVKVRNLNTNNVQEYV 257
           *********************************************************

Native     IPVDKKEKSNDSNIVKYRSLSIKAPGIK--------          328
WT         IPVDKKEKSNDSNIVKYRSLSIKAPGIKLEHHHHHH          293
Y42A       IPVDKKEKSNDSNIVKYRSLYIKAPGIKLEHHHHHH          293
Y43A       IPVDKKEKSNDSNIVKYRSLYIKAPGIKLEHHHHHH          293
H162A      IPVDKKEKSNDSNIVKYRSLYIKAPGIKLEHHHHHH          293
           ******************** *******
```

Figure 2.2 Etx amino acid variants alignment (CLUSTAL O(1.2.4)). The native Etx, produced by *Clostridium perfringens* has been previously sequenced by Gangwar *et al*., 2017, and can be found at GenBank: ATY49621.1. Bold letters with a shaded background mark the amino acid mutation. Underlined areas represent the cleavage sites of trypsin during activation [75]. As the 13 amino acids found in non-activated Etx are not included in our variants, the numbering here uses the activated toxin numbering notation.

2.2.2 Toxin activation

Trypsin was used to cleave off the C-terminal peptide sequence, converting the pro-toxin (P-Etx) to its activated state which can then oligomerise in a membrane. Trypsin (treated with TPCK (L-(tosylamido-2-phenyl) ethyl chloromethyl ketone)) from bovine pancreas (Sigma-Aldrich) was prepared in DPBS (Dulbecco's phosphate buffered saline) at 1 mg/ml.

Purified, recombinant, P-Etx was activated by incubation with Trypsin at a 1:100 ratio for 1 hour at room temperature (approximately 20 °C). Trypsin inhibitor (from *Glycine max* (soybean) (Sigma-Aldrich)) solution, at 1 mg/ml in DPBS, was added at 0.66 mg per 1 mg trypsin to stop the reaction. The sample was centrifuged for 1 minute at 13 000 rpm to remove any precipitate and the supernatant containing the soluble toxin was transferred to a new Eppendorf tube. The final protein concentration was measured using a Nanodrop spectrophotometer.Activated Etx was used on the day of activation, after overnight storage in the fridge or it was frozen immediately at -20 °C and used within a few weeks.

2.2.3 Epsilon toxin binding and oligomerization assay

RBC membranes were extracted, non-activated toxin (P-toxin) was used to test binding, and activated toxin was used to look at oligomerisation. Previously extracted RBC membranes (by Bokori-Brown) were incubated at room temperature for one hour with either 10 µM trypsin-activated Etx, or 10 µM P-Etx (non-activated), for the oligomerisation and binding assays, respectively. Any Etx not bound to the membrane material and still in solution was removed by centrifugation at 20 000 x g for 30 minutes. The remaining pellet was resuspended in 20 µl 2 x lithium dodecyl sulfate (LDS) buffer (NuPAGE, Invitrogen Ltd., Paisley, UK).

Sodium dodecyl sulfate polyacrylamide gel electrophoresis (SDS-PAGE) was carried out on the membrane-Etx, membrane-P-Etx, Etx-only and P-Etx-only samples and the protein ladder used was Perfect Protein™ Marker, 10–225 kDa (Merck, Darmstadt, Germany). Samples were loaded in a 7 % Tris-Acetate protein gel (NuPAGE™, Invitrogen Ltd., Paisley, UK) and run at 150 V for 1 hour, in a Tris-Acetate SDS Running Buffer (NuPAGE™, Invitrogen Ltd., Paisley, UK) using Surelock Xcell apparatus (Invitrogen Ltd, Paisley, UK).

The SDS-PAGE gel was removed from the apparatus and the samples transferred to a nitrocellulose membrane for the western blot, using the Trans-Blot® Turbo™ Transfer System (Bio-Rad). Once transferred, a blocking agent (5% skimmed milk, 0.1 % Tween-20 in PBS) was applied to the samples on the nitrocellulose membrane so that casein from the milk bound to any exposed area of nitrocellulose, preventing antibodies from binding non-specifically to the membrane. The membrane was blocked for one hour at room temperature, maintaining agitation on a see-saw rocker. The membrane was washed three times in 5 % Tween-20 in PBS for 10 minutes each on the see-saw rocker.

Antibodies were diluted in 3 % skimmed milk, 0.1 % Tween-20 in PBS at dilutions of 1:500 for the rabbit polyclonal anti-Etx primary antibody (Bokori-Brown), 1:4000 for the red cell membrane loading control, flotillin 2 mouse monoclonal primary antibody (proteintech), and 1:5000 for both the goat anti-rabbit IgG (H+L) IRDye® 800CW and the goat (polyclonal) anti-mouse IgG (H+L) IRDye® 680RD secondary antibodies (LI-COR Biosciences). The primary antibody solution was added to the membrane and incubated for one hour at room temperature on the see-saw rocker. The membrane was washed three times, as above, and the secondary antibody solution was incubated with the membrane for one hour at room temperature, followed by washing again.

Bound antibodies were imaged in the Odyssey CLx infrared imaging system (LI-COR Biosciences, Lincoln, USA). Quantitative analysis of the intensity of the loading control band, compared to that of the Etx protein band was performed by Bokori-Brown using Image Studio (5.2) software with the Housekeeping Protein Normalisation Protocol (LI-COR Biosciences, Lincoln, USA).

2.2.4 RBCs as models

Mammalian RBCs lose their nucleus and other organelles during maturation [7]. Like other mammalian cells, they have a lipid bilayer but have a reduced cytoskeleton (a 2D mesh composed of spectrin filaments) and the cytosol consists of a fixed concentration of haemoglobin [76]. Due to this reduced complexity, and the fact that RBC's morphology, elasticity, and membrane lipid composition are relatively well understood, erythrocytes make good models for studying the physical properties of mammalian cell membranes and their response to exogenous agents.

Several methods to analyse the effect of biochemicals on RBCs have been previously developed in the Petrov-Winlove laboratory [27, 77-80]. For example, by using thermal fluctuation spectroscopy, a correlation between a higher bending elastic modulus of the RBC membrane and increased susceptibility to pneumolysin, the *Streptococcus pneumoniae* pore-forming toxin, was found [27]. Characterising RBC morphology using the absorption of UV light by haemoglobin has also been previously used in this laboratory [81].

2.2.5 Epsilon toxin-induced RBC haemolysis

A small amount (1-5 µl) of whole blood from healthy volunteers was taken using a finger prick lancet. Each volunteer was provided with a participant information sheet in order to give their written informed consent (blank copies can be seen in Appendix 1). The participant information sheet was made in accordance with The University of Exeter Department of Physics and Astronomy Research Ethics Committee (reference number eEMPS000064). The blood sample was mixed in PBS with 1 % bovine serum albumin (BSA) to make a 5 vol % blood solution, 10 times the final concentration. This stock solution was aliquoted into Eppendorfs as the base for each sample.

The toxin, diluted in PBS, was added to the sample Eppendorfs and moderately mixed by gentle pipetting up and down approximately five times. The final sample concentration was 10 µM Etx, 0.5 vol % blood, and 0.1 weight % BSA in PBS. At the time of toxin addition to the first sample Eppendorf, the clock was started.

Phosphate buffered saline (PBS) was used as a negative control. Toxin variants were added to vials containing whole blood in BSA/PBS and mixed well. 15 µl of the mix was immediately transferred from vials to a microscope slide well which was placed in a stage-top incubator (for the 37 °C experiments). At each time point 5 different images were taken of each of the wells. This resulted in 5 images per variant per time point, and approximately 200 cells were captured in each image. The mean and standard deviation of % haemolysis was calculated from the five images and this value represents one repeat. The final values were calculated by taking the mean of at least three repeats.

2.2.5.i   RBC absorbance profiles

RBCs are packed with the protein haemoglobin, which absorbs UV light (wavelength of 415 nm). The absorbance of light changes across the diameter of the cell due to

changes in local cell thickness. This can be described using an absorbance profile which is obtained by plotting cell thickness against cell diameter, thus describing the changes in cell shape in the stages approaching haemolysis. Once haemolysis occurs, the cell appears as an empty ghost cell.

The radial absorbance profiles were calculated using a python script created by Jeremy Metz (University of Exeter, 2016) which uses the below equation to deduce the amount of light absorbed by the haemoglobin:

$$A = -logT = -log\left(\frac{I}{I_0}\right) = log\left(\frac{I_0}{I}\right) = \varepsilon lc \qquad (2.1)$$

Where A is the absorbance of light, T is the transmission of light, I_o is the initial light intensity (taken from outside of the cell) and I is the intensity of light coming through the cell. The extinction coefficient constant of the haemoglobin is represented by ε, the length that the light travels through the cell is l, and c is the haemoglobin concentration.

2.2.5.ii Room temperature experiment

A chamber was created on a microscope slide by placing two strips of parafilm between the slide and the coverslip and sealing by melting the parafilm slightly, leaving a hollow chamber. To fill the microscope slide chamber, 60 µl of the sample mixture was pipetted in from the side by placing the tip on the slide, touching the coverslip and allowing capillary action to draw the solution under the coverslip. The slide was inverted to allow red cells to settle on the coverslip. A separate slide was used for each sample. Cells were viewed with an Olympus IX50 inverted microscope (Olympus Optical, Hamburg, Germany), 60 x water objective, and an ultraviolet (UV) light source (ThorLabs) at 415 nm, which was switched off between images to limit cell damage. Images were taken every two to five minutes using an AVT Stingray F-145B camera.

2.2.5.iii Temperature change experiment

To maintain a temperature of 37 °C, a stage top incubator with a lid and glass windows was used. As only one microscope slide can fit inside the incubator, a slide with multiple wells (Ibidi 18 well µ-slide, Figure 2.3) was used instead of a separate slide for each variant.
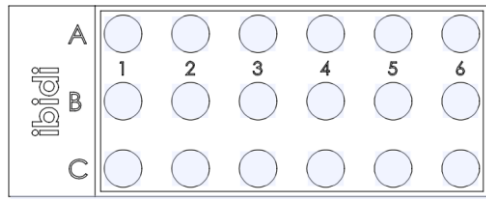
Figure 2.3 18-well microscope slide used (Ibidi).

To fill individual wells, 30 µl of each sample mixture was transferred using a pipette. The slide was immediately placed inside the stage top incubator which had been pre-heated to 37 ºC. At this point the temperature of the objective was set to 37 ºC using an attached objective heater, to limit heat loss through contact with the objective. Each sample well was imaged every 10-20 minutes for the next hour, and again at 120, 180, and 240 minutes.

For both the room temperature and the 37 ºC experiments, five images from different areas of the slide were taken, per measurement, to reduce variation due to any uneven distribution of cells on the slide. The number of ghost cells were counted by eye and the number of viable cells were counted using a python script (Jeremy Metz). The percentage of ghost cells were calculated, averaged, and plotted against time to create the lysis curves.

2.2.6 Electrophysiology with bilayer and epsilon toxin experiment

The technique of lipid bilayer electrophysiology, or black lipid membranes, was described by Mueller et al., [82] and developed further by Montal and Mueller et al., [83]. It allows measurement of the electrical properties of a lipid bilayer by placing electrodes in an aqueous buffer on either side of the bilayer (Figure 2.4). This experimental design was used to probe for pore-formation in a bilayer by detecting a current through the bilayer. In this study, we used a PTFE cuvette with two compartments divided by a Teflon film containing a 50 – 100 µm hole as shown in (Figure 2.4).
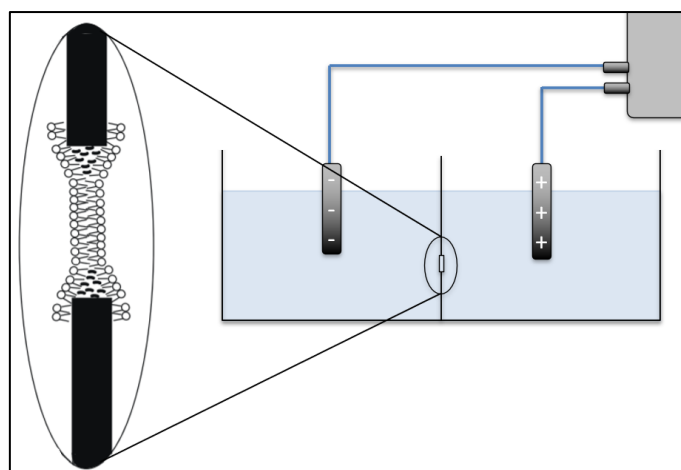
Figure 2.4 Electrophysiology cuvette schematic. Two compartments divided by a Teflon film. A small hole (50 – 100 µm) in the Teflon film allows for the flow of ions between compartments until it is blocked by the lipid bilayer. Schematic built upon from Yeagle [84].

The cuvette was cleaned thoroughly before each use by soaking for 1 hour in Hellmanex® III (Hellma®) followed by copious rinses in MilliQ water and acetone. Any aqueous droplets were dried off using nitrogen gas. To aid adherence of lipids to the edges of the hole, 5 µl of 2 % hexadecane in pentane was applied to both sides of the hole in the parafilm and the pentane allowed to evaporate for 5 – 10 minutes.

The Teflon film was surrounded by 850 µl of an aqueous buffer (1 M KCl, 5 mM 4-Morpholineethanesulfonic acid monohydrate (MES) buffer (A16104, Alfa Aesar), pH 6) (Table 2.1) at room temperature in each side of the cuvette. A monolayer of 5 µl of DPhPC lipids was formed on the surface of the buffer and the pentane allowed to evaporate for 5 – 10 minutes again. Separate glass syringes and metal needles were used for hexadecane and for lipids.

The bilayer was formed by lowering and raising the level of the buffer so that the lipid monolayers on the aqueous surface are deposited over the hole when the aqueous buffer reaches the level of the hole. A voltage of 50 mV was applied while forming the bilayer to see when a bilayer successfully formed as the current reading drops to 0 when the lipids block the hole.

Etx was added gradually to the solution, with more added if a pore did not form within a reasonable timeframe (30 – 60 minutes). Approximately 3 – 10 µl activated Etx was

added to the buffer on the cis side of the membrane to make a total toxin concentration of 0.1 – 0.8 µM in solution. The solution was mixed by pipetting up and down gently several times. No voltage was applied during toxin application in order to reduce instability of the bilayer during mixing. The cuvette was placed in a Faraday cage to minimise noise from external electric fields in the room, and 50 mV was applied to the chambers via silver-chloride electrodes (Figure 2.4). These electrodes were attached to an amplifier and a digitizer so that the applied voltage to the probes could be manipulated and the resulting current recorded using Clampex 10.7 software.

A pore is implicated when a current is observed through the bilayer. From the current, the conductance of the pore was calculated using:

$$G = {}^I\!/\!_V \qquad\qquad (2.2)$$

where G is conductance (Siemens), I is current (Amps) and V is voltage (Volts).

2.2.6.i Electrophysiology reagent preparation

Hexadecane stocks were prepared at the concentration of 2 % hexadecane in pentane. 1960 µl of pentane was measured out using a glass syringe with a metal needle. 40 µl of hexadecane was added to the pentane and the resulting 2 ml was divided into glass vials using a Pasteur pipette. These stocks were stored at -20 °C. Lyophilised lipids (Avanti, Polar Lipids Inc.) were solubilised in pentane to make a concentration of 5 mg/ml. The lipid solution was aliquoted into glass vials and stored at -20 °C as with the hexadecane.

An MES buffer with KCl was chosen because it has higher conductivity than the more commonly used PBS buffer and because it has been used previously with Etx and bilayers [56]. DPhPC lipids were chosen because these are commonly used in lipid bilayer studies due to fact that despite being saturated, their properties mimic that of unsaturated lipids. Therefore, the bilayer is less stiff than would be with most saturated lipids. It is the methyl (CH_3) side groups along the acyl chains that make for this more fluid property (Figure 1.5).

Table 2.1 MES buffer preparation - 1 M KCl at pH 6 with 5 mM MES:

Ingredients	Molar concentration	Weight to make 1 L solution	Weight to make 250 ml solution
KCl (74.55 g molar mass	1 M	74.55 g	18.64 g
MES (195.24 g molar mass)	5 mM	976 mg	244 mg
MilliQ water to volume			
KOH to pH 6			

2.3 Langmuir trough chitosan experiments

This section begins the second part of the project which is to look at the interaction of the polysaccharide, chitosan, on cell membranes. These investigations were largely conducted on lipid monolayers using a Langmuir trough. The two main experimental approaches used were basic Langmuir trough experiments measuring visco-elasticity of the monolayers (discussed in this section) and x-ray synchrotron experiments measuring the structure of the monolayers (covered in the section 2.4). This section describes the methods used to address objective 3 (to characterise chitosan induced changes in surface pressure and viscoelasticity of lipid monolayers, using a Langmuir trough).

2.3.1 Lipid membrane models

Due to the amphiphilic nature of lipids, they can form spontaneous bilayers or micelles in solution. Reproducible experimental procedures have been developed on these structures to model the behaviours of lipids of the cell membrane. Common biophysical methods to investigate macromolecules interacting with lipid membranes involve the use of lipid vesicles, supported lipid bilayers, and monolayers (Figure 2.5) [9].
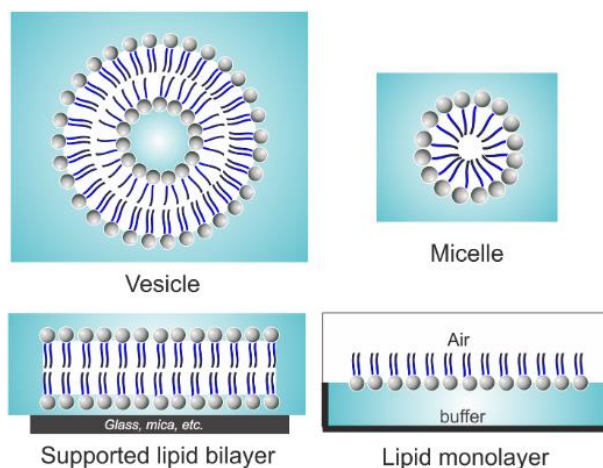
Figure 2.5 Four common models used to study the biophysics of protein-lipid interactions [9].

2.3.2 Monolayers as models for cell membranes

The use of phospholipid monolayers spread on aqueous subphases in laboratory investigation enables close study of specific interactions by mimicking a component of a cell membrane without the complexity of a double layer of lipids and the presence of membrane proteins.

Phospholipids are amphipathic, composed of a polar, hydrophilic headgroup and (a) hydrophobic tail(s). Lipids dropped on to an aqueous surface will naturally form a layer on the air/water interface which is held together in tension by a balance of forces: the hydrophobic forces lining up the lipids to keep their tail in the air, attractive interactions between water and the headgroups, and the steric repulsion between the lipids. If the lipid headgroups are charged, then electrostatic interactions would add to the picture. This monolayer, confined in 2D, can be manipulated by compressing the film with moving barriers resulting in surface area changes and associated changes in surface pressure.

Measuring the surface pressure gives an indication of the physical state of the monolayer. When the pressure is low, there is a large space available to every molecule and the film exists in a gas phase, in which lipids can diffuse freely. At higher pressures the monolayer transitions to more condensed phases, which could include liquid and solid phases, in which the mobility of lipid molecules is restricted. Phase

53

changes, especially in homogenous monolayers, can occur when the pressure reaches a certain point.

2.3.3 Langmuir trough method

Using a Langmuir trough, lipid monolayers can be compressed laterally and resultant changes in surface pressure measured. A single lipid species or a mixture of lipids can be used to form monolayers, and membrane-active molecules can be injected into the subphase underneath the monolayer to investigate their interaction with the lipids, and any resulting changes in their physical state and organisation. A caveat to the monolayer model system is that, while the monolayer is half the depth of a bilayer, the physical interactions of membrane-spanning proteins will be less accurately modelled.

The area of the lipid monolayer can be decreased by moving the trough barriers towards each other. This allows measurement of the dependence of the surface pressure on the monolayer lateral area, which gives valuable information about the state of the monolayer, such as lipid packing and viscoelasticity.

Lipids in the monolayer will not necessarily pack uniformly. Depending on their packing (i.e. the available area), the lipids may form various phases (Figure 2.6) [85]. As the area decreases, the lipids go through different phases (Figure 2.6) towards a more ordered state [85, 86].

Lipids spread over a large area will be in a gaseous state and as the area decreases, pockets of lipids are pushed together and begin condensing into the so-called liquid expanded state (Figure 2.6). During the transition, the surface pressure does not change in a constant manner as is illustrated in the compression isotherm (also referred to as a pressure-area isotherm) in Figure 2.6. Pressure increases to a point then it remains level as the area per molecule decreases and rises rapidly when the state transition of all the lipids occurs [85]. The level segments represent a mix of two phases. The domains of the more ordered phase form microdomains amongst the liquid phase [87]. This pattern follows with the transitions to tilted condensed and untilted condensed phases. Different phases can be identified by inspecting the pressure-area isotherm.

The picture is even more complex if the monolayer is multicomponent, with various lipid types; in this case phase separation can occur with micro-domains of different composition, producing a more gradual overall increase in surface pressure.

54
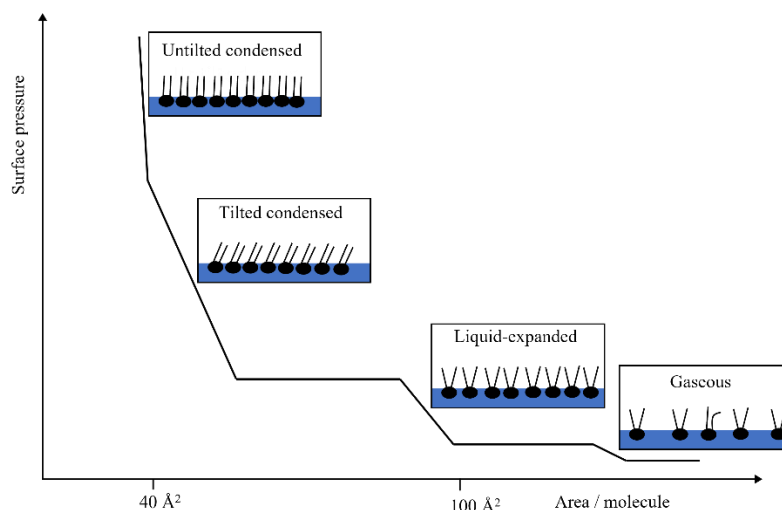
Figure 2.6 Example compression isotherm: phase transitions of a typical lipid monolayer as the area is decreased.

The static dilatational elastic moduli can be obtained when the compression isotherm is conducted very slowly. The dynamic dilatational elastic moduli can be deduced by recording the surface pressure relaxation after a sudden decrease in area. Established rheological calculations can be applied to this experimental data to obtain viscous and elastic contributions to the monolayer re-establishing an equilibrium.

A complementary, qualitative observation can also be used to inform the observer of the type of interaction occurring with the monolayer and the solute: a rise in pressure may represent insertion into the membrane [79], or a decrease in pressure could represent loss of lipids from the monolayer as a result of an interaction with a solute in the subphase.

The surface pressure can be adjusted to a particular value before adding a solute in the subphase, to see if the state of the membrane (e.g., lipid packing and viscoelasticity) affects absorption. Several studies have tried to characterise which monolayer surface pressure best represents a biological membrane and results range between 25 and 35 mN/m [84, 88-92].

The Langmuir trough is therefore a useful technique for monitoring solute-lipid interactions as well as the effect of monolayer elasticity, and monolayer lipid species composition on susceptibility to membrane-active molecules.

2.3.4 Langmuir trough

Generally, a trough made of a hydrophobic material is filled with pure water or a suitable buffer as the subphase. Lipids mixed with a volatile solvent e.g. chloroform are added on top of the clean surface and spread out as the chloroform evaporates [86]. The trough was set up as shown in Figure 2.7 with an aqueous subphase and a Kibron dyne probe. Two barriers sit over the trough so that they are just making contact with the subphase. These barriers can be moved back and forth. A small magnet was situated on the trough floor with a spinning plate below to encourage gentle mixing of the subphase. A probe hangs down (so it just touches the aqueous surface) which measures the surface pressure.
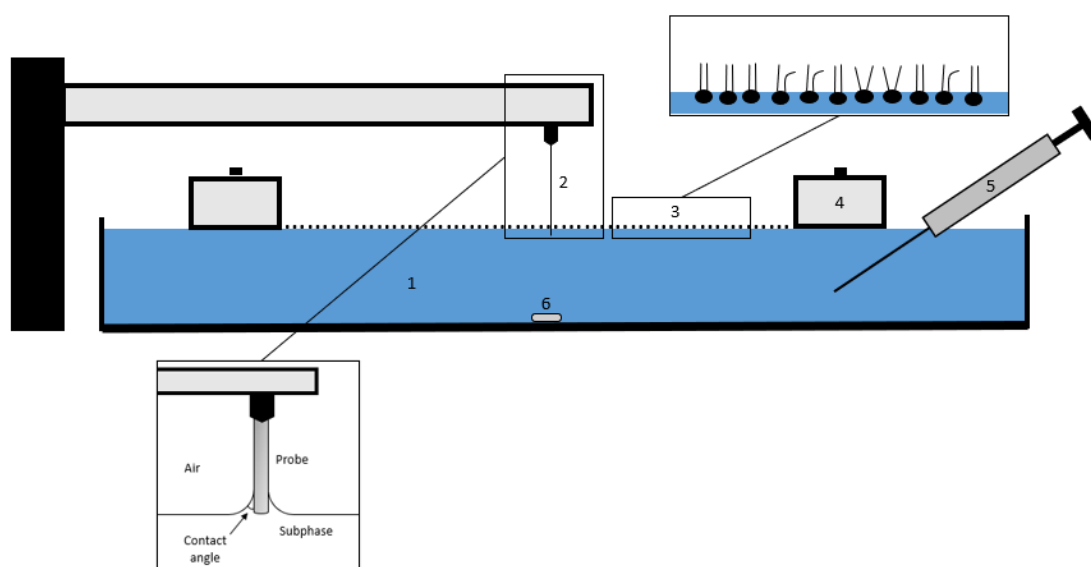
Figure 2.7 Langmuir trough schematic with the experimental set up. 1) aqueous subphase in the trough, 2) platinum pressure probe, 3) monolayer of phospholipids and inset showing hydrophilic headgroups touching water, 4) movable barriers, 5) syringe to inject chitosan, 6) spinning magnet to mix chitosan into the subphase.

The Kibron dyne probe has a smooth surface which allows water to creep up the sides ensuring there is a negligible contact angle with the probe. The surface tension pulls on the probe and this force is measured by a high precision balance in the Kibron equipment. Surface tension, γ, is then calculated using the force, f, and the known perimeter, l, of the probe (1.60 mm):

$$\gamma = f / l \qquad\qquad (2.3)$$

The surface pressure of the film, π, is calculated using the known surface tension of pure water, γ_0, and the measured surface tension of the film:

$$\pi = \gamma_0 - \gamma \qquad\qquad (2.4)$$

2.3.5 Monolayer set up

Lipids dissolved in chloroform were dropped onto a clean pure water subphase and left to spread, and for the chloroform to evaporate, for approximately 30 minutes. 1 mg/mL lipid mixtures representative of the composition of the RBC inner and outer leaflets (Avanti Polar-Lipids) were used (Table 2.2) [93]. The trough temperature was maintained at 20 ^{o}C using a heat bath and water circulation channels within the baseplate. For each experiment, several compression isotherms were performed to check there were to artifacts affecting the measurements.

Table 2.2.Constituents of lipid monolayer mixtures representing the components of the inner and outer leaflets (IL and OL respectively) of RBC membranes.

Lipid or sterol	Full name	Molecular weight (MW) [g/mol]	IL Mole %	OL Mole %
Cholesterol	Cholesterol	386.65	19.6	20
DPPC	1,2-dipalmitoyl-*sn*-glycero-3-phosphocholine	734.039	11.8	31
DPPE	1,2-dipalmitoyl-*sn*-glycero-3-phosphoethanolamine	691.959	38	9
DPPS	1,2-dipalmitoyl-*sn*-glycero-3-phospho-L-serine	757.95	22.3	1
SM	N-palmitoyl-D-erythro-sphingosylphosphorylcholine	703.028	8.3	39

2.3.6 Chitosan preparation

Low molecular weight chitosan (50-190 kg/mol) (75-85% deacetylated) (Sigma-Aldrich) stock solution was prepared to a concentration of 10 g/L in Milli-Q water and

HCl was added to pH 5.5 to dissolve the chitosan. The solution was stirred at 50 °C for 2 hours and stirred overnight at room temperature. The final state of chitosan in the weak acid solution would include protonated amino groups on the deacetylated moieties, and therefore it would have a net positive charge.

2.3.7 Chitosan application to phospholipid monolayer

The lipid monolayer was compressed to a target surface pressure and left for at least 20 minutes to equilibrate before chitosan solution was injected into the subphase using a long, flexible needle and syringe (Hamilton) to reach under the barrier, so that the lipid monolayer remained undisturbed. The injection was close to a stirrer bar magnet spinning at 16 rpm to distribute the chitosan. After addition to 100 ml water subphase in the Langmuir trough the total concentration in the subphase was 1.26 x10^{-8} M. The pressure was monitored for approximately 1 hour after chitosan injection. Static and dynamic measurements were taken before and after chitosan addition to observe any changes in static or dynamic elasticity, respectively.

2.3.8 Monolayer measurements and calculations

2.3.8.i Static dilatational elastic modulus

The compression isotherm was used to calculate the monolayer static dilatational modulus. Here, the rate of compression is so slow that the monolayer is assumed to be static. The term 'static' is used in this thesis for simplicity, however, a more accurate term may be 'quasi-static', where the acceleration and inertial components are deemed unimportant due to the exceedingly slow rate of compression. The monolayer static dilatational modulus, ε, was calculated as a function of the surface pressure, π, and the area, A, as:

$$\varepsilon = -A\frac{d\pi}{dA} \qquad (2.5)$$

The static dilatational moduli results were generated using Matlab (R2017a) with a script written by Sowmya Purushothaman (2016).

2.3.8.ii Dynamic dilatational elastic modulus

The dynamic dilatational modulus, was calculated using the monolayer relaxation after a sudden, small decrease in area, resulting in a small ramp of the surface pressure. The quick compression (which takes approximately one second) causes the surface

pressure to increase and then gradually decrease as the system relaxes back to equilibrium, whilst the area is kept constant. The relaxation involves fast (elastic) and slow (viscous) processes and can be described by exponential relaxation:

$$\Delta\pi(t) = A_1 \exp\left(-\frac{t}{\tau_1}\right) + A_2 \exp\left(-\frac{t}{\tau_2}\right) + \Delta\pi_\infty \qquad (2.6)$$

where $\Delta\pi(t)$ is the change in pressure at any time (t), A_1, A_2 etc., are pre-exponential factors, and τ_1, τ_2 etc., are the corresponding relaxation times for the different processes taking place [94].

The dynamic dilatational modulus, E, can then be obtained by Fourier transform:

$$E\ (v) = \frac{F\left\{\frac{\mathrm{d}\Delta\pi(t)}{\mathrm{d}t}\right\}}{F\left\{\frac{\mathrm{d}ln\,A}{\mathrm{d}t}\right\}} \qquad (2.7)$$

where E is the complex dynamic dilatational modulus and v is the frequency.

The dynamic dilatational modulus is a complex number with two parts, corresponding to the elastic (E_R) and viscous (E_{IM}) processes. These processes are referred to as the storage (E') and loss (E") moduli, respectively. These can then be used to calculate the tangent of the phase angle, tan φ, to determine whether the relaxation is predominantly elastic or viscous:

$$\tan\varphi = \frac{E_{IM}}{E_R} \qquad (2.8)$$

where E_{IM} is the imaginary part of the complex dilatational modulus (the loss or viscosity modulus), and E_R is the real part (the storage or elastic modulus). If tan φ < 1 then it is predominantly elastic and if tan φ > 1 then it is more viscous. This method of data analysis was implemented using Kibron dilatational rheology software module (Firmware Version 4.0 on Windows 10).

There are several models to describe the storage and loss moduli contributions of a 2D film and the standard linear Maxwell solid model (Figure 2.8) is the most appropriate to describe this dynamic elasticity method, i.e., a single, sudden change in area followed by an exponential relaxation period. The storage modulus can be

plotted against the loss modulus to form a Cole-Cole plot, which allows clear visualisation of the contributions of elasticity, E, and viscosity, η, in a standard linear Maxwell solid model [94, 96].
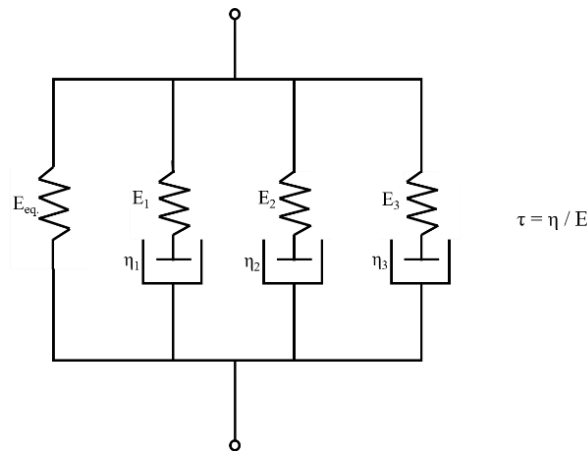
Figure 2.8 Diagram for the generalized linear Maxwell solid model, with the elastic, E, and viscous, η, elements. $E_{eq.}$ is the equilibrium elasticity, as the elasticity of a monolayer does not decrease to 0.

Each spring and dash pot represents one relaxation process, τ, by:

$$\tau = \eta / E \qquad\qquad (2.9)$$

The relaxation processes which are relatively fast will be due to a predominant elastic contribution and conversely the relatively slow relaxation processes will represent a predominantly viscous contribution. The relation experiments were performed over the short timescale of 600 seconds, however, with good exponential fits, estimations of frequencies as small as 10^{-5} /s can be made [94]. There is some compromise of accuracy, however, previous techniques to measure these frequency ranges, such as by sinusoidal barrier movements, would take repeat periods of 10 000 seconds each, during which evaporation would have a large compromising effect on the data.

2.4 Synchrotron chitosan experiments

This section also uses the Langmuir trough equipment to form the lipid monolayers; however, it is the synchrotron experimental set-up that is the central point to this section. The following methods were used to address objective 4 (to obtain structural information of the interaction of lipid monolayers with chitosan using x-ray techniques).

2.4.1 Chitosan preparation

Chitosan was prepared to 10 g/L stock solution using the method in section 2.3.5.

2.4.2 Lipid monolayer

Lipid monolayers were made up of mixtures of lipids that represent the composition of the inner or outer leaflets of RBC membranes, as used in section 2.3.5 (Table 2.2). A lid was secured over the Langmuir trough and helium pumped into the gas volume to minimise oxygen content in the gas above the monolayer and prevent artifacts. The Langmuir trough temperature was maintained at 20 °C.

2.4.3 Chitosan-lipid interaction measurements

Compression isotherms were obtained by reducing the area of the film until a pressure of 40 mN/m was reached and then the barriers were relaxed until pressure 0. This was repeated at least once. The monolayer was then compressed to 30 mN/m and the barrier motors set to maintain this pressure whilst x-ray reflectivity (XRR) and grazing incidence x-ray diffraction (GIXD) measurements were conducted. Chitosan was added by injecting 50 μl into the subphase through the monolayer in the area where the beam would focus, using a metal needle and syringe. Any subsequent changes in area or pressure were recorded over time as this would indicate interaction of the chitosan with the monolayer. During chitosan addition, and subsequent equilibration time, the barrier motors were turned off so that any change in pressure could be monitored.

The motors were then turned on to return the monolayer to 30 mN/m before starting the first set of XRR and GID measurements on the monolayer with added chitosan. The second set of XRR and GID measurements were made after the monolayer was expanded to 0 mN/m and recompressed back to 30 mN/m, to see if chitosan incorporated into, or re-arranged the monolayer differently after an expansion and compression cycle.

2.4.4 X-ray methods background

X-ray reflectivity (XRR) studies measure the intensity of a reflected x-ray wave from a surface. In order for this wave to be informative about the structure of the surface, there must also be a wave that transmits through the surface. There is no transmission wave when the angle of incident, α_i, is smaller than the critical angle for total reflection, α_c (Figure 2.9A). Therefore, the angle of incident for these experiments was slightly

larger than the critical angle so there is an external, reflected wave, as well as an internal, transmitted wave (Figure 2.9C).

A) Incident angle < Total reflection critical angle
All incident X-rays are reflected.

B) Incident angle = Total reflection critical angle
Incident X-rays propagate along the sample surface.

C) Incident angle > Total reflection critical angle
Incident X-rays penetrate into the material by refraction
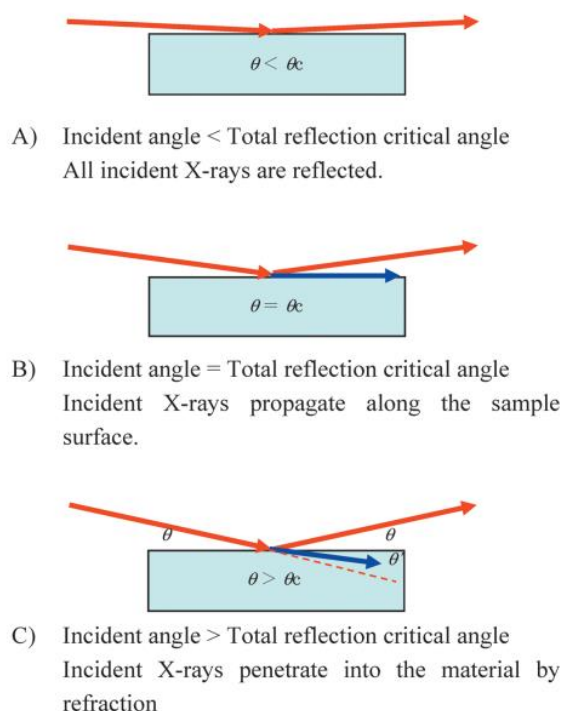
Figure 2.9 X-ray reflection conditions with different incident angles. Symbol θ represents the incident angle and θ_c represents the critical angle for total reflection [97].

Refraction of a wave occurs when it travels from a medium of one refractive index to a medium of a different refractive index. The monolayer acyl chains will form a layer with one refractive index, and the headgroups will form another layer of different refractive index and then the aqueous subphase has another refractive index again. Therefore, the incident x-ray will refract each time as it encounters the acyl chains, headgroups, and the subphase of our sample.

Diffraction of the x-rays could occur when a wave almost parallel to the monolayer surface interacts with the lipid acyl chains. This can give information about the surface, such as lattice structure and tilt angle of the lipids. In grazing incidence x-ray diffraction, GIXD, x-rays are focussed on the monolayer at an angle very close to the critical angle. This angle allows total external reflection of the x-ray beam and incidence wave propagation along the surface plane (Figure 2.9B). From the obtained diffraction pattern, insights into the in-plane structure of the acyl chains can be

deduced. GIXD is most sensitive to the acyl chain region of the lipids and can reveal the lateral 2D order in the monolayer and acyl chain tilt angle.

2.4.5 X-ray measurements of chitosan-lipid interaction

X-ray measurements were conducted at the European Synchrotron Radiation Facility (ESRF) in Grenoble, France, at the Troika II ID10B beamline, in June 2018. An X-ray beam was directed through a Carbon 1-1-1 monochromator to extract a single wavelength, λ = 1.55 Å (energy of 8 keV, 200 mA). The beam focussed on the monolayer was 100 x 300 µm in vertical and horizontal directions respectively. The Langmuir trough was on an anti-vibration table and not moved during measurements. A double crystal deflector was used because this allows the incidence beam to rotate around a fixed point without moving the sample (Figure 2.10). The reflected beam was detected using a linear position-sensitive detector (PSD, Brucker).
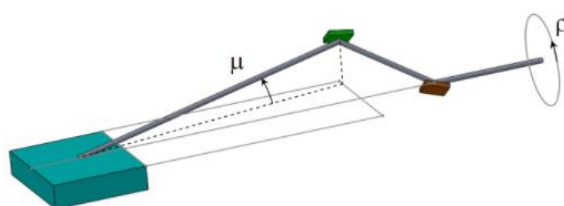
Figure 2.10 Diagram of the double crystal deflector (ID10 beamline overview, [98]).

2.4.5.i XRR

X-ray reflectivity probes the monolayer in the direction of the surface normal, which is equivalent to the z-axis in Figure 2.11. High energy x-rays are directed at the lipid monolayer as an incidence wave represented by vector k_I, and reflect from the molecules as a reflected wave, represented by vector k_R , and k_T is the transmitted wave vector which passes through the medium (Figure 2.11).
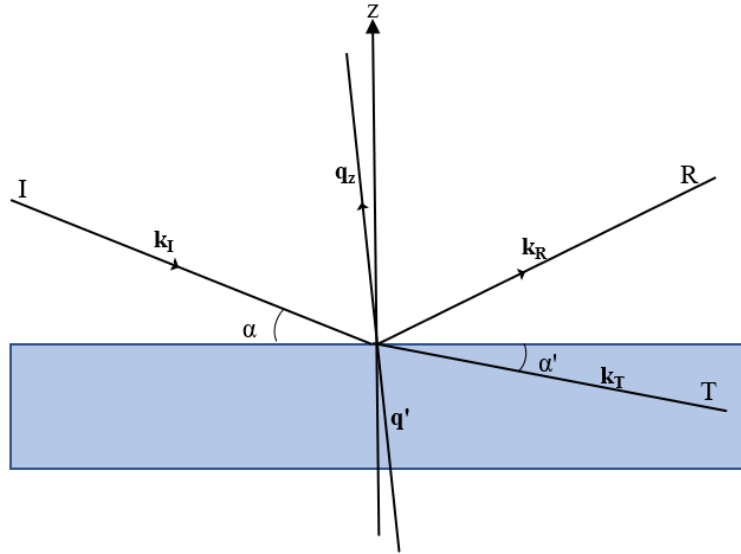
Figure 2.11 Schematic representation of a typical x-ray reflectivity set up.

Reflectivity, *R,* is a function of the ratio of intensity of the reflected wave (related to the wave amplitude a_R) relative to the intensity of the incidence wave (related to the wave amplitude a_I). *R* can also be described as the square of the modulus of the reflection coefficient [99]:

$$R = \left(\frac{a_R}{a_I}\right)^2 = \left|\frac{\alpha - \alpha'}{\alpha + \alpha'}\right|^2 \qquad (2.10)$$

where α represents the angle of incident (which is controlled by the user) and α' represents the transmission angle (which is affected by the absorption properties of the monolayers (such as electron density and refractive index)).

The transmission angle, α', was used to derive the electron density along the z-axis by the following steps: First, each value of *R* was standardised by dividing by the Fresnel reflectivity, R_F, which is the reflectivity of a completely smooth surface calculated using optical laws in the case of x-rays [100]. This allows reflectivity measurements to be compared between experiments in different set ups.

Second, R/R_F was plotted as a function of the scattering vector, $\mathbf{q}_z$ (Figure 2.11) to form the reflectivity curve plots. The plotted data was then fitted using a function of the scattering wave vector through the monolayer, $\mathbf{q'}$ (Figure 2.11), represented by $\phi(q')$. We based our monolayer on a model of three slabs (representing acyl chains, headgroups and the subphase), each of constant electron density, similar to previous

x-ray studies on lipid monolayers [101, 102]. As such, the reflectivity function, $\phi(q')$, contained information on the thickness and refractive index of each slab and a roughness parameter was applied to smooth the boundaries between slabs. Least squares analysis was used to estimate the best fit (software written by Oleg Konovalov, ID10, ESRF).

Further, when the surface interface is not smooth, such as with our monolayers, the fitted reflectivity curve creates a profile of scattering waves, ρ, through the medium, with gradient dρ/dz. The gradient of this profile, was normalised to obtain $1/\rho_{av}$ dρ/dz.

Third, we used the Born approximation - that the square of the Fourier transform of this normalised gradient profile, $1/\rho_{av}$ dρ/dz, represented by $\phi(q')$, is related to $R(q)/R_F$ by the reflectivity master formula:

$$|\phi(q')|^2 = R(q)/R_F(q) \qquad\qquad (2.11)$$

- to derive the electron density along the z-axis, $\rho(z)$ [100]:

$$\phi(q') \equiv \frac{1}{\rho_{av}} \int \frac{d\rho}{dz} e^{iq'z} \, dz \qquad\qquad (2.12)$$

2.4.6 GIXD

2.4.6.i Equipment

The x-ray beam was directed at the monolayers at an angle of 0.1233°, which is slightly lower than the critical angle for total reflection, 0.154°, and the diffracted x-rays were detected with the Mythen 1K detector.

2.4.6.ii Processing Bragg reflections

Bragg reflections are interpreted using the Miller indices, h and k. Bragg peaks were fitted using a Lorentzian distribution, and the parameters of the resulting curve were used to determine the lateral lattice structure of the monolayer. The number of peaks indicate the symmetry of the 2D unit cell. For example, one peak indicates a hexagonal cell and two peaks indicate a distorted hexagonal or rectangular cell. The information for the following equations was gathered from Als-Nielsen *et al.*, (1994) [100].

The distance between lattice points (d-spacing) was calculated using the Bragg equation:

$$d = \frac{2\pi}{q_{xy}}$$

(2.13)

Where q_{xy} is the lateral plane across the sample surface.

Further lattice parameters can be calculated if we first assign Miller indices, *h* and *k*. When two peaks are present in the Bragg pattern, Miller indices are assigned to both peaks where for peak 1 $\{h, k\}$ can be assigned [0,1] or [1,0] and peak 2 $[h, k]$, $\{1, -1\}$.
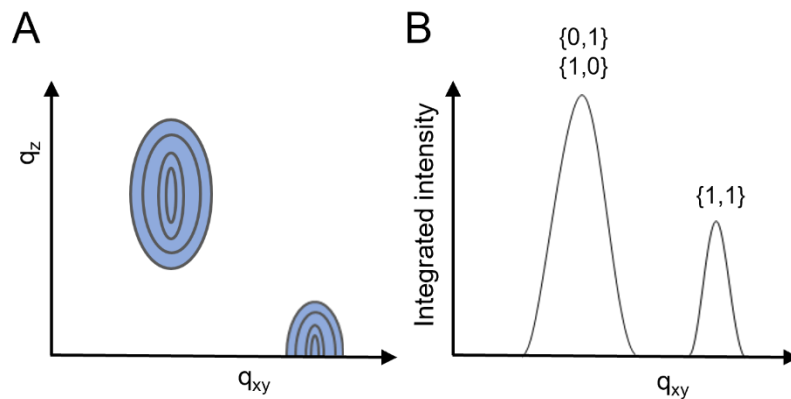
Figure 2.12 Typical Bragg peak pattern. A) Intensity distribution of Bragg reflections and B) Bragg peaks, integrated intensity distribution of the Bragg reflections, with assigned Miller indices.

The unit vectors a and b represent the dimension of 2D unit cells, and these vectors are connected by the angle γ. All three of these parameters can be calculated using Miller indices:

$$d = \frac{2\pi}{q_{xy}} = [h^2/a^2 + k^2/b^2 - 2(hk/ab)\cos(\gamma)]^{-1/2}\sin(\gamma)$$

(2.14)

When there are two Bragg peaks, the cell symmetry can be described as a distorted hexagonal cell where $a = b$ and $\gamma < 120$. For $a = b$, equation (2.14) becomes:

$$a = (2\pi/q_{xy}\, \sin\gamma) \times (h^2 + k^2 - 2hk\, \cos\gamma)^{0.5}$$

(2.15)

The parameter, a, will be the same value if calculated from the peak 1 Miller indices ({0,1}) or ({1,0}) or from the peak 2 Miller indices ({1, −1}). Therefore, either of the Miller indices values can be inserted into equation (2.15) to obtain the same result. Using the peak 1 indices, where $h = 0$ and $k = 1$, to calculate a_{p1} and the peak 2 indices, where $h = 1$ and $k = $ -1, to calculate a_{p2}, we get:

$$a_{p1} = 2\pi / q_{xy_1} \sin \gamma \qquad (2.16)$$

$$a_{p2} = \left((2\pi \times \sqrt{2}) / q_{xy_2} \sin \gamma \right) \times (1 + \cos \gamma)^{0.5}$$

To get γ, simultaneous equations can be used with the two a equations:

$$a_{p1} = a_{p2} \qquad (2.17)$$

$$2\pi / q_{xy_1} \sin \gamma = \left((2\pi \times \sqrt{2}) / q_{xy_2} \sin \gamma \right) \times (1 + \cos \gamma)^{0.5}$$

Which can be solved for γ:

$$\gamma = \arccos \left(\left(q_{xy_2} / q_{xy_1} \sqrt{2} \right) \right)^2 - 1 \qquad (2.18)$$

From the now determined γ, the value of a can be calculated using either of the (2.16) equations.

Using the Scherrer formula [103], the full width half maximum of the Bragg peak was used to calculate the coherence length, L_{xy}:

$$L_{xy} = 0.9(2\pi \, / \, FWHM) \qquad (2.19)$$

3 <u>Epsilon toxin</u>

3.1 Introduction

The aims of this chapter were to characterise haemolytic activity of Etx and to evaluate the importance of selected amino acids in Etx binding, oligomerisation and pore-formation stages on RBC membranes. Specifically, looking at:

- Etx variants with mutations in the receptor-binding domain (Y42A and Y43A)
- and an Etx variant with a mutation to the pore-forming module (H162A)

Etx binding, oligomerisation, pore-formation and haemolysis were studied by incubating toxin with extracted RBC membranes, lipid bilayers, and whole RBCs. I expected to see reduced cytotoxicity to RBCs by Y42A and Y43A, due to impairment of receptor binding but not impairment to hydrophobic binding. All variants were tested with artificial lipid bilayers to check if mutation to these amino acids affected hydrophobic binding and pore-formation.

The working hypotheses in this chapter are:

- that Etx action on a host cell involves three main steps: 1) the binding of monomers to receptors, 2) the synthesis of oligomers, and 3) formation of pores resulting in cell lysis.
- that Etx action on RBCs follows these same steps (but with a different receptor to previously studied cells, CHO-hMAL, and with the addition of a hydrophobic mechanism of binding).
- that the mutations have no effect on hydrophobic binding in lipid bilayers
- that the H162A mutant, which arrests pore-formation after the oligomerisation stage, regains pore-forming ability when the lipid environment is favourable.

3.2 Results

3.2.1 Etx-induced haemolysis in RBCs

Haemolysis of RBCs is marked by a leakage of haemoglobin and the cells can be seen turning from dark to light grey ('ghost cells') when lysed (Figure 3.1, top). Approximately 10 minutes before haemolysis, the RBC radial absorbance profiles (2.1) in Figure 3.1 (bottom), show that the cells swell, decrease in diameter, and become

more rounded, before, relatively suddenly, appearing as a ghost cell, as seen in Figure 3.1 (top) at 22 minutes.
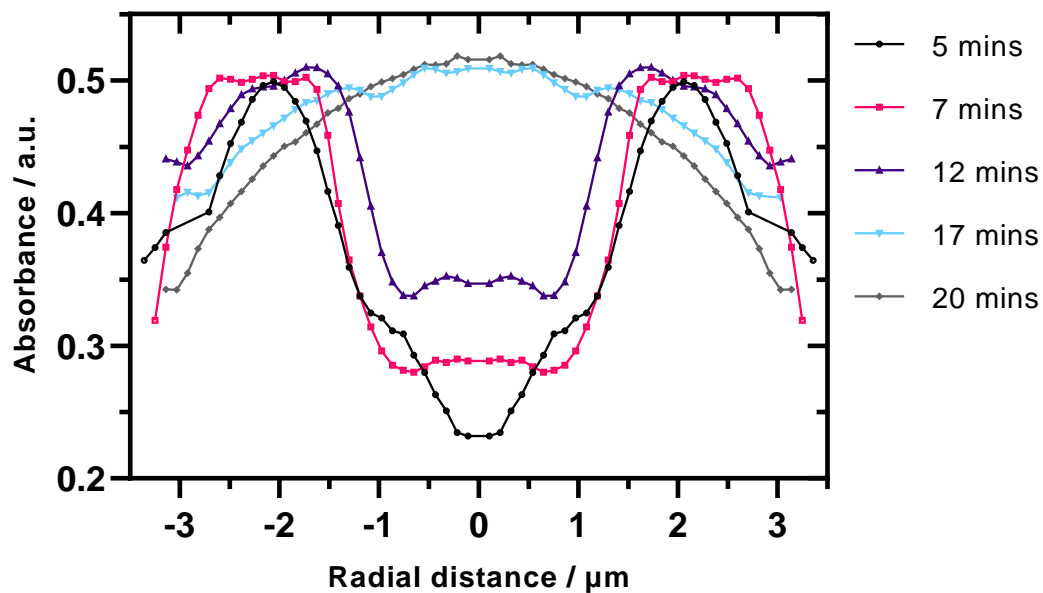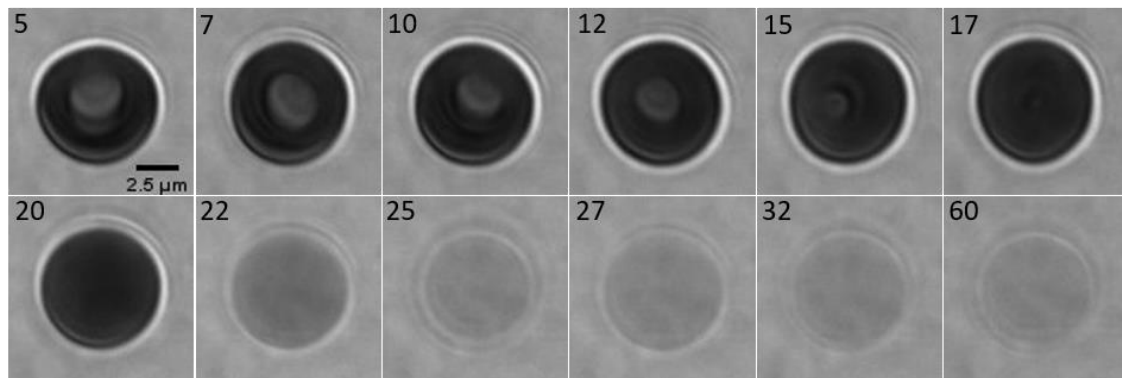
Figure 3.1 Course of haemolytic effect of Etx-WT. Top panel: Images of a single cell between 5 and 60 minutes of incubation with WT Etx. Haemolysis occurs after 20 minutes. Time stamps are in the top left corner of each image. Bottom panel: Absorbance of UV light (equation (2.2) from the cell centre across its radius at increasing time points since addition of WT Etx.

The three Etx variants, Y43A, Y42A and H162A were tested against the wildtype, WT, to establish the relative number of RBCs lysed over a time course of 240 minutes after the addition of 1 and 10 µM toxin, at room temperature and human body temperature, 37 °C (see Methods 2.2.5.ii and 2.2.5.iii).

3.2.1.i Receptor-binding domain mutation - Y42A

Reduced haemolysis was seen after one hour incubation of RBCs with 10 µM Y42A at both room temperature and 37 °C, with (26.2 ± 9.7) % and (61.2 ± 11.1) % haemolysis observed, respectively, compared to WT. Y42A appears non-toxic at room temperature at 1 µM and despite the physiological temperature of 37 °C, 1 µM Y42A caused negligible lysis, compared to WT, after one hour incubation (Figure 3.5).

Y42A exhibited negligible haemolysis at 1 µM concentration until approximately 90 minutes with RBCs at 37 °C (Figure 3.6A). At 10 µM concentration at 37 °C, Y42A haemolysis was significantly lower, with non-overlapping standard error margins, than WT (but higher than H162A) up to 60 minutes (Figure 3.6B).

The Y42A variant is the only one that showed a marked increase in cytotoxicity with a shift from 1 µM to 10 µM (Figure 3.2). In addition, a clear effect of temperature on activity can be seen with 10 µM Y42A, especially towards the start of incubation.
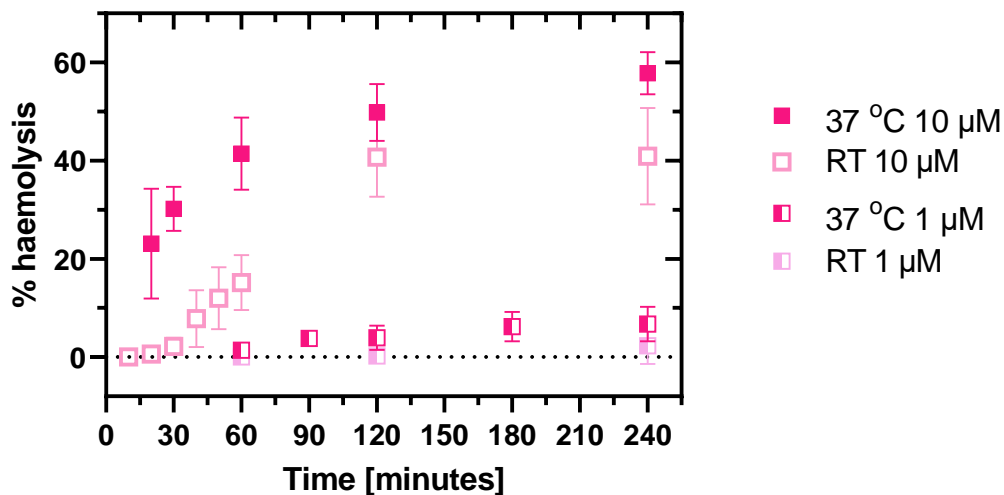
Figure 3.2 Effect of temperature and concentration on the kinetics of haemolysis by the Y42A Etx variant.

3.2.1.ii Receptor-binding domain mutation - Y43A

Y43A and WT showed no significant difference in haemolysis after one hour at room temperature and 37 °C with both 1 µM and 10 µM (Figure 3.5). At almost all timepoints

measured, WT and Y43A showed no significant difference in toxicity and appeared to plateau from 60 minutes (Figure 3.6).

3.2.1.iii Pore-forming module mutation - H162A

H162A caused negligible haemolysis at room temperature even at the higher concentration of 10 µM (Figure 3.5). At 37 °C, percentage lysis by 1 µM H162A was consistently significantly (no overlap in standard error margins) lower than WT but by 240 minutes there was no significant difference between WT and H162A (Figure 3.6A). At the higher concentration, 10 µM, percentage lysis by H162A was still significantly lower than 10 µM WT up to 120 minutes (Figure 3.6B).

H162A showed strong temperature dependence, where activity was only observed at physiological temperature, 37 °C (Figure 3.3). Concentration dependence was not observed when both 1 µM and 10 µM were tested at 37 °C (Figure 3.3).
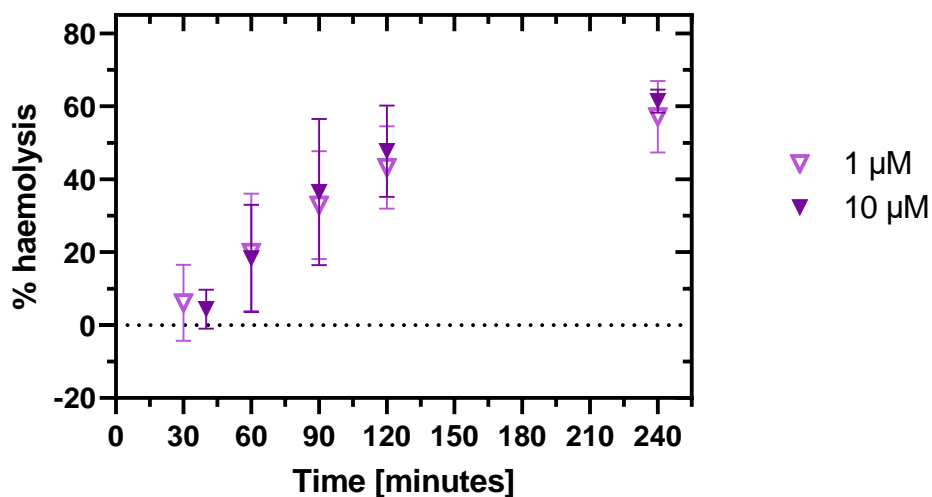
Figure 3.3 Effect of concentration on the haemolytic activity by H162A at 37 °C.

Interestingly, even when H162A was incubated with cells for one hour at room temperature prior to heating to 37 °C, the onset of haemolysis was not necessarily faster than when incubated at 37 °C from the start (Figure 3.4).

71
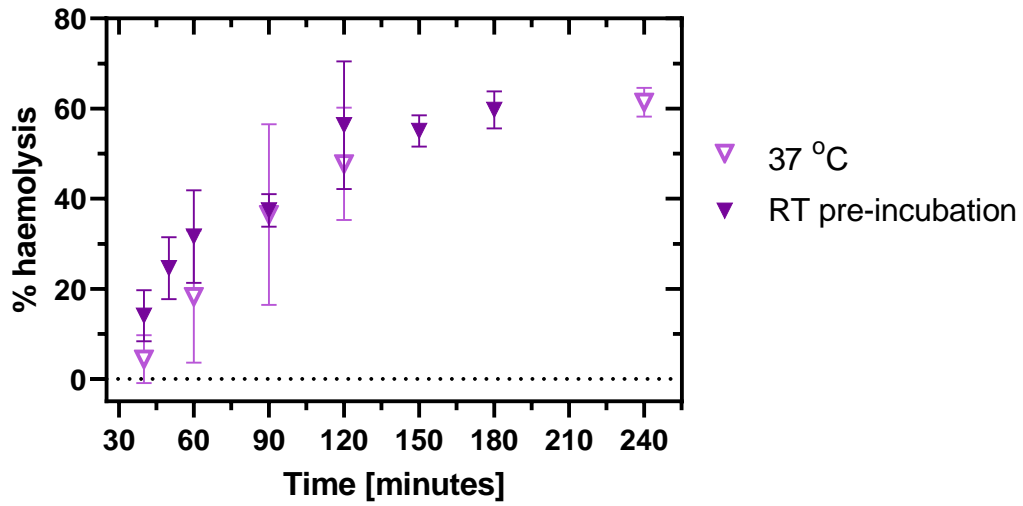
Figure 3.4. Effect of a one-hour thermal pre-treatment, at room temperature (RT), on 10 µM H162A haemolytic activity.
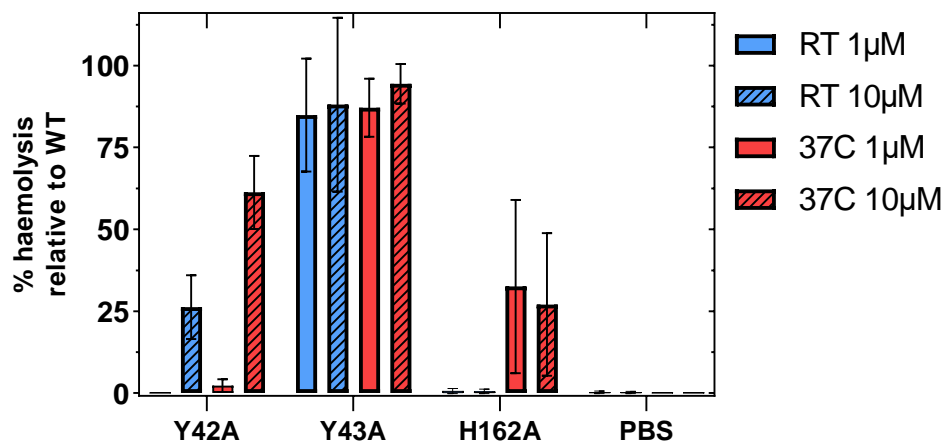
Figure 3.5 Percentage of RBC haemolysis in comparison to WT after 1 hour incubation.
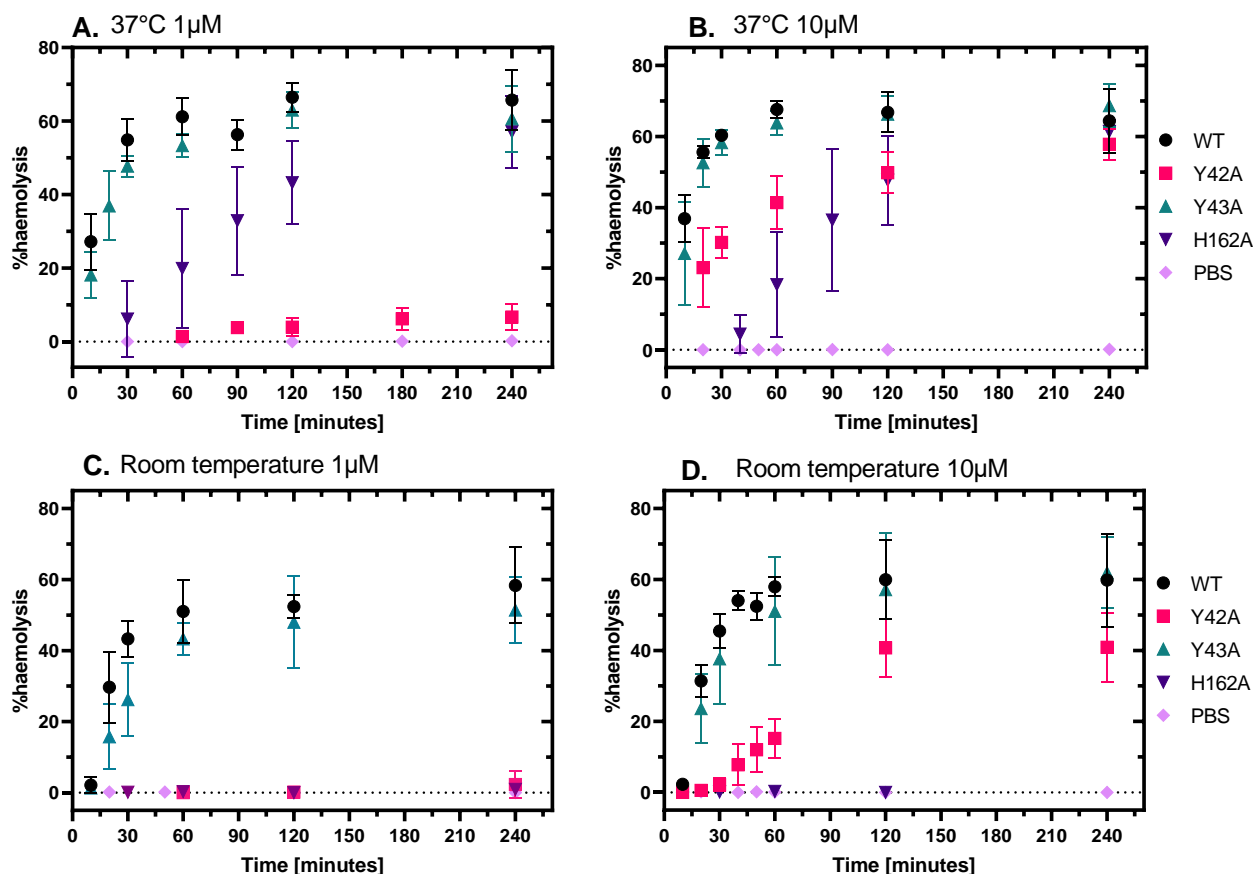
Figure 3.6 Percentage haemolysis by Etx. Cells were incubated at 37 °C with concentrations of 1 and 10 μM Etx (A and B, respectively) and at room temperature with concentrations of 1 and 10 μM Etx (C and D, respectively). Error bars are standard errors of the mean.

3.2.2 Etx binding and oligomerisation

3.2.2.i Brief overview of method

RBC membranes were extracted, and non-activated toxin (P-toxin) was used to test binding, and activated toxin was used to look at oligomerisation (Methods 2.2.3). As Etx binds to a substrate, it moves from soluble to non-soluble, and this technique can be used to detect Etx specifically in the non-soluble fraction. The reason extracted RBC membranes were used, rather than use whole cells, was to ensure we did not detect Etx bound to other cell components.

3.2.2.ii Receptor-binding domain mutation - Y42A

Y42A showed reduced binding to RBC membranes (work in collaboration with M. Bokori-Brown, to be published). A reduction in Y42A oligomerisation can be seen in the western blot (Figure 3.7). Upon quantification by analysis of the band intensity, reduced oligomerisation was indeed observed, at both room temperature (reduced to approximately 30 %) and at 37 °C (reduced to approximately 70 %), compared to WT (Figure 3.8, created by M. Bokori-Brown). There was an increase in oligomerisation by Y42A at 37 °C compared to room temperature (Figure 3.8). These data correspond with the reduced haemolysis seen by Y42A compared to WT, and the increased haemolysis by Y42A at 37 °C compared to room temperature (Figure 3.5).

3.2.2.iii Receptor-binding domain mutation - Y43A

There was no observable difference in RBC binding (work in collaboration with M. Bokori-Brown, to be published) and no significant difference in quantified oligomerisation at room temperature and 37 °C with Y43A (Figure 3.8). These data correspond with no difference in RBC haemolysis, compared to WT.

3.2.2.iv Pore-forming module mutation - H162A

H162A exhibited reduced binding to RBCs at room temp and 37 °C (work in collaboration with M. Bokori-Brown, to be published). The band of H162A oligomers can be seen in Figure 3.7. Oligomerisation by both 1 and 10 µM of H162A was reduced to approximately 50 % compared to WT, for both temperatures tested (Figure 3.8).
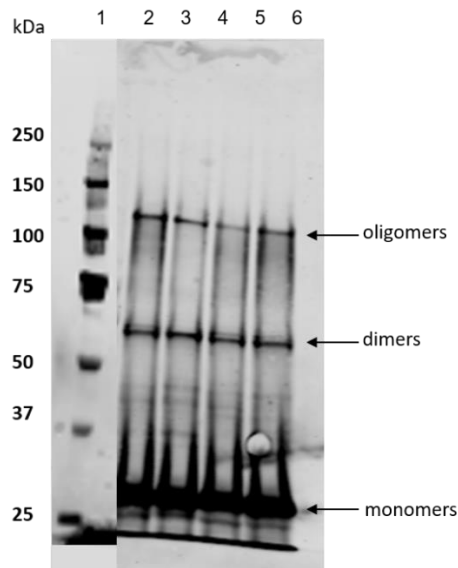
Figure 3.7: Oligomerisation assay at room temperature with 10 µM of each Etx variant: Y42A, Y43A, WT and H162A, using RBC membrane preparations. All variants were activated using a trypsin digest assay. Oligomers can be seen at approximately 130 kDa. Lane 1: Molecular weight marker (with molecular masses labelled to the left); Lanes 2-5: red cell membranes incubated with trypsin-activated Etx wild type, Etx-H162A, Etx-Y42A or Etx-Y43A, respectively; Lane 6: red cell membranes incubated with buffer only.
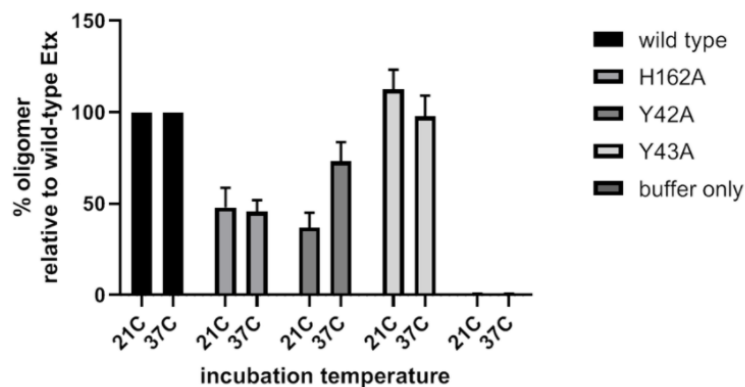
Figure 3.8 Quantified protein amounts from three room temperature and three 37 °C oligomerisation assays on RBC membranes (Figure 3.7). Samples were incubated with 10 µM toxin for 1 hour. This graph incorporates my work (contribution to experimental design and initial laboratory experiments) but was created by Monika Bokori-Brown (contribution to experimental design, initial laboratory experiments and independently conducted final laboratory experiments and quantified protein amounts).

A similar experiment was carried out with our collaborator, M. Bokori Brown, using a CHO cell line engineered to express the MAL receptor (CHO-hMAL). Some of these results were taken into account when considering hypotheses to describe the RBC-Etx interactions. The oligomerisation assay with CHO-hMAL cells showed that Y42A did not form oligomers, that Y43A did not form oligomers at room temperature (however, at 37 °C oligomers were detected) and that H162A oligomerisation was not impaired (Table 3.1).

3.2.3 Comparison of haemolysis curves between individuals

RBCs exhibit natural variability in their response to pore-forming toxins [27], both within the same population of cells and between individuals. It is therefore important to quantify the variability of RBCs susceptibility to Etx. This was carried out on cells obtained from another healthy volunteer. There was some variation seen with the WT toxin where cells from the second individual, 'blood 2', appeared more susceptible (Figure 3.9). Variations between donors could occur simply due to natural differences in blood composition, such as the relative abundance of immune cells in their circulation at the time of donation. No statistically significant difference was observed with Y43A and Y42A variants (Figure 3.9). As these experiments were conducted at room temperature, H162A caused negligible haemolysis.
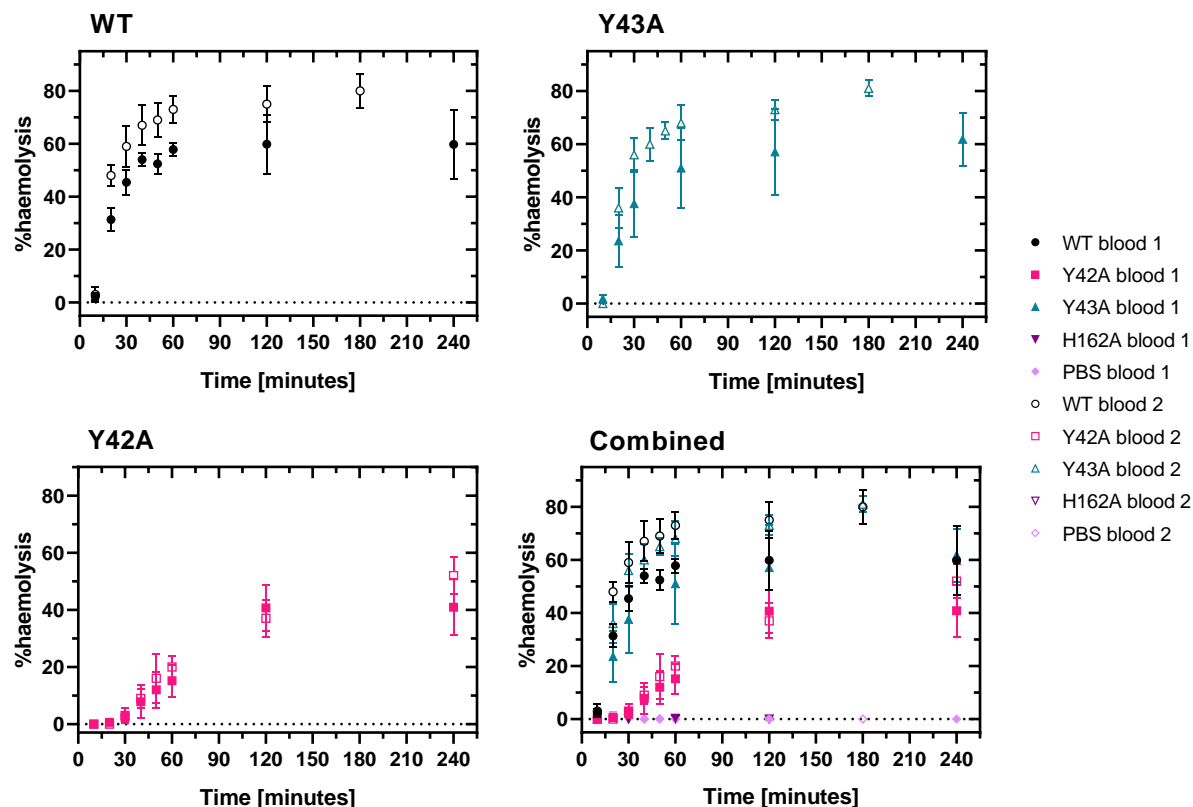
Figure 3.9 Comparison of haemolysis rates of RBCs from two different individuals over four hours. All data were obtained from cells incubated at room temperature.

3.2.4 Electrophysiology of Etx pores in lipid bilayers

Several Etx mutants were tested with this technique (Methods 2.2.6) to see if mutations in the receptor-binding region (Y42A and Y43A) and in the pore-forming module (H162A) effected a hydrophobic-mediated pore-formation mechanism in DPhPC lipids.

Pores began to form in the DPhPC lipid bilayer between 0 and 30 minutes after addition of 0.1 – 0.8 µM activated toxin. Pore formation was probably a stochastic event as there was no clear pattern of time-taken for a pore to form. We observed discrete jumps in current of approximately 25 pA, when 50 mV was applied (Figure 3.10), which was consistent with the conductivity of a single Etx pore in the literature [40, 56].
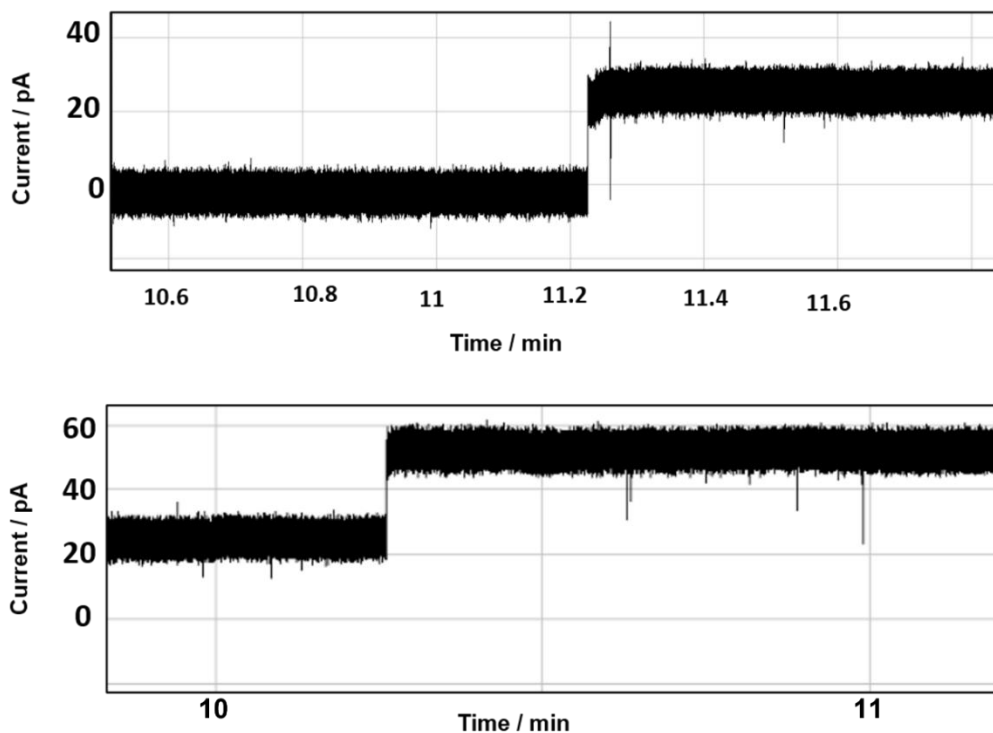
Figure 3.10 Etx pore formation event in DPhPC bilayers. Voltage applied was kept constant at 50 mV once Etx was added to the cis chamber. Top plot shows one pore and the bottom plot shows an additional pore forming.

The voltage applied, and the resulting current of single pores are shown in Figure 3.11A. Voltage was applied in both cis- and trans- directions and the resulting current was slightly weaker in the latter direction, indicating asymmetric accessibility to ions (Figure 3.11B). For example, when 100 mV was applied to the bilayer with a single WT pore, the conductance was (0.57 ± 0.017) nS and when -100 mV was applied, the conductance was (0.47 ± 0.012) nS.
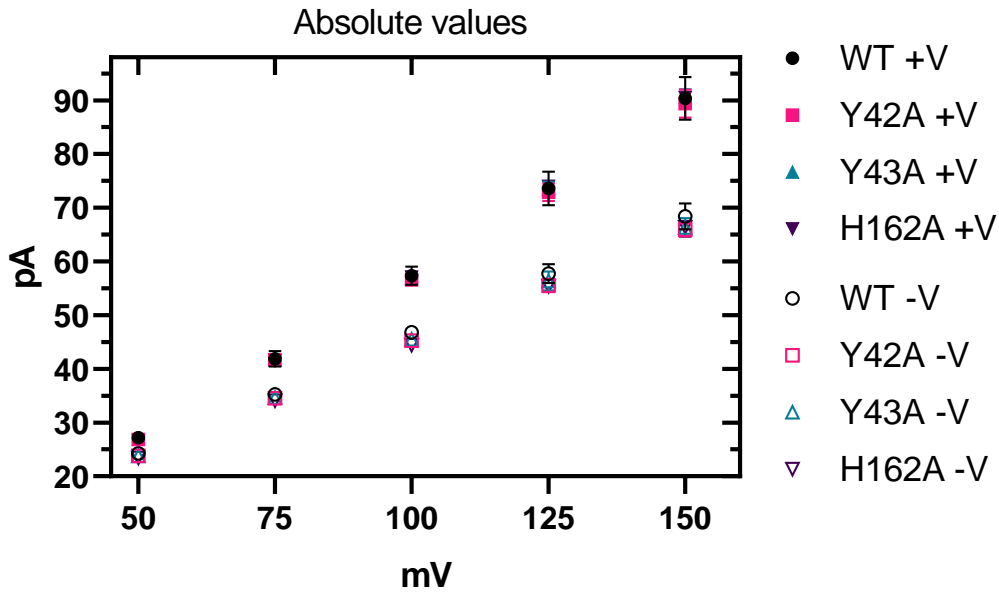
Figure 3.11. Single pore conductance in lipid bilayers over stepwise increase in voltage from -150 to 150 mV. Absolute values of average current plotted to emphasize the asymmetry of current flow. Pores formed by 0.1 – 0.8 µM activated Etx variants in a DPhPC bilayer and data presented with standard error of the mean.

The pore conductance for each applied voltage was calculated (equation (2.2)), showing that there were insignificant differences in pore conductance between the variants over most voltages (Figure 3.12). However, the data do show some variance at lower voltages with the error bars of H162A and WT not overlapping between -100 and -25 mV.
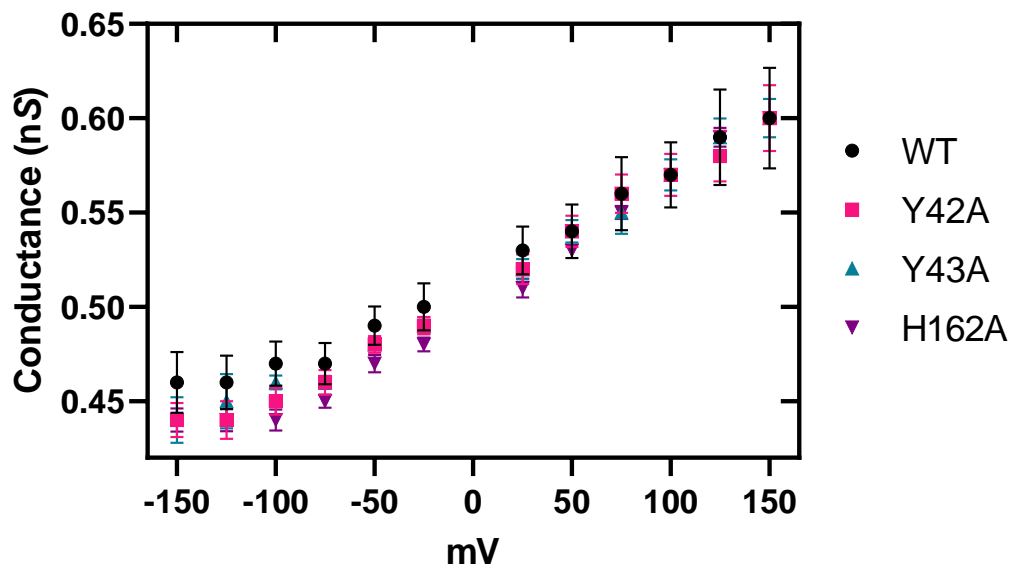
Figure 3.12. Average conductance of a single pore of each variant over stepwise increase in voltage from -150 to 150 mV. Pores formed by 0.1 – 0.8 μM activated Etx variants in a DPhPC bilayer data presented with standard deviation.

3.2.5 Summary of results

A summary of results can be seen in Table 3.1 where results from data collected by Monika Bokori-Brown on CHO-hMAL cells are also included (indicated with MBB initials).

Table 3.1: Summary of Etx oligomerisation, and lytic activity, and the three systems investigated (extracted membranes, whole cells, and lipid bilayers) over various experiments and a tick mark to indicate Etx activity and a cross for when negligible effect of Etx on the system has been detected. Extent of Etx effect is indicated in colour (see bottom panel for key). RT stands for room temperature and MBB indicates work carried out solely by M. Bokori-Brown.

Mechanism:	Oligomerisation				Pore-formation			
System:	CHO-hMAL membrane		RBC membrane		CHO-hMAL cells	whole RBCs		DPhC bilayer
Experiment:	Membrane oligo. assay (RT)	Membrane oligo. assay **37C**	Membrane oligo. assay (RT)	Membrane oligo. assay **37C**	MBB cytotoxicity **37C**	Haemolysis assay (RT)	Haemolysis assay **37C**	Electro-physiology (RT)
Y42A	✖	✖	✓	✓	✓	✓	✓	✓
Y43A	✖	✓	✓	✓	✓ Y42A<Y43A< WT	✓	✓	✓
H162A	✓	✓	✓	✓	✖	✖	✓	✓
WT	✓	✓	✓	✓	✓	✓	✓	✓

✖	Negligible compared to WT
✓	10-40 %, compared to WT
✓	40-60% compared to WT
✓	60-70 %, compared to WT
✓	70-80 %, compared to WT
✓	No different to WT

3.3 Discussion

3.3.1 Radial absorbance profiles

The radial absorbance profiles (equation (2.1)) and the images of RBCs incubated with WT Etx show cells swelling and becoming more rounded, followed by a loss of haemoglobin, resulting in an empty ghost cell (Figure 3.1). Etx pores inner channels are reportedly only 24 Å in diameter [42] and allow molecules of up to 1 kDa in size to diffuse through [40]. As a single haemoglobin subunit is approximately 16 kDa, haemoglobin would not be able to leak through a pore, which suggests haemoglobin loss occurs due to a more significant disruption of the membrane. The Etx-induced swelling of cells before lysis is supported by previous work looking at MDCK cells [41]; however, this work additionally showed membrane blebbing which was not observed in this thesis. Blebbing of RBC membranes by another pore-forming toxin has been observed previously [104]. We suggest that, in future studies to catch such events in RBCs, the cells would have to be monitored using high magnification and high frame rate microscopy.

3.3.2 Y42A

We hypothesised that the amino acid, Y42, is required for binding to a receptor. Therefore, it was expected that Y42A binding, and therefore oligomerisation and haemolysis would be impaired. Indeed, Y42A did exhibit reduced binding, oligomerisation (Methods 2.2.3), and haemolysis in RBCs (Methods 2.2.5), compared to WT (Figure 3.5). Further, the binding, oligomerisation and lysis of CHO-hMAL cells by Y42A was extremely low (M. Bokori-Brown, to be published), indicating that this mutant is important in hMAL receptor binding, at least in CHO cells.

Further, Y42A activity appears to be concentration dependent. Very little haemolysis was seen at 1 µM compared to at 10 µM (Figure 3.2). This could be understood in terms of probability of binding, as the higher the number of molecules, the higher the likelihood of enough successful bindings to facilitate oligomerisation and therefore pore-formation. The Y42A mutation is in the receptor-binding region so, either hMAL-binding is impaired or, alternatively, binding through this mechanism is completely obliterated, and another binding mechanism is used. For example, Y42 may bind to a different isoform of MAL, a different receptor altogether, and/or purely bind in a hydrophobic manner in RBC membranes.

It is possible that Y42 is involved in binding to a different receptor altogether. A previous study found evidence towards possible glycan binding sites in the region of Y42 in the receptor-binding domain, although confirmation of this is inconclusive at this stage as it was not the focus of the study [45]. RBCs have trans-membrane glycoproteins called glycophorins, whereas CHO cells reportedly lack the enzyme to create similar glycoproteins [105]. Considering this information, the reduced activity by Y42A on RBCs, compared to WT, could be due to impaired glycan binding, where the same effect is not observed in CHO-hMAL cells because they lack the glycoprotein.

The impairment in binding, oligomerisation and haemolysis was seen at both room temperature and 37 °C. However, Y42A activity at each of these stages increased with temperature. Therefore, the temperature increase appears to compensate for the effect of the mutation in Y42; however, it does not repair it enough to match the WT activity. This could suggest that Y42A is defected in a way such that the interaction with a receptor protein would be unstable, leading to transient binding and unbinding. At higher temperatures, the likelihood of enough monomers being bound to the membrane at one time would be increased, resulting in increased receptor-binding activity.

Increased temperature can also cause molecules to change shape due to thermal expansion which can lead to amino acids that are otherwise hidden to become more exposed [106]. It is possible that this could happen with Etx, either exposing hydrophobic amino acids and therefore increasing hydrophobic binding efficiency, and/or exposing receptor-binding amino acids, which would enhance receptor-binding.

In addition, increased temperature would increase thermal fluctuations of the molecule, an effect which has been shown to increase receptor-binding even when the thermal fluctuation affects a distal part of the molecule [107]. Therefore, thermal fluctuations in the local environment, induced by the temperature increase, could explain increased receptor binding with temperature with Y42A.

These results do not answer whether Y42A is required for receptor binding in RBCs, but do provide evidence towards a complex interaction system where multiple binding mechanisms are used.

3.3.3 Y43A

The Y43 amino acid has been previously reported to be important in binding to the hMAL receptor, where a Y43E variant was not toxic to CHO-hMAL cells [35]. In addition, our group observed reduced binding, oligomerisation and lysis of CHO-hMAL cells by the Y43A variant (M. Bokori-Brown, to be published).

However, in RBCs we found the binding, oligomerisation and haemolysis by Y43A was no different to that seen of WT. Therefore, the Y43 amino acid is probably not important for receptor-binding in RBCs. From this finding, any putative MAL receptor on RBCs is therefore likely to be of a different form to the hMAL receptor used by previous studies (Rumah *et al.*, (2015) and M. Bokori-Brown), which is from human T-lymphocytes. Indeed a MAL isoform C has been reported to be present in RBCs [53], although this publication has yet to be peer-reviewed at the time of writing this thesis. This shows that there is variation in the important amino acids for receptor-binding, and this changes with different versions of receptor.

This indication that there is a MAL isoform, rather than the hMAL used in CHO-hMAL cells, points to the weak binding that we see with Y42A being an impaired interaction with MAL isoform C. However, other options still include: Y42A weakly binding to another receptor such as a glycophorin, or purely hydrophobic binding in RBCs by Y42A. Hydrophobic binding is possible due to a large number of uncharged hydrophobic amino acids in Etx, specifically in the receptor-binding domain (Figure 1.12).

3.3.4 H162A

H162A has previously been considered as a safe variant for receptor-binding studies at 37 °C [45]. Indeed, in our study, H162A caused negligible haemolysis at room temperature, even at the high concentration of 10 µM, despite significant binding and oligomerisation seen in RBC cell membranes. These results reflect previous findings of this mutation causing a block to the conformational change required to punch a hole in the membrane [45, 108]. However, the data in this thesis showed that H162A was able to cause haemolysis in RBCs at 37 °C, at a rate of 10-40 % compared to WT haemolysis, as well as form pores similar to WT in artificial lipid bilayers.

In contrast, oligomer formation in CHO-hMAL cells was not reduced compared to WT, despite inhibition of cytotoxicity at both room temperature and 37 °C. This suggests

that the RBC membrane uniquely does not inhibit the pore-formation, where other cell types would. This factor of RBCs would have to only be apparent at 37 °C.

There was no difference in the extent of oligomerisation seen in RBC membranes between room temperature and 37 °C experiments and therefore haemolysis at the higher temperature cannot be explained by improved binding or oligomerisation mechanisms. This suggests that, specifically the pore-formation step in RBC membranes is affected by temperature. However, we found that H162A was able to form pores in lipid bilayers at room temperature (Methods 2.2.6), indicating that it is not temperature that contributes this rescue effect, but the increase in thermal fluctuations that would come with using synthetic bilayers or by increasing temperature.

Supporting this hypothesis, DPhPC bilayers have been found to be less stiff, with a 30 % smaller bending modulus, than the more physiologically relevant, Dioleoyl phosphocholine (DOPC) bilayers [109], hence a DPhPC bilayer would undergo thermal fluctuations of higher amplitudes. This mechanism of thermal fluctuation-dependent activity appears specifically pronounced in RBCs.

When H162A was incubated at room temperature with the cells for 1 hour prior to the increase to 37 °C, the haemolysis still took approximately 30 minutes to appear, as it did when incubated at the increased temperature straight away (Figure 3.4). As oligomer formation is unaffected by temperature (Figure 3.8), there would have been unrestricted oligomerisation taking place during the one hour at room temperature, setting the stage for rapid haemolysis once the temperature increase enabled pore-formation. However, we still observed a 30-minute delay before detectable haemolysis, suggesting that the pore-formation mechanism was re-facilitated gradually – where the probability of sufficient thermal disturbance in the local environment occurring to overcome the mutation is low/would increase with time. In addition, there is no concentration dependence of H162A between 1 and 10 µM, which suggests that the maximum number of oligomers was accomplished during the room temperature incubation.

The restoration of pore-formation function seen in RBCs at 37 °C suggests that the RBC lipid environment is more conducive to the conformational change required for pore-formation due to possible increased thermal fluctuations in the areas of Etx

oligomerisation. Thermal fluctuation has previously been linked to pore-formation mechanisms whereby a similar mutation in the related protein, aerolysin, could be overcome by destabilisation in the local environment [108].

Aerolysin and aerolysin-like proteins have key hydrophobic amino acids with side chains of aromatic rings and hydrogen bond donors in the β-strands behind the pre-stem loop which appear to facilitate the release of the pre-stem loop and following β-strands [108]. Once released, the pre-stem loop heads the movement through a cavity between two neighbouring monomers, to form the inner tube of the double β-barrel [110].

In aerolysin, the release of the pre-stem loop is triggered by C-terminal peptide (CTP) removal [111]. More specifically, the CTP removal exposes a partially hydrophobic amino acid, tyrosine, which subsequently moves away from exposure and this movement facilitates the release of the pre-stem loop [110]. When tyrosine was replaced by glycine, no movement was triggered because, although glycine is also hydrophobic, it formed an interaction with a leucine from the neighbouring β-strand and this association appeared to prevent the movement that triggers pre-stem release [110].

The partially hydrophobic H162 amino acid is thought to be in an equivalent position to the leucine described in aerolysin [108]. It was mutated to a hydrophobic amino acid, alanine, in the H162A Etx variant. As this mutation is very similar to the tyrosine mutation in aerolysin, it could be that the effect of the H162A mutant is also blockage of the pre-stem. With higher thermal fluctuations, the blocking of the pre-stem loop by the H162A mutation may be overcome, allowing it to unfold to a position ready to form the β-barrel.

3.3.4.i H162A binding and oligomerisation

A separate mechanism appears to contribute to reduced oligomerisation seen with H162A and RBCs compared to WT (Figure 3.8). The reduced haemolysis compared to WT of RBCs at 37 °C is within the same scale as the reduced oligomerisation in comparison to WT. Unfortunately, the scale of reduced binding has not been quantified; however, it is reasonable to assume that reduction in oligomerisation is a result of reduced binding and that the most likely cause of reduced haemolysis compared to WT is reduced binding. However, the cause of reduced binding of the

H162A mutant is unclear. One suggestion could be that the mutation causes a conformational change that impairs protein ability to access the hydrophobic region of the RBC.

There was no reduction in binding and oligomerisation seen with CHO-hMAL cells (M. Bokori-Brown, to be published) which may be because the prevalent binding mechanism for these cells is via a receptor, and not through hydrophobic interaction.

3.3.5 All variants cause pores of similar conductance in lipid bilayers

Each variant was able to form a pore in DPhPC lipid bilayers (Methods 2.2.6) which is in contrast to the complex variation observed so far in physiological cells. Cells have many other structures on their membranes, such as the glycocalyx that would inhibit access to a protein. With most Etx-susceptible cells, a receptor is likely needed to overcome any barriers to binding. In addition, the heterogeneity of lipid species in the outer (and inner) leaflets of the physiological cell membranes would affect diffusion times for the monomers and therefore oligomerisation time scales.

3.4 Conclusions

On the basis of these data, we speculate that Etx action on RBCs may be partly receptor-mediated and that this receptor associates with the Etx Y42 amino acid. It is possible that there is both hydrophobic-mediated and receptor-mediated interactions between Etx and the cell membrane. This hypothesis could explain the reduced activity seen with the Y42A variant, where mutation to the Y42 amino acid prevents binding with a receptor but not hydrophobic-mediated binding (which may even be enhanced, as evident in experiments at 37 ^{o}C). Whereas the WT and Y43A Etx variants may simultaneously employ both binding routes, and therefore have a more severe and rapid cytotoxic affect.

In comparing our data alongside findings on CHO-hMAL cells by our collaborator M. Bokori-Brown, we find that the amino acids important for Etx activity differ between cell types. This could be due to a hydrophobic interaction in RBCs and not CHO cells, likely due to increased obstructions to lipids in CHO cells, or involvement of a different receptor.

Potential receptors in RBCs could be a MAL isoform or glycophorins. The hMAL receptor found in T-lymphocytes does not appear to be present in RBCs, according to

our data, where the Y43 amino acid (shown to be required for hMAL-binding) was mutated, but resulted in no impairment to binding, oligomerisation, pore-formation or haemolysis in these studies.

We have hypothesised that H162A toxicity in RBCs can be reactivated due to thermal fluctuations in the membrane which occur at physiological temperature. Specifically, we hypothesise that the mutation causes an unstable 'block' to the conformational change required for pore-formation, as a similar mutation in aerolysin displayed similar instability.

4 Effect of chitosan on lipid monolayers – Langmuir trough experiments

4.1 Introduction

This chapter continues the examination of membrane-active, biological substances by investigating the effect of a polysaccharide, chitosan, on lipid monolayers. The aim was to investigate whether chitosan could bind to or integrate into lipid monolayers and whether this would cause changes to the physical properties of the monolayer. The focus of this chapter is on the lipid monolayer viscoelasticity, in particular the static and dynamic dilatational elastic moduli, and their response to chitosan.

Improved understanding of chitosan-membrane interactions is important not only because chitosan is produced by the disease-causing pathogen *E. histolytica*, but because it is increasingly applied in multiple biomedical advancements, spanning prophylactics, disease treatments, and commercial dietary supplements.

Lipid mixtures that model inner and outer cell membrane leaflets (IL, and OL, respectively) were used to form monolayers on a subphase in a Langmuir trough. The specific lipid mixtures were used because they are representative of mammalian cell membranes (in terms of headgroup composition) and the Petrov laboratory has previously established an understanding of their behaviour.

The aims of the study presented in this chapter are:

1. To characterise chitosan-induced viscoelastic changes in lipid monolayers that represent mammalian cells.

2. To investigate whether the initial surface pressure of a monolayer affects adsorption of chitosan.

3. To compare the static (ε) and dynamic (E_{IM}, E_R) dilatational elastic moduli of lipid monolayers.

Compression isotherms and a dynamic dilatational measurement (at a target surface pressure) were conducted on the pure lipid monolayer before each experiment. The pure lipid monolayer was then compressed to the target surface pressure and chitosan injected underneath the monolayer. Approximately one hour after chitosan insertion,

a further dynamic dilatational measurement was taken, followed by a compression isotherm to finish.

4.2 Results

4.2.1 Isotherms

The compression isotherms changed after chitosan addition under the monolayer, where the surface pressure consistently took off at a larger area, compared to the pure monolayer (Figure 4.1). This effect is seen with both IL and OL monolayers (Figure 4.1A, B). This effect was consistently more prominent with the IL.
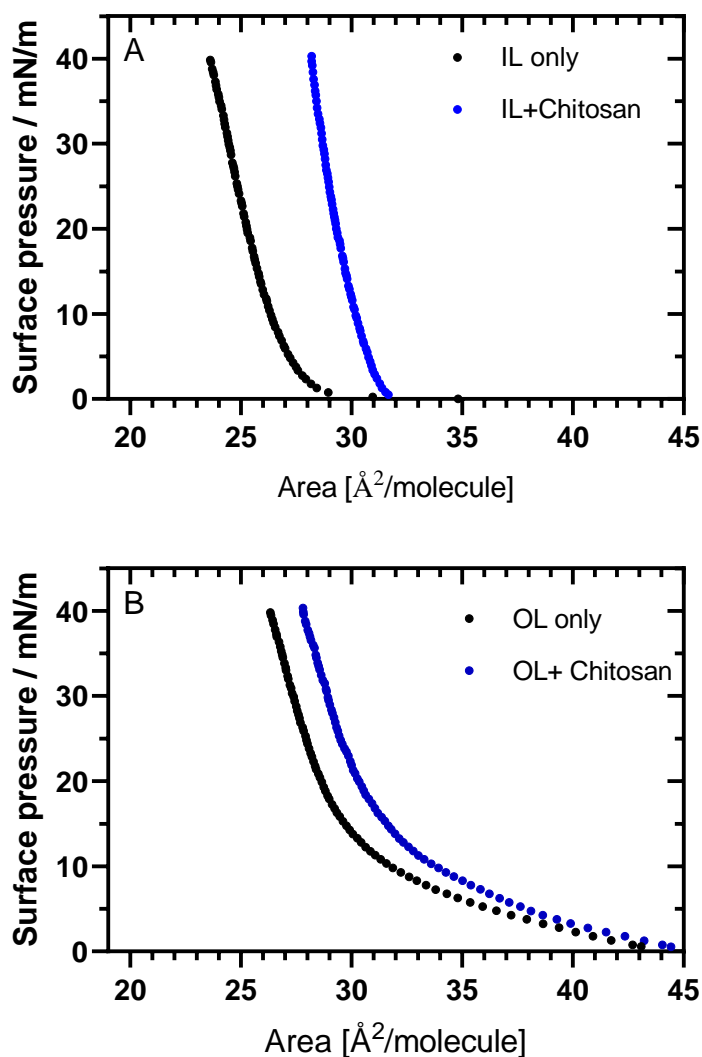
Figure 4.1 Pressure-area isotherms before (black) and after (blue) chitosan addition to IL monolayers (A), and OL monolayers (B).

4.2.2 Static dilatational elastic modulus

The compression isotherms were then used to calculate monolayer static dilatational modulus, ε. Representative static dilatational moduli can be seen in (Figure 4.2) where chitosan adsorption to the IL led to a consistently higher elastic modulus. However, no significant change in elastic modulus was observed in the OL with chitosan (Figure 4.2).
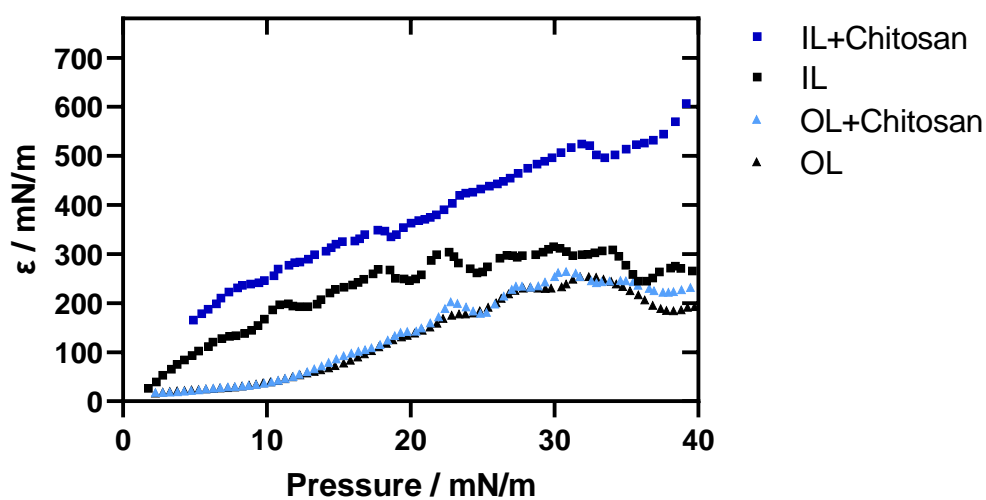
Figure 4.2 Static dilatational elastic moduli of monolayers before and after chitosan addition to the subphase.

The mean of three and four experiments on IL and OL monolayers, respectively, at selected pressures is presented below (Figure 4.3). Statistical significance is seen with the IL at all pressures (Figure 4.3A) Error bars of pre- and post- chitosan treated monolayers overlap at all pressures with the OL (Figure 4.3B).
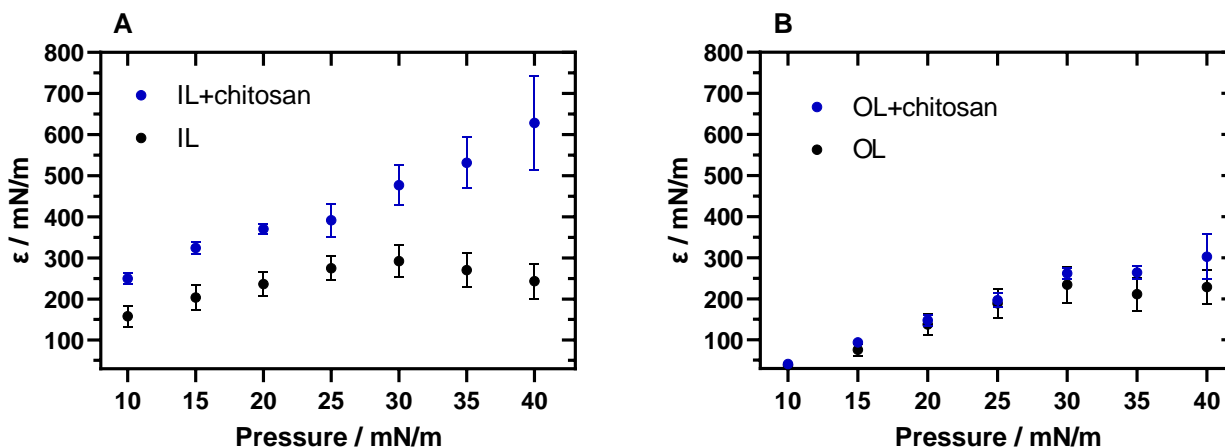
Figure 4.3 The mean static dilatational elastic moduli at seven surface pressures of A) IL and B) OL lipid monolayers. Means and standard error bars obtained from three and four experiments, respectively.

4.2.3 Dynamic dilatational elastic moduli

The dynamic dilatational elastic moduli can be measured when a quick compression causes the surface pressure to increase and then gradually decrease at constant surface area as the systems try to reach equilibrium again. An example of a sudden compression is shown in Figure 4.4 where the compression occurs at approximately 23 minutes and a relaxation of surface pressure begins straight afterwards, while the surface area is kept constant. This relaxation transient is used to calculate the dynamic dilatational elastic modulus of the monolayer at the initial surface pressure (19 mN/m in Figure 4.4).
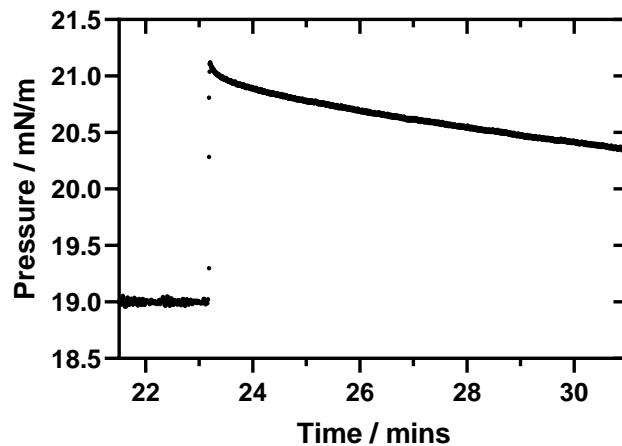
Figure 4.4 Example of small area change causing increase in pressure and the resulting relaxation curve.

The curve produced by recording the relaxation of surface pressure over time was fitted using equation (2.6) to extract values of the pre-exponential factors and the relaxation times of each process of relaxation. Fitted relaxation curves of IL and OL monolayers with and without chitosan are shown below (Figure 4.5) and the parameters of each curve are reported in (Table 4.1).
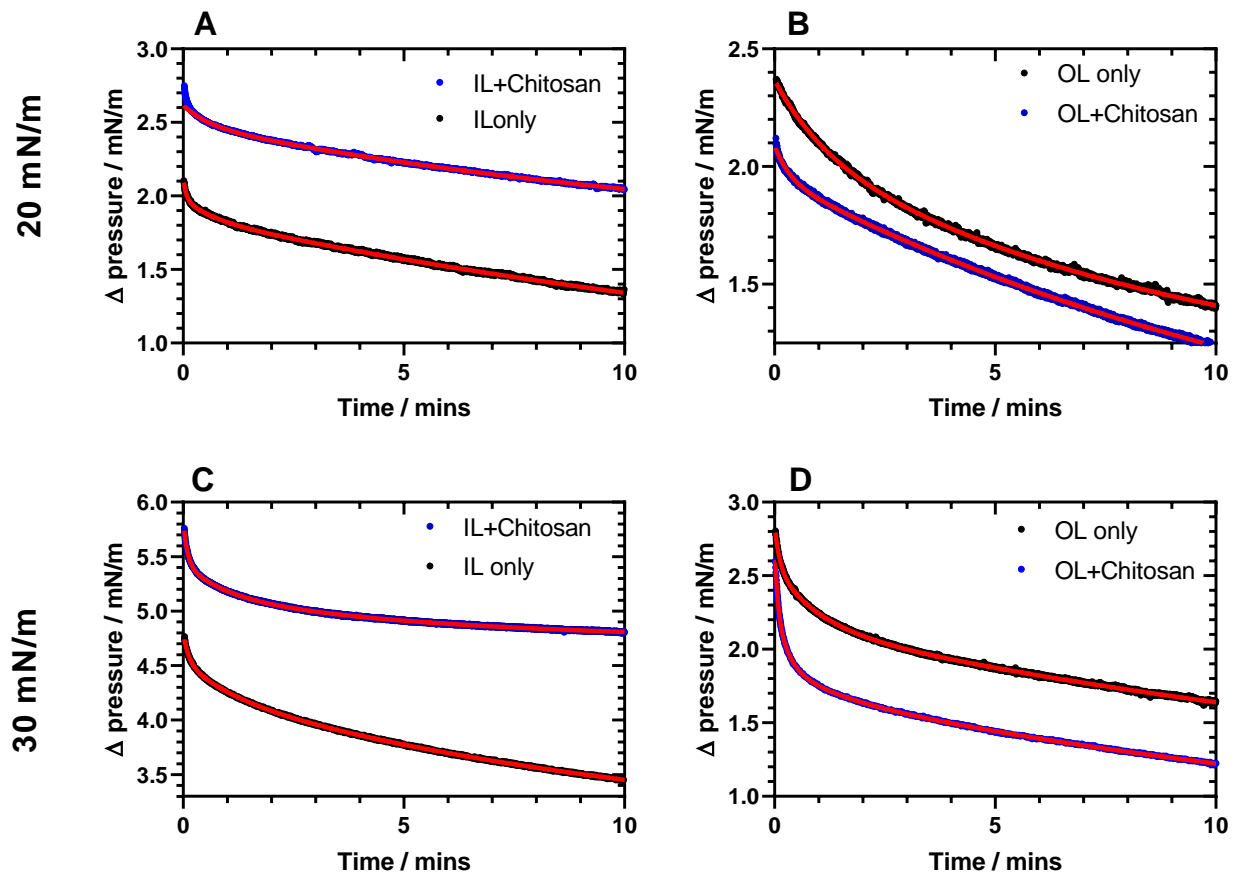
Figure 4.5 Surface pressure relaxation transients of IL (A and C) and OL (B and D) monolayers with and without chitosan added. Top graphs show monolayers where initial surface pressure was approximately 20 mN/m (A and B) and bottom graphs show monolayers of initial pressure of 30 mN/m (C and D). Red line shows the fit of the experimental data with parameters shown in Table 4.1.

Chitosan addition to the IL at 20 mN/m caused the slowest relaxation process, τ_1, to become faster and the pre-exponential factor, A_1, to decrease, whereas the opposite can be seen with the OL at 20 mN/m where τ_1 becomes slower and A_1 increases (Table 4.1). However, the same trend was not seen at a higher surface pressure, as τ_1 became faster (and A_1 decreased) for both the IL and OL at 30 mN/m (Table 4.1).

Table 4.1 Relaxation transient parameters (see equation (2.6)).

	π_0 (mN/m)	A_1	A_2	A_3	A_4	τ_1 (s)	τ_2	τ_3	τ_4	$\Delta\pi\infty$ (mN/m)
IL	20	1.35	0.12	0.14	--	1241.50	37.57	3.85	--	0.51
	30	1.42	0.29	0.26	--	713.20	64.20	7.16	--	2.84
IL + chitosan	20	0.85	0.13	0.19	--	823.57	34.14	0.40	--	1.64
	30	0.42	0.28	0.39	--	337.20	53.12	5.44	--	4.74
OL	20	1.03	0.28	--	--	550.32	68.98	--	--	1.07
	30	1.37	0.39	0.28	--	1236.00	58.14	7.15	--	0.79
OL + chitosan	20	1.40	0.14	--	--	835.93	20.35	--	--	0.55
	30	1.17	0.20	0.42	0.42	1057.00	65.71	14.47	3.37	0.56

A Fourier transform was performed on the relaxation data fit which produced a complex modulus, equation (2.7), corresponding to the elastic (storage (E')) and viscous (loss (E'')) processes involved in the monolayer relaxation. In all monolayers (with or without chitosan) the storage modulus curved upwards to a plateau at higher frequencies (which is expected because high frequency signals would be due to highly elastic, stiff, components), whereas the loss modulus exhibited at least one peak, earlier on the frequency scale.

The frequency range used was 10^{-4} to $10^{0.6}$ /s which represents time scales as large as 10 000 seconds (2.7 hours) and as small as 0.25 seconds. The latter timescale is equal to the sampling rate in these experiments, however, the larger time scale is several times larger than the length of these experiments. The reason this frequency range was used was because they are based on the work by Georgi As. Georgiev [94, 112] who reasoned that even short experiments can observe part of a relaxation process which has a time scale of 10 000 seconds. The fitting process of the relaxation transients (methods section 2.3.8.ii and results Figure 4.5) were largely exact and therefore, these long time-scale processes can be reasonably estimated.

Plotting loss against storage moduli to make a Cole-Cole plot allows clearer visualisation of the number of processes affecting the relaxation, according to the number of peaks [96]. Most experiments resulted in one clear peak with a small shoulder at higher storage moduli values. Often, especially at higher surface pressures, a second peak is seen at higher storage moduli which becomes more prominent with the addition of chitosan.

4.2.3.i   Inner leaflet only

The IL loss modulus (corresponding to soft, easily deformable domains within the IL, such as weak bonds between certain molecules), at 23 mN/m, had a maximum value of 57 mN/m at a frequency of approximately 10^{-4} /s and at 28 mN/m this increased to 65 mN/m (Figure 4.6). Additionally, the storage modulus (corresponding to stiff, difficult to deform components of the IL, such as strong bonds between molecules) increased from 312 mN/m (at 23 mN/m) to 368 mN/m (at 28 mN/m) at its plateau value. The ratio of loss to storage moduli, tan φ, at both monolayer pressures was below 0.3 over the entire frequency range. Any value of tan φ below one shows that the monolayer is predominantly elastic.

The Cole-Cole plots (see the last two plots in Figure 4.6) can be interpreted within the standard linear Maxwell solid model for viscoelasticity (Figure 2.8) which demonstrates that the number of peaks in the Cole-Cole plots indicate the number of systems, each with a viscous and elastic contribution, involved in the monolayer relaxations.

The Cole-Cole plot of the IL at both 23 mN/m and 28 mN/m show that the monolayer behaviour is dominated by one significant Maxwell process. There is a hint of a second component in the plots at high values of the storage modulus (at approximately 300 mN/m and 350 mN/m for the lower and higher surface pressure monolayers, respectively). These viscoelastic characteristics of the lipid monolayer will be used as a reference for comparison when chitosan is introduced.

4.2.3.ii   Inner leaflet with chitosan

The viscoelastic behaviour of the IL monolayer is significantly modified upon introduction of chitosan. There was a large drop in loss modulus, indicating a reduction in viscosity with chitosan addition to the IL at 23 mN/m, with the peak shifting slightly to the right on the frequency scale, compared to the pure monolayer. A chitosan-induced reduction of viscosity was also seen at 28 mN/m, where two peaks can be

observed: the first peak at a low frequency of 10^{-4} /s and the second peak, similar to that of the lower pressure, is shifted slightly to the right of the IL-only peak on the frequency scale. The appearance of a second peak indicates the presence of an additional relaxation process that should be identifiable in the corresponding Cole-Cole plots.

Chitosan caused the IL monolayer to become stiffer, as the measured storage modulus was higher over the entire frequency range, for both 23 mN/m (although the storage modulus plateau value was only slightly larger) and 28 mN/m. The ratio, tan φ, clearly decreased when chitosan was added at both pressures, showing an even greater significance of the storage component.

The Cole-Cole plot of the monolayer at 23 mN/m shows one main Maxwell process again with the addition of chitosan. The peak in this case is much smaller compared to the pure lipid monolayer, and has a much smaller range, situated high on the storage modulus axis (between 250-325 mN/m). The Cole-Cole plot at 28 mN/m shows at least two Maxwell processes (and a possible third one at higher values of the storage modulus), with both peaks situated lower than IL-only on the loss modulus scale and higher on the storage modulus scale. This indicates the presence of at least two relaxation mechanisms which are predominantly elastic.
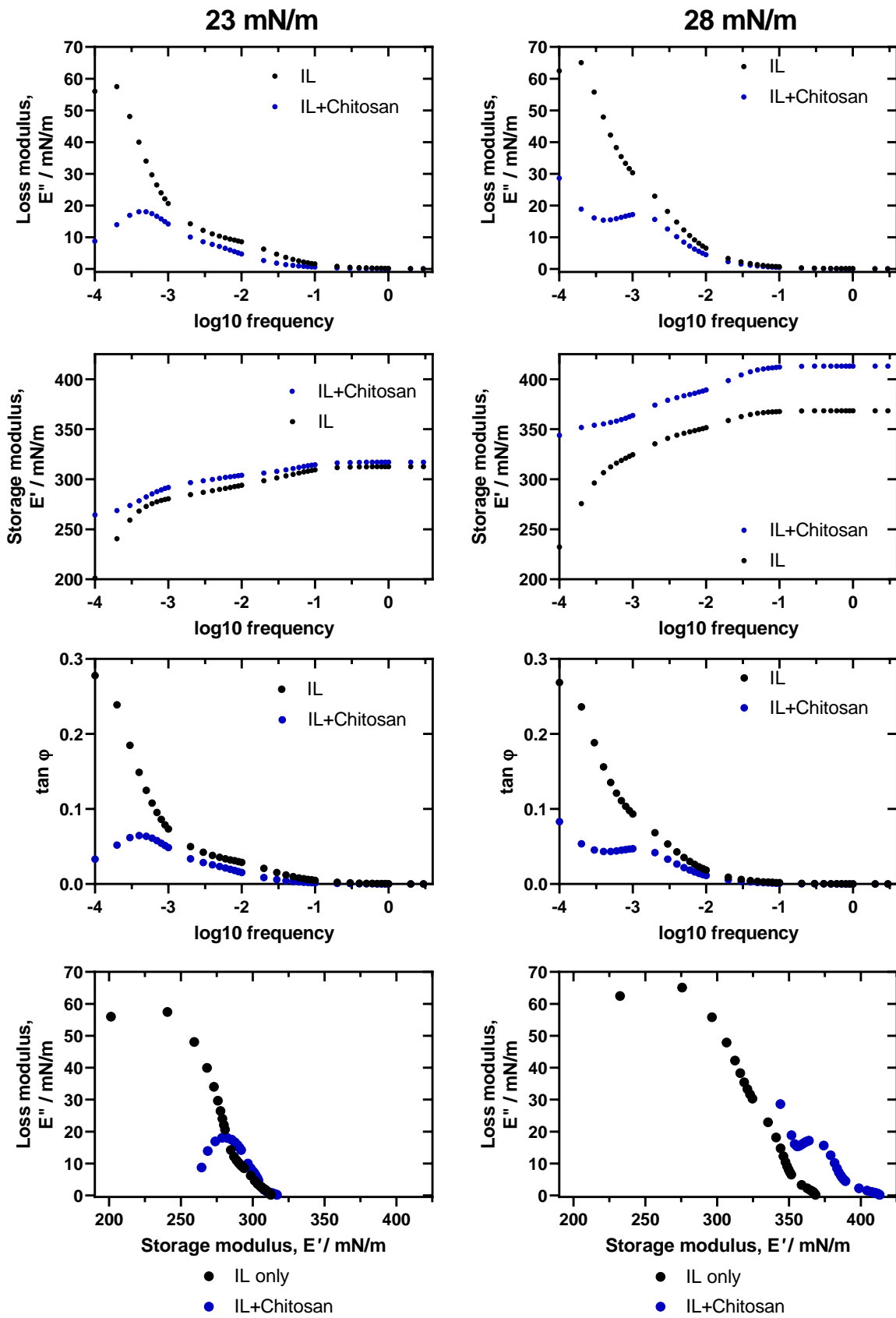
Figure 4.6 Comparison of storage and loss moduli of IL monolayers with and without chitosan.

4.2.3.iii Outer leaflet only

The OL loss modulus peaked between the frequencies of 10^{-4} /s and 10^{-3} /s for both 19 and 28 mN/m (Figure 4.7). At 28 mN/m the loss modulus maximum increases slightly, showing that OL becomes more viscous with pressure. At this higher pressure there is also a small shoulder at an approximate frequency of $10^{-2.5}$ /s, indicating two processes involved in the viscous component.

The OL storage modulus maximum is slightly higher at 28 mN/m compared to 19 mN/m suggestive of a slightly stiffer monolayer at the higher pressure. The tan φ values for the OL monolayers were smaller than one for both surface pressures, showing a predominantly elastic component to the monolayers, and the maximum tan φ value increased by approximately 0.2 at the higher pressure, showing that the OL becomes more viscous. There is also a small tan φ shoulder seen at approximately 10^{-3} /s with the OL at 28 mN/m.

The Cole-Cole plots show that at 19 mN/m the OL monolayer behaviour is dominated by one significant Maxwell process contributing to its viscoelasticity, whereas at least two (and probably a third one) can be seen at 28 mN/m with two shoulders higher on the storage modulus axis. The Cole-Cole peak at the higher pressure is higher on the loss modulus axis and spans a larger range on the storage modulus axis.

4.2.3.iv Outer leaflet with chitosan

The introduction of chitosan modifies the viscoelastic behaviour of the OL monolayer in a different way to the IL monolayer. The opposite to the IL was seen with the OL at 19 mN/m, where the loss modulus increased with chitosan addition, indicating an increase in viscosity (Figure 4.7). An increase in the first loss modulus peak can be seen for the OL monolayer at 28 mN/m with chitosan, and the second peak at a higher frequency clearly shows an increase in viscosity.

The storage modulus plateaued at a slightly lower value when the chitosan was added to the OL monolayer at 19 mN/m indicating a decrease in stiffness. The storage modulus of the OL, at 28 mN/m, was largely unchanged by chitosan at lower frequencies (up to about 10^{-2} /s) and then plateaued at a higher value at higher frequencies (in contrast to that seen at 19 mN/m), indicating an increase in stiffness (Figure 4.7).

The ratio, tan φ, remains less than one for both OL only and OL with chitosan, showing a predominantly elastic system. However, there is clearly an increase in tan φ with chitosan added at 19 mN/m up to frequencies of 10^{-3} /s. At 28 mN/m, the second tan φ peak becomes more pronounced with chitosan.

All this resulted in modifications in the Cole-Cole plots. The Cole-Cole plot of the OL at 19 mN/m is larger on the loss modulus axis with the addition of chitosan, and the whole curve shifts down on the storage modulus axis. Interestingly, the introduction of chitosan did not significantly change the character of the plot, which remained dominated by one Maxwell process with a hint of a second, minor one, at larger values of the storage modulus. The Cole-Cole plot for 28 mN/m shows two peaks again (with a possible third process for large values of the storage modulus), however, the second peak (low on the loss modulus scale and high on the storage modulus scale) was larger with the addition of chitosan.
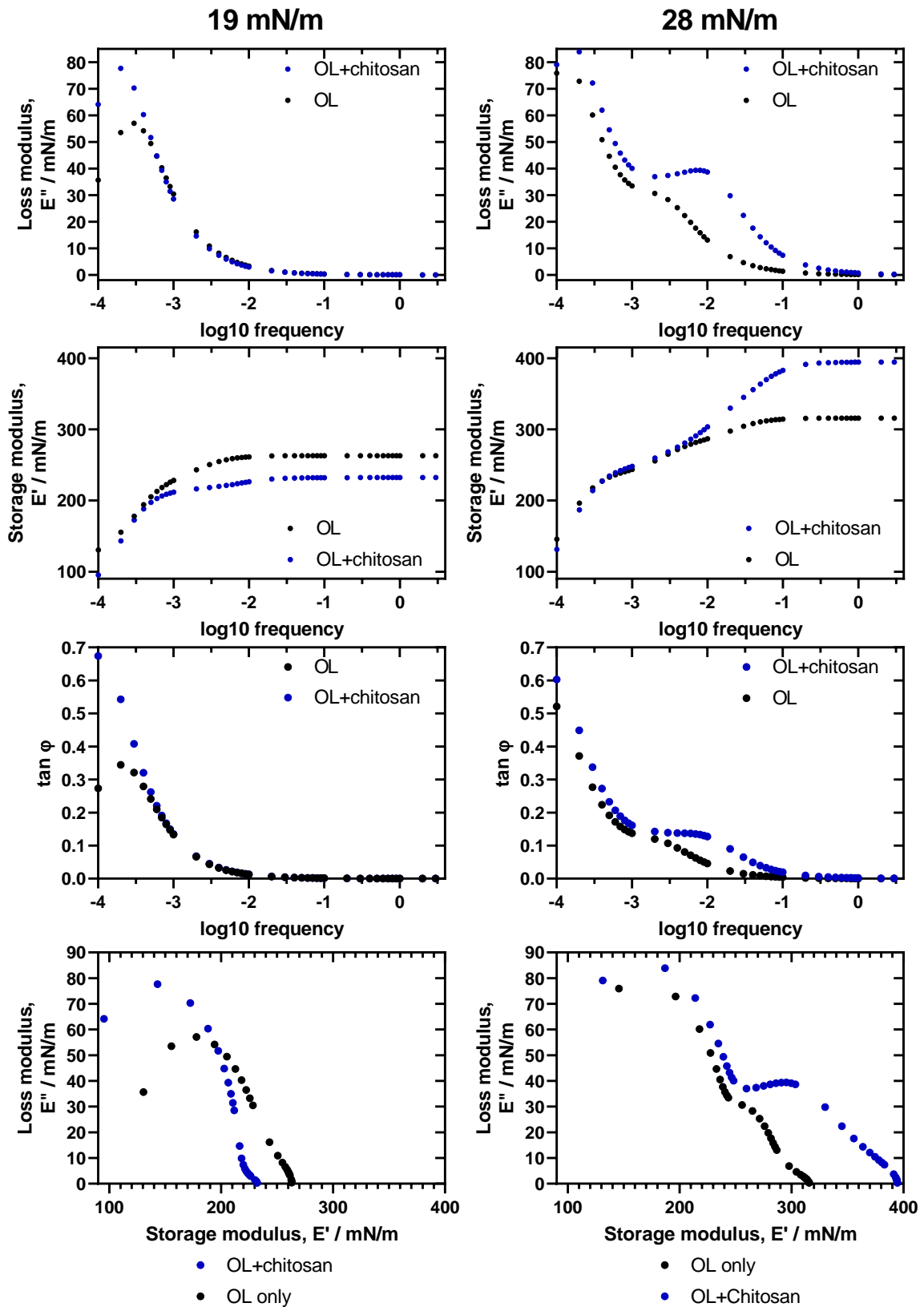
Figure 4.7 A representative comparison of storage and loss moduli of OL monolayers with and without chitosan.

4.2.4 Quantitative comparison of static and dynamic dilatational elastic moduli

The static and dynamic dilatational elastic moduli obtained over different pressures of the IL and OL were compared in Figure 4.8. The value of storage modulus used was the plateau reached at high frequency.

The IL-only dynamic elastic moduli were similar to the static elastic moduli, especially between pressures 15 and 25 mN/m (Figure 4.8A). The two dynamic measurements taken at approximately 30 mN/m were both higher than all the static dilatational elastic moduli measurements for the IL monolayer. With the addition of chitosan, the dynamic dilatational elastic moduli tend to be lower than that of the static elastic moduli, especially between pressures 20 and 29 mN/m (Figure 4.8B).

The OL dynamic dilatational elastic moduli values were considerably higher than the static moduli for all the pressures tested (between 12 and 35 mN/m) for both OL only and OL with chitosan, though both moduli follow similar trends of increased stiffness with pressure.
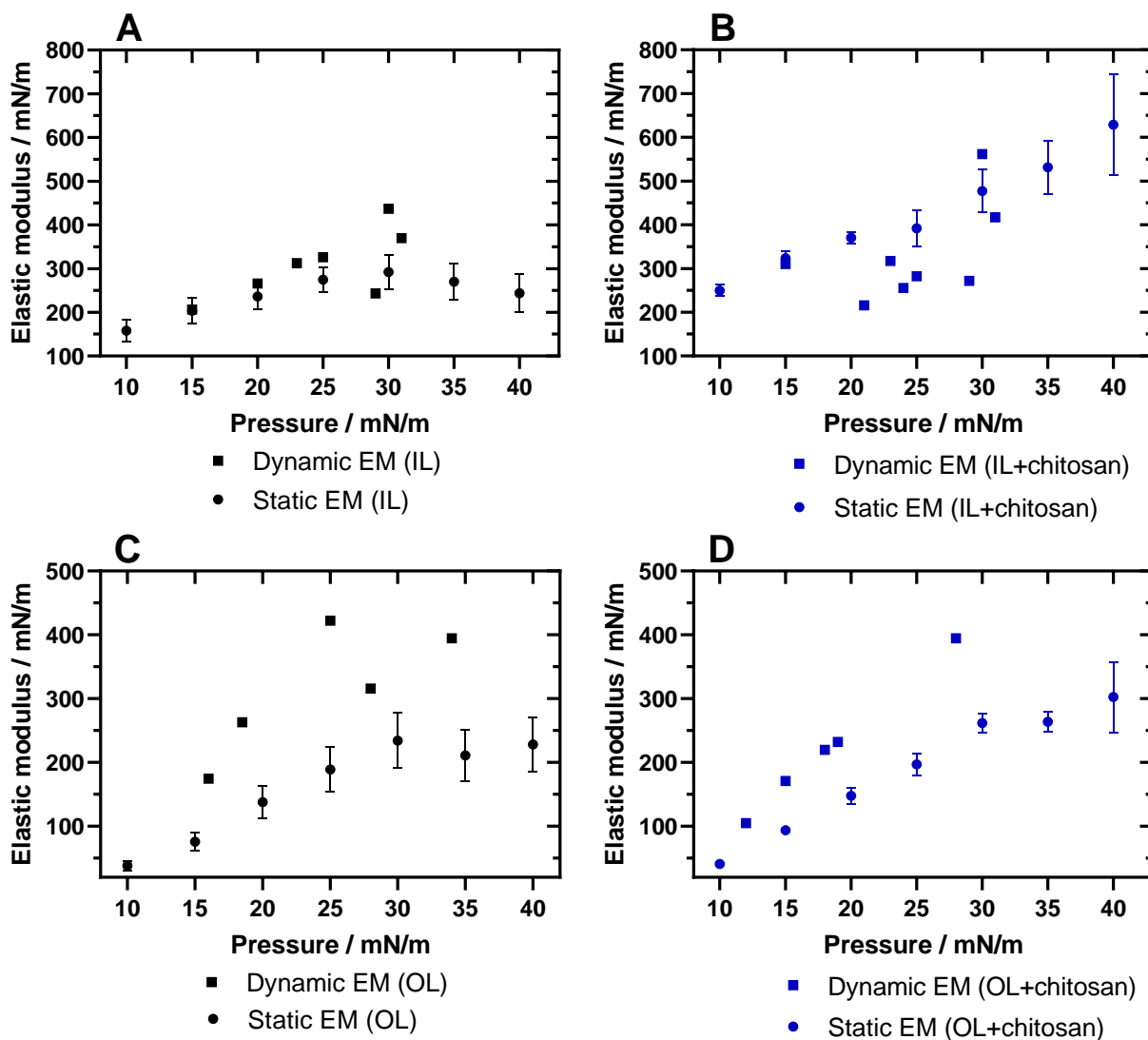
Figure 4.8 Comparison of the static dilatational elastic moduli (circles) and dynamic dilatational elastic moduli (squares) of OL and IL lipid monolayers.

4.2.5 Chitosan adsorption causes pressure increase

The surface pressure of the IL monolayer often increased when chitosan was injected under the monolayer. One example can be seen in Figure 4.9 where chitosan was added at time 0, where the initial pressure was 35.4 mN/m.
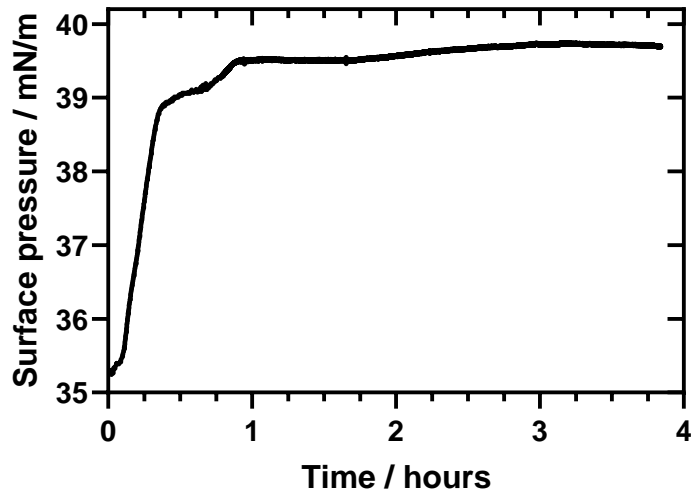
Figure 4.9 An example of the surface pressure increase after chitosan injection into the subphase (at time 0 hours).

The initial surface pressure may have some influence on the extent of the surface pressure change when chitosan is added. The majority of experiments recorded a maximum pressure, post-chitosan addition, of up to a 4.5 mN/m increase, for both IL and OL monolayers (Figure 4.10). On five occasions, between the initial pressures of the 23 and 35 mN/m, the IL surface pressure increased between 3.4 and 4.6 mN/m post-chitosan injection.

Inner leaflet pressure change with chitosan   **Outer leaflet pressure change with chitosan**
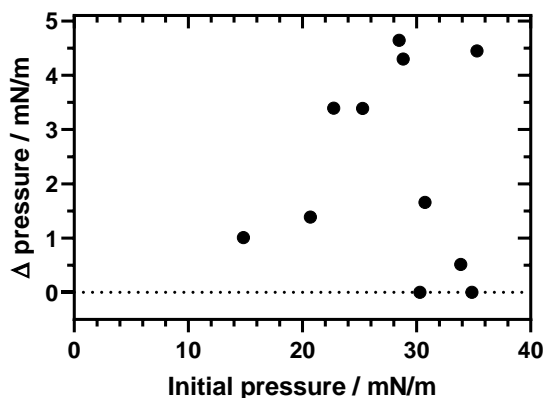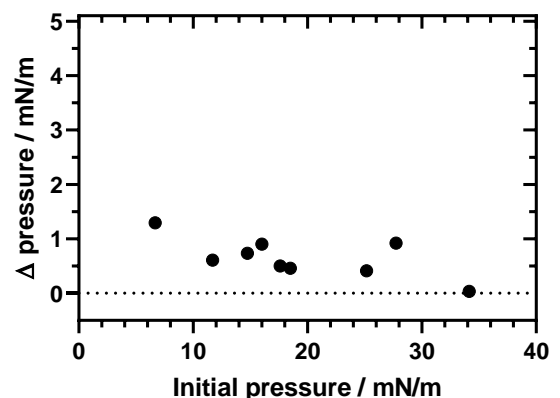
Figure 4.10 Maximum surface pressure changes after chitosan injection under monolayers of increasing initial surface pressures.

4.3 Discussion

4.3.1 Monolayer expansion

The compression isotherms shifted to the right after chitosan addition, where the pressure lift off began at a larger area/molecule (Figure 4.1). This indicates chitosan-induced expansion of the monolayer. In agreement with this, previous studies have found that chitosan causes expansion of lipid monolayers [66], especially saturated lipids [65] (lipids used in this thesis were saturated).

It has also been found that chitosan causes cholesterol monolayers to expand, likely due to hydrogen bonding between the amine groups of chitosan and the OH groups of cholesterol [69]. IL and OL have a negligible difference in cholesterol (IL only has 0.4 % less than OL) and therefore this effect would not account for the differences seen between our monolayer types.

The IL expansion was observed to be considerably more than that of OL and the surface pressure increased with chitosan addition to the IL monolayers (Figure 4.9) which also indicates a monolayer expansion. Expansion is most likely to be caused by insertion of chitosan between the lipids, and possibly penetrating into the acyl chain region. Chitosan molecules are clearly closely associating with the IL lipids, enough to modify the monolayer viscoelastic properties.

4.3.2 IL increase in elastic modulus with chitosan

In comparison to the OL, chitosan caused more of an impact on the IL monolayer where it increased the elastic modulus (thus increasing stiffness), as shown with both static and dynamic elastic measurement methods. In addition, the ratio, tan φ, clearly decreased when chitosan was added to the IL, emphasizing a decrease in viscous contributions in the monolayer.

There was a clear second peak with IL with chitosan on the tan φ plot and on the Cole-Cole plot, where it emerges low on the loss modulus scale and high on the storage modulus scale. The standard linear Maxwell solid model demonstrates that the number of peaks in the Cole-Cole plots indicate the number of systems, each with a viscous and elastic contribution, involved in the monolayer relaxations. An additional peak with the presence of chitosan indicates that chitosan adds another complex relaxation mechanism, with both viscous and elastic effects.

4.3.3 OL decrease in elastic modulus with chitosan

The opposite to the IL was seen with generally a lower elastic modulus with OL with chitosan. The static dilatational elastic modulus did not appear to change with chitosan addition to the OL. There was no clear evidence of increased dynamic dilatational elastic moduli by chitosan in the OL. However, in Figure 4.7, a marked increase in loss modulus is seen for the lower surface pressure of OL with chitosan. This indicates a viscous influence of chitosan, possibly because of association near headgroups causing friction between them.

The Cole-Cole plots of both the IL and OL monolayers with chitosan at 28 mN/m show a larger second peak low on the loss modulus scale and high on the storage modulus scale. This indicates the added mechanism of relaxation brought about by chitosan addition has a higher elastic component than the systems in place in the pure lipid monolayer.

4.3.4 Effects of dominant lipid species

Differences between the monolayers can be explained by their lipid compositions. The main difference between the IL and OL is the dominant lipid species, with high amounts of DPPS and DPPE in the IL and high amounts of DPPC and SM in the OL. The differences in chitosan impact between the two monolayer types can be explained in terms of electrostatic, hydrophobic, and hydrogen-bonding interactions.

4.3.4.i DPPS and DPPE

The headgroup of DPPS carries a net negative charge which would electrostatically attract chitosan which carries a net positive charge. Specifically, the amine group of chitosan will make a complex with the carboxyl group of DPPS. In agreement with this explanation, the electrostatic attraction between chitosan and the negatively charged lipid species, DPPG, has been previously documented and reported as the main cause of chitosan induced changes to the monolayer [70, 71].

Strong electrostatic interaction could cause increased stiffness of the monolayer due to the high molecular weight (50 – 190 kDa) of the chitosan polymer, spanning across several lipids and reducing lipid diffusion and increasing resistance to deformation.

DPPE is also present in a high percentage in the IL. DPPE have conical shapes, where the tails take up more space than the heads, therefore there could be more space between headgroups for the chitosan to access the hydrophobic regions of the acyl

106

chains. The monomers of chitosan that evade the deacetylation process remain in the form of insoluble chitin, with an $NHCOCH_3$ group on carbon 2 (rather than an amine group) (Figure 1.13). The chitosan used in our experiments was 75-85 % deacetylated and therefore will contain some hydrophobic moieties. Therefore, some hydrophobic interaction in the acyl chain region of the lipids will occur.

DPPE headgroups have an amine group which is a strong hydrogen bond donor which can form inter- and intra-molecular hydrogen bonds with phosphate and carbonyl groups of lipid headgroups [113]. At higher monolayer surface pressure, PE headgroups associate less with neighbouring lipids and more with the aqueous subphase, becoming more available for hydrogen bonding to solutes as demonstrated in Figure 4.11 [114]. The hydroxyl groups of chitosan may then competitively form hydrogen bonds with PE, causing further stiffening of the monolayer.
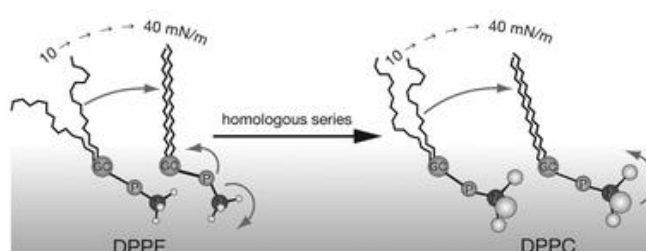
Figure 4.11 The effect of monolayer surface pressure on the depth of amine groups in the subphase [114].

There appears to be a pattern of chitosan adsorption to the IL being higher at pressures 20-30 mN/m (Figure 4.10). These surface pressures represent an area of lipid phase change and insertions often occur at phase change boundaries because domain formation changes can cause a break in line tension [115]. In addition, the presence of a maximum is suggestive of two mechanisms at play and could be the result of increasing hydrogen bonding, combined with decreasing access for hydrophobic interaction with increasing surface pressure.

4.3.4.ii DPPC and SM

The OL changes can be described in terms of the interaction between chitosan and DPPC and SM. These lipid species both have a choline base $(CH_3)_3N^+(CH_2)_2OH)$ esterified to the phosphate. The OH group at position 6 in the chitosan carbon chain

could form hydrogen bonds with the choline groups of PC and SM. However, these choline groups may be less available for hydrogen bonding with solutes than the amine group of DPPE [114] (Figure 4.11).

Both lipids carry a net neutral charge and therefore the strong electrostatic attraction seen with DPPS would not occur here, which could explain why the effects are generally smaller in the OL in comparison to the IL. In agreement with this, experimental data have shown just a slight interaction of chitosan with DPPC monolayers in comparison to negatively charged DPPG monolayers [68]. There would still be some electrostatic attraction to the negatively charged phosphate groups, however, facilitating some surface activity of chitosan.

A study demonstrated that a reduction in elasticity of DPPC and DPPG monolayers by chitosan is not solely by electrostatic interaction with the positively charged amine groups ($-NH_3^+$) of chitosan, because another molecule with similarly charged amine groups did not reduce static elasticity as much as chitosan [116]. Instead, the authors suggest interaction depends strongly on hydrophobic mechanisms, as speculated in this thesis, and/or the conformation of chitosan. The latter hypothesis being that coiled molecules of chitosan would insert more easily into the monolayer than non-coiled polymers, although they did not elaborate on a putative mechanism behind this.

Both DPPC and SM lipids are cylindrical shaped, where the tails and heads have the same width [6, 10] and therefore these lipids would pack well together. The reduced expansion of OL monolayers with chitosan could be due to a lack of gaps between lipid headgroups to allow for the hydrophobic interaction to occur at the acyl chain region, limiting adsorption of chitosan via hydrophobic interaction.

4.4 Summary

In summary, three mechanisms behind chitosan interaction with our lipid monolayers have been used to explain the differences seen between the IL and the OL monolayers. All three mechanisms (A: hydrophobic, B: hydrogen bonding, and C: electrostatic) are possible in both monolayer types but are much more prominent in the IL compared to the OL. Figure 4.12A shows a high amount of hydrophobic interaction in the IL at low surface pressure, due to spaces between lipid headgroups. Figure 4.12B shows a high amount of hydrogen bonds between PE headgroups and

chitosan, at high surface pressure. Figure 4.12C shows strong electrostatic interaction regardless of surface pressure in the IL between PS headgroups and chitosan.
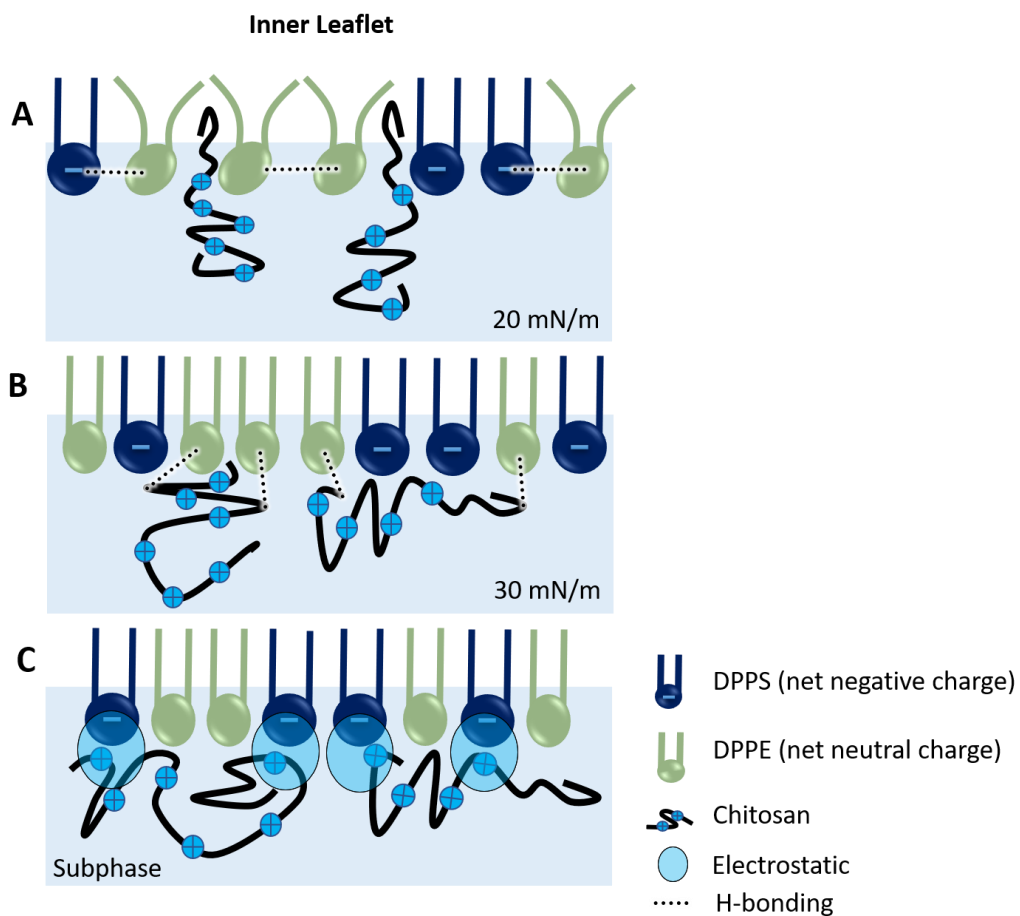
Figure 4.12 Chitosan interaction with IL monolayers by A) hydrophobic, B) H-bonding and C) electrostatic attraction.

Figure 4.13 shows that these three mechanisms may occur in the OL between chitosan and DPPC and SM lipids but are less likely due to less gaps for hydrophobic access, and less hydrogen bond donors available in the subphase, and any electrostatic attraction would be much weaker because of the net neutral charge of the DPPC and SM lipids.
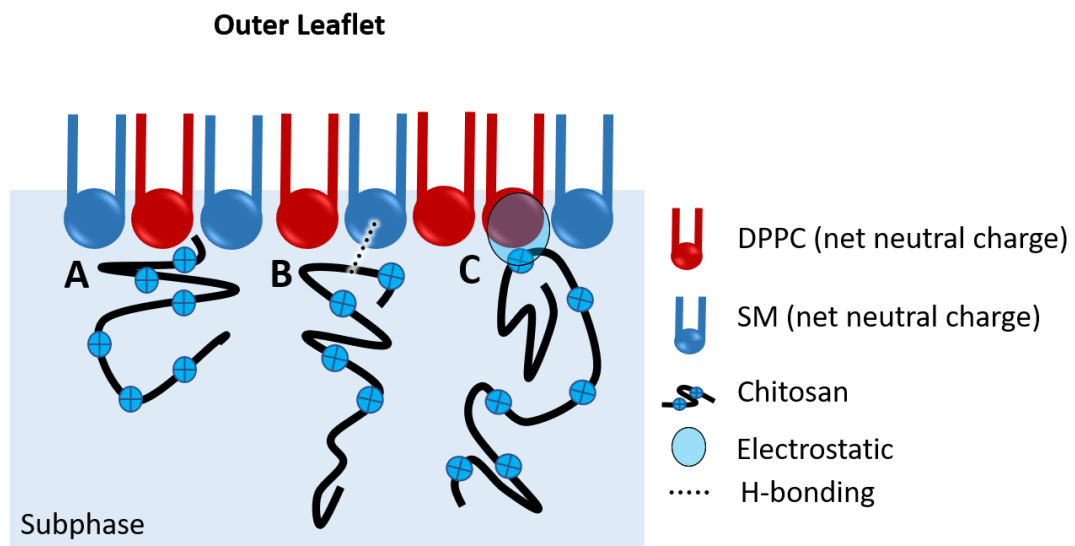
Figure 4.13 Chitosan interaction with OL monolayers A) hydrophobic, B) H-bonding and C) electrostatic attraction.

5 Effect of chitosan on lipid monolayers - Synchrotron experiments

5.1 Introduction

This chapter extends the investigation into the effect of chitosan on the monolayer, by using x-ray methods to elicit structural information about the lateral and transverse order in the monolayer at a molecular level. X-ray reflectivity (XRR) and grazing incidence x-ray diffraction (GIXD) were used because they are complementary to each other. GIXD picks up on the crystalline structure in the lateral (along the interface) plane but does not detect the subphase or headgroup regions. XRR characterises the vertical (along the surface normal) profile of lipid acyl chains and headgroups, and is based on estimating electron densities [102].

These experiments were conducted by injecting chitosan through a lipid monolayer at a surface pressure of 30 mN/m. This method of injection differs to the Langmuir trough measurements in this previous chapter as the injecting needle was not inserted underneath the barrier. This is because 1) the set-up at the synchrotron did not allow for a spinning magnet to distribute the chitosan and 2) the distance between the barrier and the footprint of the beam was too large, even for our long needles. Another difference to the Langmuir trough experiments in the previous chapter is that a second set of measurements of was made after an additional expansion and recompression of the monolayer with chitosan, to see if any changes occurred.

5.2 Results

5.2.1 XRR

5.2.1.i Reflectivity curves

Figure 5.1 presents the normalised reflectivity curves and the fit of the experimental data. Although the reflectivity curves look similar between IL and IL with chitosan, as well as between OL and OL with chitosan, there are subtle differences which give rise

to variation in the electron density profiles caused by the presence of chitosan, as discussed in the next section.
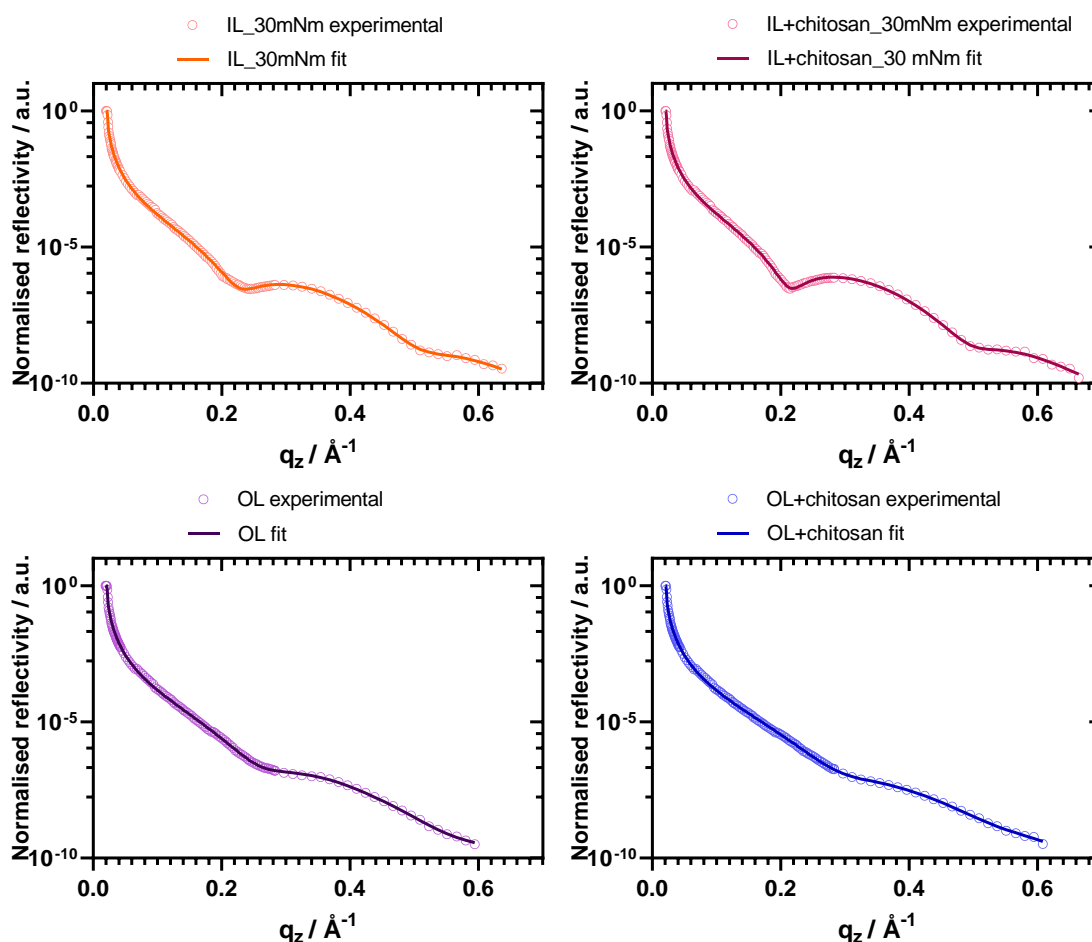
Figure 5.1 Normalised reflectivity curves of IL and OL monolayers at 30 mN/m before and after chitosan injection through the monolayer to the water subphase. The circles represent experimental data and the line is the fit.

5.2.1.ii Electron density profiles and monolayer thickness

Interaction between chitosan and the lipid monolayers seems to have distinctive features depending on the composition of the monolayer. Electron density patterns were obtained by Fourier transform of the normalised density gradient profile (formerly calculated within the function of the scattering vector, $\phi(q')$, [100]) (see equation (2.12)).

When chitosan was added to the IL, a higher electron density was observed in both the region of the lipid headgroup and acyl chains (Figure 5.2A). After an expansion and recompression, this effect was more pronounced (Figure 5.2C). These changes reflect the presence of chitosan in both the headgroup regions, as well as intercalation into hydrophobic regions with the acyl chains.

The electron density for the OL monolayer showed smaller differences between the pure lipid monolayer and the monolayer with added chitosan (Figure 5.2B). Interestingly, after an expansion and recompression, the chitosan appears to redistribute and penetrate deeper into the acyl chain region (Figure 5.2D).
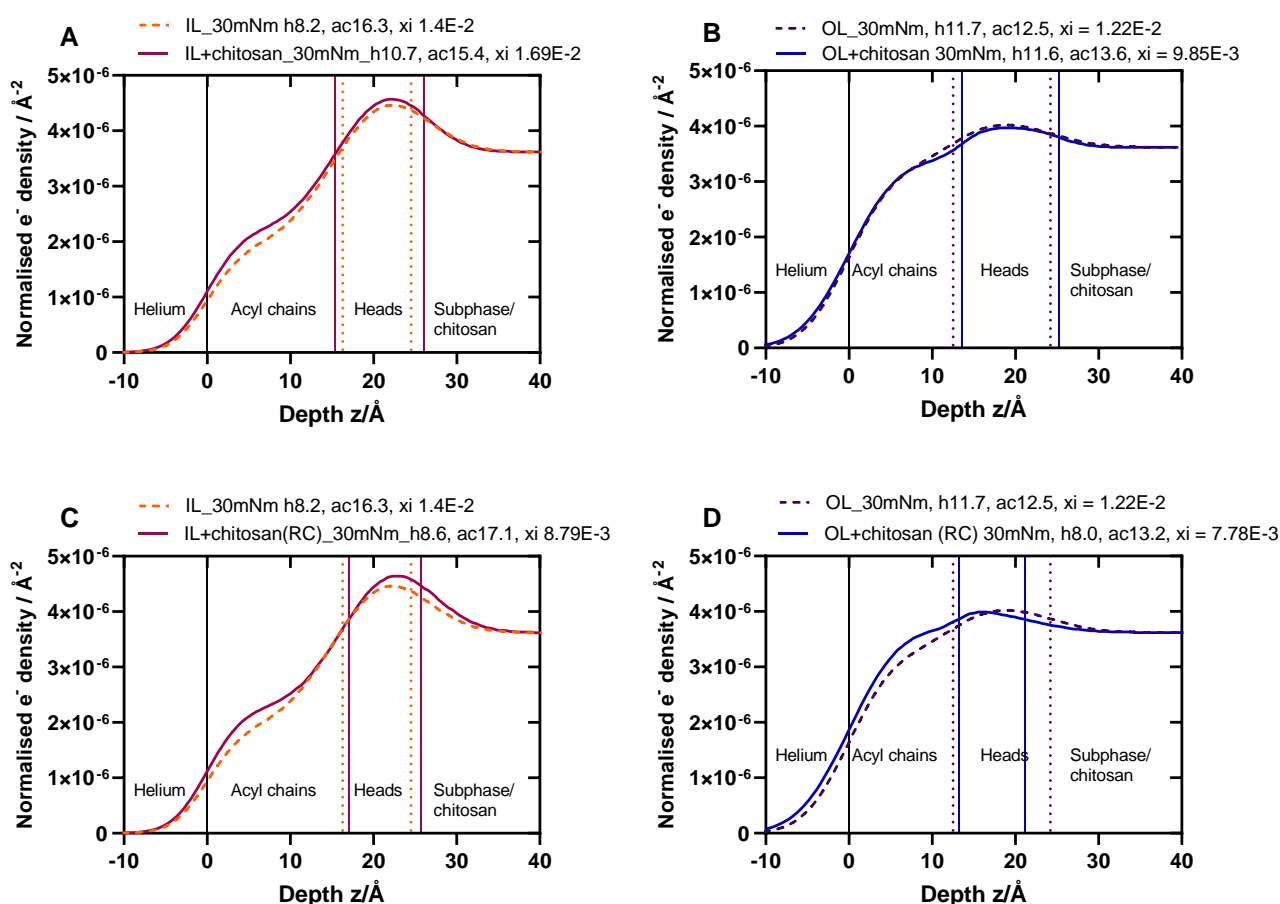
Figure 5.2 Electron density profiles of IL and OL monolayers at 30 mN/m before and after chitosan injection. A and B) show profiles immediately after chitosan injection and C and D) show the profile after an expansion and recompression (RC) of the monolayer. The thicknesses of the headgroups and acyl chain regions can be seen above each graph with the notation 'h (size in Å)' and 'ac (size in Å)', respectively, followed by the χ^2 value.

The thickness of the headgroups of the IL monolayers increased with chitosan addition, from (8.2 ± 2) to (10.7 ± 0.2) Å, before returning to the original thickness after an expansion and recompression (Figure 5.3). The acyl chains changed in thickness in the opposite way although not statistically significant. For chitosan addition to OL monolayers, the thickness of the headgroups did not change beyond the margin of error of the pure OL headgroups. The acyl chain thickness however did increase with the addition of chitosan, from (12.5 ± 0.2) to (13.6 ± 0.3) Å, but returned to within the range of the original thickness after an expansion and recompression (Figure 5.3).
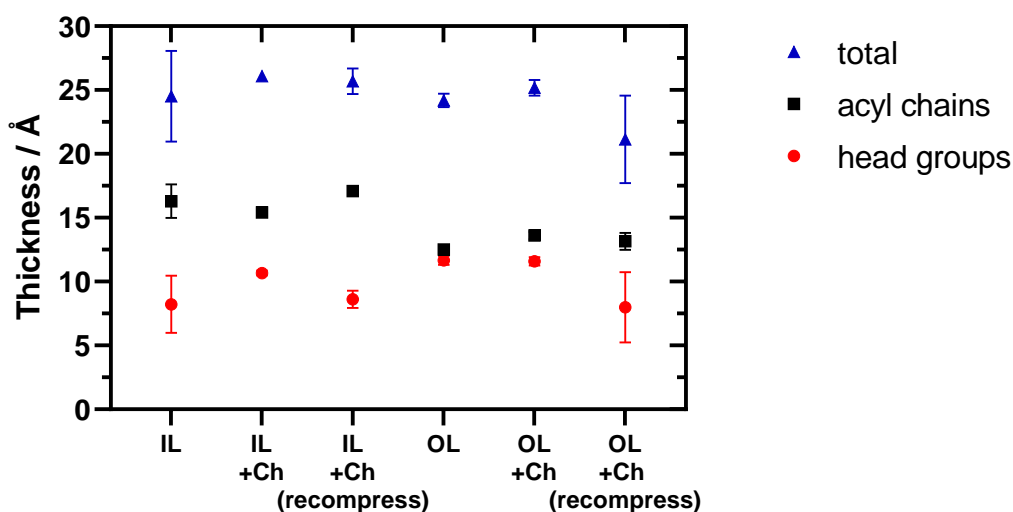
Figure 5.3 Summary of thicknesses of the headgroups, acyl chains, and the total monolayer.

5.2.2 GIXD

All data sets have been fitted using two Lorentzian functions, indicating the presence of two Bragg peaks, which corresponds to distorted hexagonal symmetry [100]. The coherence length, L_{xy}, of IL at 30 mN/m was (41 ± 1) Å for peak 1 and (322 ± 4) Å for peak 2 (Figure 5.4). The distance between lattice points in the lateral plane, the d-spacing, was (4.185 ± 0.002) Å for peak 1 and (4.169 ± <0.001) for peak 2. The length of the unit vector, a, was (4.802 ± 0.005) Å connected by an angle of (119.744 ± 0.001)°, with the area of a unit cell being (20.18 ± 0.04) Å^2.
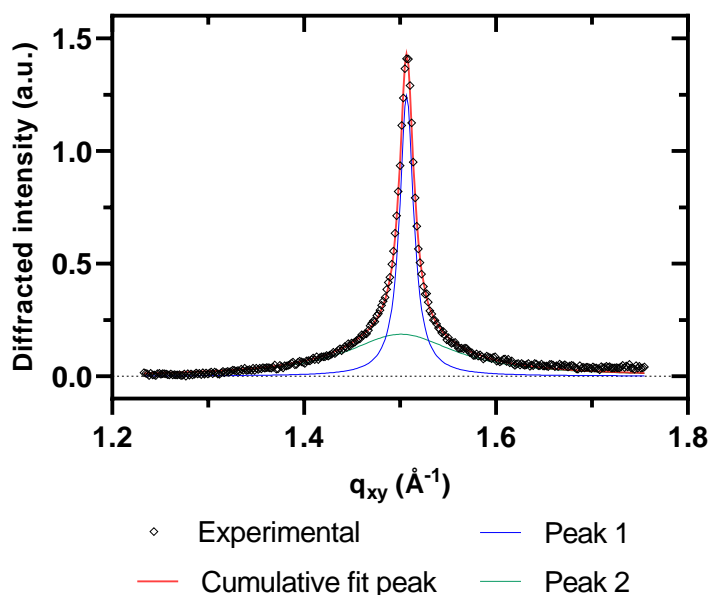
Figure 5.4 Bragg peak from IL lipid monolayer on water.

Once chitosan was injected through the monolayer, the IL peak maxima shifted left on the q_{xy} axis and the distance between lattice points in the lateral plane, *d*-spacing, increased to (4.330 ± 0.005) Å for peak 1 and to (4.179 ± 0.001) Å for peak 2 (Figure 5.5 and see Table 5.1 for summary). L_{xy} increased to (61 ± 4) for peak 1 indicating that chitosan increased lateral order in the {0,1} or {1,0} crystallographic direction. In contrast, L_{xy} decreased to (228 ± 8) Å for peak 2 and after the monolayer was relaxed and recompressed back to 30 mN/m, the L_{xy} decreased further to (193 ± 4) Å for peak 2. This indicates chitosan interaction caused a decrease of lateral order in the {1,-1} crystallographic direction.

The primitive unit cell area increased to (21.15 ± 0.08) Å^2 for the immediate measurement and to (21.7 ± 0.1) Å^2 after an expansion and recompression back to 30 mN/m, indicating incorporation of chitosan molecules between lipids causing expansion. The unit vector, *a,* after chitosan addition, increased to (4.885 ± 0.009) Å for the first measurement and (4.93 ± 0.01) Å after an expansion and recompression. The angle, *γ*, connecting the unit vectors *a* and *b* decreased to $(117.592° \pm <0.001)$ and $(116.483° \pm 0.002)$ after recompression.
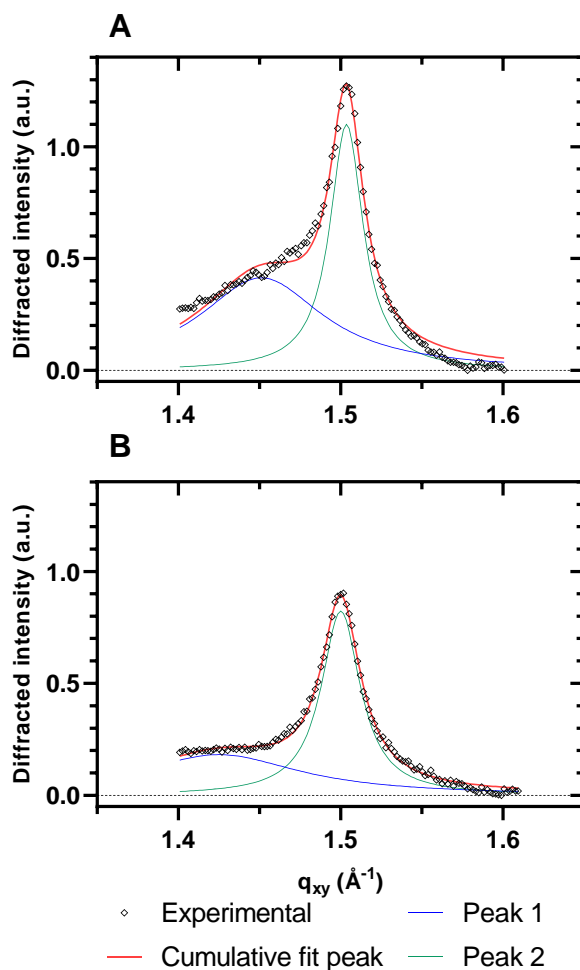
Figure 5.5 Bragg peaks from IL lipid monolayers on a subphase of chitosan and water. A) shows the measurement immediately following chitosan adsorption, and B) shows a measurement after an expansion and recompression.

Due to technical difficulties, the corresponding OL monolayers on a pure water subphase data from ESRF are unable to be shown. Instead, our measurements of OL monolayer on a Tris KCl buffer, pH 7.2, is presented in Figure 5.6A, alongside our GIXD data of OL monolayer on a pure water subphase from another synchrotron facility, DESY. These data were analysed by a member of our group, Beth McGill, and the Bragg peaks are presented in Figure 5.6B for comparison.

The lattice parameters were very similar between the ESRF monolayers on buffer and the DESY monolayers on pure water (see Table 5.1 for comparison). Therefore, the

ESRF OL monolayers on buffer will be used to compare to the ESRF OL monolayers on pure water with chitosan.
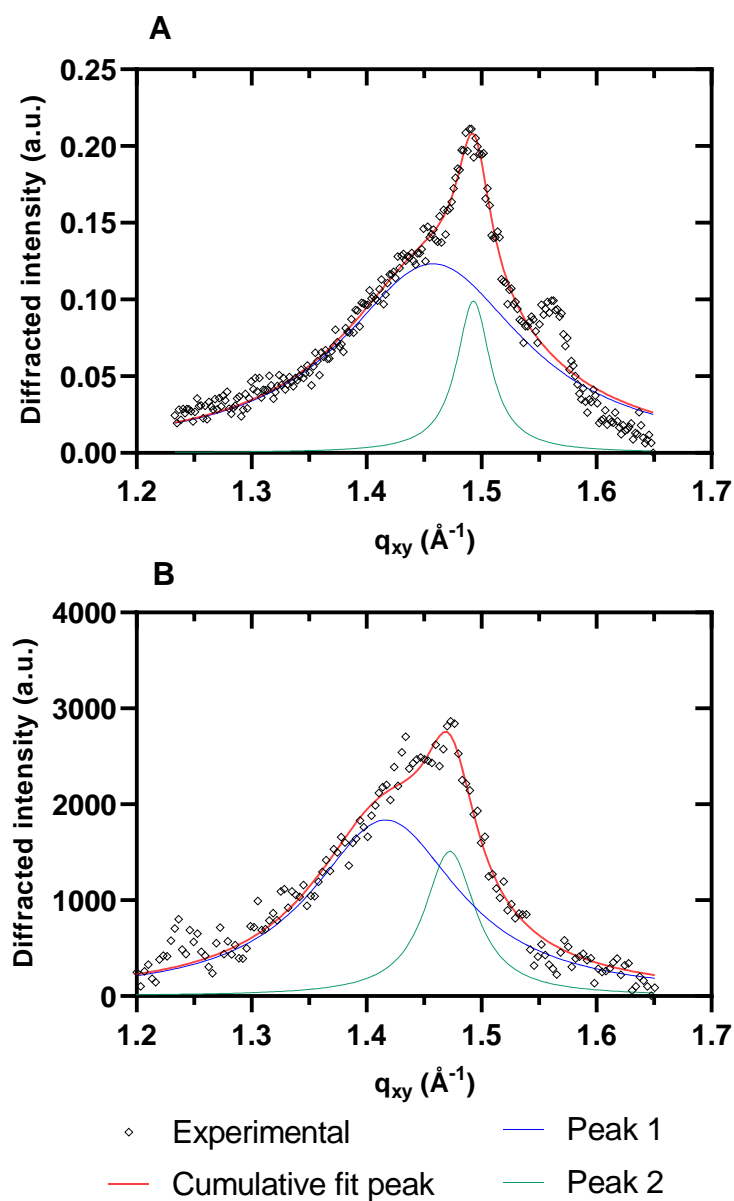
Figure 5.6 Bragg reflections from OL monolayers. A) shows the measurement taken at ESRF, with a buffer subphase and B) shows the measurement taken at DESY on a pure water subphase.

The lattice parameter changes indicate that OL changes in the opposite way to IL upon interaction with chitosan (Figure 5.7 and Table 5.1). The coherence length of ordered domains increased for both peak 1, from (29.2 ± 0.8) to (93 ± 8), and peak 2, from

(157 ± 16) to (296 ± 32) in OL with chitosan addition, although after an expansion and recompression of the monolayer, the peak 2 order decreased dramatically to (82 ± 3).

The area of unit cells decreased from (21.1 ± 0.1) to (20.28 ± 0.05) $Å^2$. The *a* unit vector decreased from (4.90 ± 0.01) to (4.834 ± 0.006) Å and *γ* had increased from (118.393 ± 0.002) to (119.787 ± 0.001)°. The monolayer was then relaxed and recompressed to 30 mN/m, yielding similar parameters again.
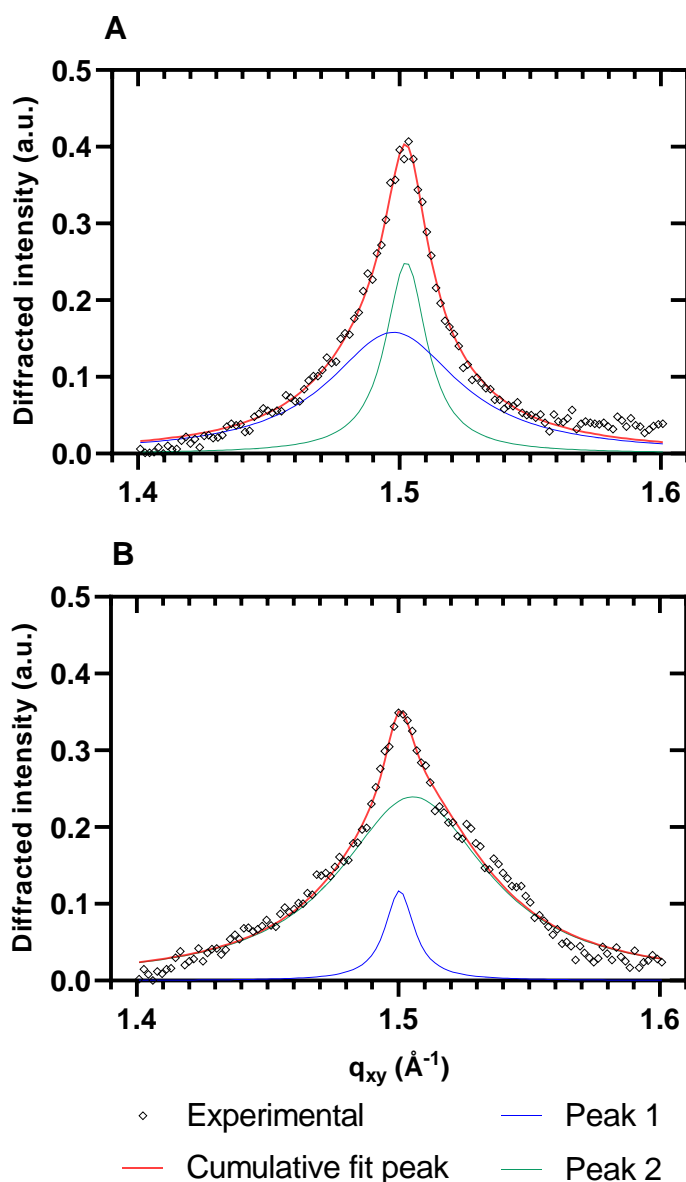
Figure 5.7 Bragg peaks from OL lipid monolayers in a subphase of chitosan and water. A) shows a measurement taken immediately after chitosan adsorption, and B) shows a measurement after an expansion and recompression.

Table 5.1.Summary of lattice parameters of monolayers at 30 mN/m with and without chitosan present in the subphase. Asterisks, *, denote error margins < 0.001. A significant increase from the column to the left is shown with green shading and a significant decrease with red shading. An insignificant change is shaded with grey.

Parameter		IL	IL+chitosan	IL+chitosan recompression	OL (on water (DESY))	OL (on buffer)	OL+chitosan	OL+chitosan recompression
q_{xy} max (Å^{-1})	{(0,1), (1,0)}	1.501 ± 0.001	1.451 ± 0.002	1.425 ± 0.002	1.417 ± 0.005	1.458 ± 0.002	1.498 ± 0.001	1.500 *
	{1,-1}	1.507 *	1.504 *	1.500 *	1.473 ± 0.001	1.493 ± 0.001	1.503 *	1.506 ± 0.001
d- spacing (Å)	{(0,1), (1,0)}	4.185 ± 0.002	4.330 ± 0.005	4.409 ± 0.007	4.44 ± 0.02	4.310 ± 0.007	4.195 ± 0.003	4.188 ± 0.001
	{1,-1}	4.169 *	4.179 ± 0.001	4.188 *	4.267 ± 0.004	4.208 ± 0.002	4.182 ± 0.001	4.173 ± 0.002
FWHM (Å^{-1})	{(0,1), (1,0)}	0.138 ± 0.004	0.093 ± 0.005	0.122 ± 0.009	0.157 ± 0.006	0.194 ± 0.005	0.061 ± 0.005	0.013 ± 0.002
	{1,-1}	0.018 *	0.025 ± 0.001	0.029 ± 0.001	0.054 ± 0.008	0.036 ± 0.004	0.019 ± 0.002	0.069 ± 0.003
L_{xy} (Å)	{(0,1), (1,0)}	41 ± 1	61 ± 4	46 ± 3	36 ± 1	29.2 ± 0.8	93 ± 8	425 ± 78
	{1,-1}	322 ± 4	228 ± 8	193 ± 4	105 ± 15	157 ± 16	296 ± 32	82 ± 3
Area (Å^2)		20.18 ± 0.04	21.15 ± 0.08	21.7 ± 0.1	22.2 ± 0.3	21.1 ± 0.1	20.28 ± 0.05	20.20 ± 0.03
a (Å)		4.802 ± 0.005	4.885 ± 0.009	4.93 ± 0.01	5.00 ± 0.03	4.90 ± 0.01	4.834 ± 0.006	4.824 ± 0.003
γ ^{o}		119.744 ± 0.001	117.592 ± 0.001	116.483 ± 0.002	117.368 ± 0.005	118.393 ± 0.002	119.787 ± 0.001	119.773 ± 0.001

5.3 Discussion

5.3.1 Inner leaflet

The L_{xy} values show that the IL crystalline domains had more lateral order in the {1,-1} crystallographic direction (represented by peak 2) than the {0,1} or {1,0} crystallographic directions (both represented by peak 1). In agreement with this, monolayers of DPPS, the dominant component of the IL mix, had similar order, where the crystallographic direction {1,-1} was more ordered than that of {0,1} or {1,0} [117].

5.3.2 Outer leaflet

As with the IL, the OL crystalline domains were also more ordered in {1,-1} than {0,1} or {1,0} and in agreement with this, this order has been shown previously with monolayers of the dominant component of the OL mix, DPPC [117]. The OL monolayers exhibited more extreme distorted hexagonal symmetry the IL monolayers.

5.3.3 Differences between inner and outer leaflet

In both {0,1} or {1,0} and {1,-1}, the ordered crystalline domains were smaller for OL than IL, showing that OL has less order in both crystallographic directions. There was a larger area per molecule seen with OL, compared to IL and this was shown by several parameters: the OL peak maxima were lower along the q_{xy} axis, compared to IL which indicates larger area per molecule, the *d*-spacings (distance between lattice points, as described in Figure 5.8) in both peaks were higher in the OL monolayer compared to the IL monolayer, and the primitive unit cell area, and *a* was larger in OL than IL. The comparatively small primitive unit cell area of the IL suggests tight packing of the lipids. This tight packing could be largely due to DPPS and its influence on the other predominant lipid species in this mix, DPPE. This suggestion is made because DPPS has been shown to have a strong effect in decreasing area size of DPPC monolayers [117]. Further, PE headgroups can form hydrogen bonds with other lipid headgroups [118] contributing to a more stable monolayer than DPPC monolayers, as suggested previously [119].
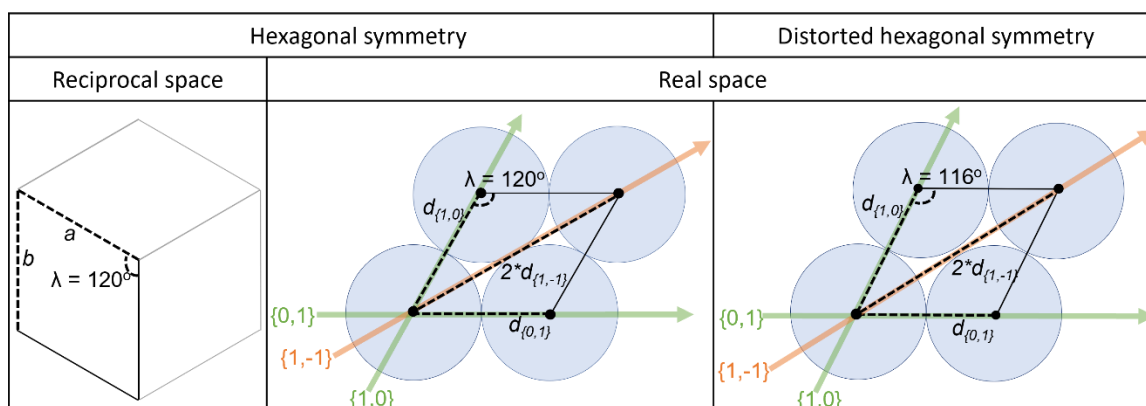
Figure 5.8 Examples of unit cells in reciprocal space and in real space. The vectors
a and *b* represent the dimension of the reciprocal unit cells (see equation (2.14)).
The coloured arrows represent crystallographic directions implied in real space. The
degeneracy of the signals from the {0,1} and {1,0} crystallographic directions is
indicated by their identical green colouring. The *d*-spacings (representing lipid chain
spacing) are indicated with their corresponding crystallographic direction in
subscript. Black dots represent the basis of the lattice, and the blue shaded circles
represent the space occupied by a lipid.

5.3.4 Differing effects of chitosan

Chitosan clearly induced large structural changes to the IL monolayer, where
there was an increase in electron density in both headgroup and acyl chain
regions, an increase in headgroup thickness, expansion of the IL monolayer, and
a notable decrease in lateral crystalline order of the acyl-chains in the {1,-1}
direction. These effects paint a picture of the chitosan polymers adsorbing to the
headgroups, causing lipids to move further apart and penetrating into the acyl
chain region, disrupting the highly ordered composition of lipid domains. In
addition, chitosan appears to have a preferred orientation when interacting with
the monolayer as shown by the change in coherence length more prominently
seen in one crystallographic direction.

In contrast to the IL, chitosan addition to the OL monolayer caused a general
increase in lateral crystalline order of the acyl chains, especially in the {0,1} and
{1,0} directions. The expansion and recompression after chitosan addition to the
OL had a large impact on chitosan incorporation, where we saw a significant
increase in electron density of the acyl chains and a significant decrease in
headgroup thickness, suggesting chitosan incorporated into the acyl chain region

and caused headgroups to become less tilted in the subphase, altering their effective thickness.

These stark differences in chitosan effect on the two monolayer types can again be explained by the behaviours of the dominant lipid species of IL versus OL, as in chapter 4. The conversation can now be continued further, with the information of the orientation of the chitosan with the IL lipids (DPPS and DPPE) and the OL lipids (DPPC and SM) and the effects of chitosan on the lateral crystalline structure of the monolayers.

5.3.4.i   DPPS and DPPE

In a previous study, chitosan disrupted the domain structure in negatively charged DPPG monolayers, causing them to become more homogenous, and causing expansion [71]. If a similar effect occurs with the negatively charge DPPS lipids in IL, then that could explain expansion, and the decrease in chain order (due to increased space for acyl chains, as chitosan spreads out the lipid headgroups).

The DPPE conical shape allows hydrophobic interaction of the acetylated moieties (uncharged) of chitosan with the acyl chain region which would explain the increase in electron density in the acyl chain region. As discussed in chapter 4, DPPE can form hydrogen bonds within and between lipids, and chitosan in the monolayer would competitively hydrogen bond to the amine groups of DPPE, especially at higher surface pressures [114]. This competitive binding would disrupt the close associations between lipid headgroups [120] and therefore could cause the disruption to lateral crystalline order that is observed in our data.

5.3.4.ii DPPC and SM

As discussed in chapter 4, the cylindrical shapes of DPPC and SM cause restricted access for chitosan to the acyl chain region. However, a second cycle of expansion and compression of the monolayer in the presence of chitosan would allow access of chitosan molecules to the acyl chain region, which is evidenced by the increased electron density in such experiments (Figure 5.2D).

DPPC lipids have large headgroups causing the chains to tilt, which could explain why the acyl chains are more disordered in the OL-only than the IL-only monolayers. It has previously been observed that the adsorption of phospholipase A to a DPPC monolayer causes less tilting of the chains [121]. If

the association with chitosan had a similar effect, this could also contribute to an increased packing of lipids, reducing area/molecule.

Chitosan interaction with DPPC has previously been shown to cause chitosan-rich domains causing large spaces between chitosan-poor domains with high lipid packing and highly ordered acyl chains [71]. This effect could explain the increase in acyl chain order seen in the OL with chitosan, and the increase in acyl chain thickness (due to less tilting), as well as the apparent compression of the OL monolayer.

5.3.5 Summary

In summary, the structural changes to the monolayer, as elucidated through synchrotron methods are largely in agreement with the hypotheses made in chapter 4 (summarised in Figure 4.12 and Figure 4.13). The results in this chapter also indicate formation of domains, rich in chitosan in the OL monolayers. In contrast, the IL monolayer data could suggest that the composition becomes more homogeneous with chitosan addition.

6 Conclusions and future work

The overall aim of this thesis was to use a combination of biological and physical approaches to investigate the interactions of lipid membranes and exogenous, membrane-active biomolecules.

The University of Exeter supports interdisciplinary approaches to research, and it is within that environment that this PhD was undertaken. Coming from a broad zoological undergraduate degree, followed by a molecular biology masters degree, the challenge for me was to bring together biological and physical research techniques. This involved different ways of thinking, different supervisors and different laboratories, which required adaptability and flexibility, and a lot of learning.

Initially, my experimental design took the approach of a biologist, which was to collect many observations of a biological system, and seek to find a pattern using statistical tests. However, within the physics laboratory, I adapted to a different approach, which was to identify a physical property of membranes to test, establish a biological model, and calculate the outcome using specific mathematics to quantify the property.

These two approaches can be seen in the two parts to my thesis where the haemolytic effects of Etx are characterised using statistics to quantify the activity in under various conditions (temperature, concentration, and Etx mutation). This resulted in a jigsaw puzzle of clues with which to answer, and elaborate on, my hypotheses. The second part centred around the use of Langmuir trough monolayers as a model for lipid membranes. This resulted in precise information on the behaviour of this system with which to answer my research questions, but with the caveat that the behaviour could be very different in biological conditions.

The objective to examine the haemolytic effects of Etx with RBCs was met by taking a count of cells that had lost their haemoglobin content after addition of Etx and creating a lysis curve over time.

The objective to investigate the importance of certain amino acids in the binding and pore-formation stages of Etx action on RBCs was met not only by comparing lysis curves, but by providing evidence of hydrophobic binding with lipid bilayers,

and by western blot detection of lipid-bound monomers and oligomers in extracted RBC membranes. The significant findings from this were: that Y43A exhibited the same behaviour as WT, despite having attenuated effects on other cell types (CHO-hMAL, M. Bokori Brown, to be published); that Y42A receptor-binding to RBCs was impaired, which led to decreased oligomer formation and decreased haemolysis (however hydrophobic-binding appeared unaffected); that H162A did not have impaired haemolytic effects on RBCs (at 37 °C) or impaired pore-formation in lipid bilayers (however this variant did exhibit reduced binding which led to reduced oligomerisation and haemolysis of RBCs).

The objective to characterise chitosan induced changes in surface pressure and viscoelasticity of lipid monolayers, using a Langmuir trough, was met by manipulating the area/molecule of monolayers, recording surface pressure changes and using static dilatational elasticity and dynamic dilatational elasticity calculations on the experimental data. The main findings from these experiments are summarised in Figure 4.12 and Figure 4.13 and include: that chitosan increases the stiffness of IL monolayers, that chitosan causes expansion of IL and OL monolayers but particularly IL between surface pressures of 20 – 30 mN/m.

The objective to obtain structural information of the interaction of lipid monolayers with chitosan using x-ray techniques was met after a visit to the ESRF synchrotron facility in Grenoble, where we used x-ray reflectivity and grazing incidence x-ray diffraction techniques. The findings from this reinforced several of the main findings of the monolayer experiments in chapter 4, where chitosan appeared to penetrate into the acyl chain region in IL monolayers (and OL after gaps were created by a monolayer expansion and recompression), and that chitosan caused an expansion to IL. In contrast to chapter 4, chitosan caused an apparent compression of the OL monolayer; however, this could be an effect of the formation of chitosan-rich domains and lipid-rich domains.

The Etx research in this thesis could be used to inform the early stages of vaccine discovery to protect against Etx effects in humans. Specifically, the finding that H162A toxicity is not attenuated for RBCs at physiological temperature.

The chitosan research is a contribution to the academic and medical communities which are developing the use of chitosan in drug delivery systems and as drugs

themselves. Specifically, the strong attraction of chitosan to the IL of mammalian cells as seen in this thesis, is very important information for the many cases where chitosan can access cell membranes. It is possible that any lysed cells in the target environment would have a competitive affinity to chitosan as IL segments are likely to be exposed. In the case of disease, or indeed a puncture wound from a vaccination, the number of broken cells would be higher than normal, possibly reducing the drug delivery to the target live cells.

6.1 Recommendations for further research

The natural next step of this research is to take the Etx results further and approach the hypothesis of thermal fluctuations being important for H162A pore-forming ability. A technique used in the Petrov laboratory is to record thermal fluctuations of RBCs, gaining information on the extent of fluctuation by observing amplitude deviations from the mean shape. The Petrov laboratory specialises in single cell analysis and therefore a single cell could be characterised in terms of fluctuation, and that same cell re-measured after Etx H162A toxin is flushed through the medium. From there, association of fluctuation and time to lysis could be obtained. If there is an association showing a reduced time to lysis with increased thermal fluctuations, it would provide strong support for the thermal fluctuations hypothesis, which could be used to inform and improve laboratory experiments (for example, using lipid models with a high degree of fluctuation).

It would also be very useful to examine pore-formation by Etx variants on lipid bilayers which are not homogeneous, and which represent physiological cells more closely with unsaturated acyl chains. Bilayers could then be designed to model such properties as fluidity, thermal fluctuations, domain structure, and electrostatic effects.

It would be interesting to conduct an experiment on whether chitosan has a protective effect against (or a 'drug delivery' effect for) Etx or other pore-forming toxins, especially now that the physical changes to mammalian-representative monolayers by chitosan have been characterised. This could be carried out using some of the methods mentioned in this thesis but also by fluorescence microscopy where tagged protein is added to cells which have been pre-incubated with and without chitosan. Toxin localisation on the cells could then be

visualised using a confocal microscope. If chitosan is protective, we might expect to see a layer of toxin around the cell but no haemolysis.

7 Appendix

7.1 Ethics forms
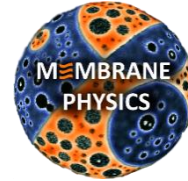
PARTICIPANT INFORMATION SHEET (PIS)

Template version 1.1, Sep 2018

Date of customised PIS: 19th December 2018

Research Project: Red Cell Biophysics

Operator: Dr Peter Petrov

Thank you for showing an interest in this project. Please read this information sheet carefully before deciding whether to participate. If you decide to participate, we thank you. If you decide not to take part, we thank you for considering our request.

Purpose of this study

The aim of this study is the development of new experimental methodologies to determine key physical properties of human red blood cells such as membrane elasticity and electric potential. Furthermore, the involvement of the red cell in diseases such as diabetes mellitus, arteriosclerosis and others may be examined. The new methodologies will be used to investigate how the membrane physical properties influence interactions between cells and other molecules of interest and bio-chemical signalling of the red cells. We shall seek to establish whether membrane deformation, mechanical properties and or oxidative stress affect the release of the signalling agents such as ATP (vasodilator) and sphingosine-1-phosphate (signalling sphingolipid and regulator of vascular and immune systems). We also aim to investigate the effect of the so-called pore-forming proteins on

the physical properties and integrity of red cells, and their potential to influence of the release of signalling agents. Red cells obtained from volunteers will be studied with experimental methods including (but not limited to) optical microscopy and bio-luminescence assays.

Description of participants

For this study, we are looking for individuals aged 21 or above who are in general good health.

What does this study involve for me?

For this study, a small amount of blood will either be collected via finger-prick with a lancet device or be drawn from a vein in your arm with a hypodermic needle. The latter procedure will be performed by a trained member of staff, usually a phlebotomist, doctor or nurse. A tourniquet is placed around your arm just above the elbow, the area is cleaned and then a small needle is inserted into a vein in the inner arm. Blood is withdrawn into sample bottles and the needle is then removed. Pressure is applied at the site with a piece of cotton wool or gauze until the bleeding has stopped and then a small plaster is applied. Please tell the person taking the blood if you are allergic to plaster adhesive.

In most cases, blood will be taken first thing in the morning. In an attempt to standardise conditions between participants, we may ask you to fast (no food or drink), either from 10 pm the night before or 2 hours prior to the procedure. This will be discussed in detail with you during the consent process.

What are the risks and/or discomfort associated with this investigation?

Putting the needle into the arm involves a pinprick sensation but after that, the rest of the procedure should be quite painless. Some people continue to feel some discomfort or pain probably because of irritated nerves under the surface of the skin, but this should settle quite quickly. If not, you should go to see your GP or a member of hospital staff.

You may get a bruise or a small lump after having blood taken. It can often look very dramatic, appear away from the site where the blood has been taken, and/or remain visible for a few days following the procedure. This will usually settle by itself and fade away in time, but if in doubt, you should see your GP or a member of hospital staff. Some conditions may increase the risk of bruising. These include:
- drugs such as Warfarin or Aspirin
- conditions such as a bleeding disorder or low platelets (thrombocytopenia)
- when it is hard to get a vein, for example if the arm is swollen (oedema)
- elderly patients.

To help reduce this risk as much as possible, please tell the person taking the blood if you have any such conditions or if you have had a problem previously after a blood test. Pressing firmly on the site until the bleeding has stopped should help to reduce any bruising. If possible, keep the arm slightly raised and avoid too much movement of the arm, such as lifting or carrying heavy parcels, for at least an hour after the blood test. Should you experience excessive bruising or prolonged bleeding, then apply further firm pressure to the area. A few ice cubes wrapped in a towel may help reduce any swelling and bruising.

Do I have to take part?

You are under no obligation to take part, it is purely voluntary. If you decide not to take part, it will not affect your rights, wellbeing, assessments/appraisals or interactions with the academic research team, including whether you are a student or colleague.

Can I change my mind and withdraw from the Project?

You may withdraw from participating in the project at any time without any disadvantage to yourself of any kind.

Who is overseeing these investigations?

These investigations are being collectively overseen by Dr Peter Petrov (co-lead of research group and Principal Investigator of the research project), Professor Peter Winlove (co-lead of research group), Dr Bob-Dan Lechner (Research Fellow) and Miss Beth McGill (PhD student).

What will happen to my research data?

The research data that we collect will be used to develop methodology for the determination of red cell physical properties and to assess the applicability and reliability of those newly developed methods. Also, the variability of the accessible parameters of those measurements will be determined. For example, if we collect multiple measurements from you on separate occasions we can examine the day to day variability of these assessments. By combining your data with data collected from other participants, we can also assess the variability of this assessment between participants. Collectively, this data will help inform us of the reliability of the method and the natural variability of the parameters, ensuring the integrity of our studies as well as providing valuable information needed for designing future studies.

Although this data is primarily for use within the research department, it may also be presented at conferences or published in scientific papers in the future. In these cases all presented data will be anonymised.

Will my personal data be confidential?

For this study, we only gather a minimum of patient information. Your personal data (e.g. name, age group, gender) will be confidential and will only be accessed by relevant members of the Biomedical Physics research team. Any data that is presented outside of the immediate research team will be completely anonymised.

What if the research team discover a health concern?

Our research assessments are for research purposes only and have no clinical significance nor will genetic information be obtained. If we observe an unexpected finding that might be related to a health concern using these techniques, we will inform you of our observations. You can then decide if you want to consult your GP on that issue.

THANK YOU FOR TAKING THE TIME TO READ THIS PARTICIPANT INFORMATION SHEET.

If you would like further information please contact one of the following:

Dr Peter Petrov	p.g.petrov@exeter.ac.uk	01392 724139
Dr Bob-Dan Lechner	b.lechner@exeter.ac.uk	01392 725825
Miss Beth McGill	bmm205@exeter.ac.uk	01392 727467

Complaints

If you have any complaints about the way in which this study has been carried out, please contact the University of Exeter's College of Engineering, Mathematics, and Physical Sciences' Ethics Committee:

Jo Parson or Alex Corbett
Email: ethics@exeter.ac.uk

**This project has been reviewed and approved by the
University of Exeter Department of Physics and Astronomy Research Ethics
Committee
REFERENCE NUMBER: eEMPS000064**
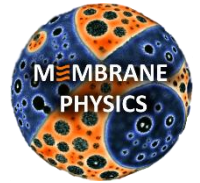
The training and establishment of research assessments within Bio-Medical Physics

CONSENT FORM FOR PARTICIPANTS

VERSION NUMBER: 3.2   **DATE: December 2018**

Research Project: Red Cell Biophysics

I have read and understood the Participant Information Sheet (PIS) Template (version 1.1, September 2018) that was completed on 19th December 2018 concerning this project. All my questions have been answered to my satisfaction. I understand that I am free to request further information at any stage.

I understand that:

1. my participation in the project is entirely voluntary;

2. I am free to withdraw from the project at any time without any disadvantage;

3. my data, including limited personal data (e.g. name, age group, gender), will be retained indefinitely in secure storage within the bio-medical physics group;

4. my data may be accessed by members of the bio-medical physics research team;

5. access to my study data files may be sought by auditors, monitors, regulatory authorities and ethics committees;

6. if I choose to withdraw from the study, any data already collected may be used in conjunction with this study;

7. the results of the project may be published but my anonymity will be preserved;

8. I agree to take part in this project.

....   ………………   ....
(Printed name of participant)   (Year of birth)   (Gender)

....……….........................   .……….........................
(Date)   (Signature of participant)   (Unique participant number)

....……….........................
(Printed name of researcher) (Date)   (Signature of researcher)

7.2 Amoebapore production

7.2.1 Introduction and background

Entamoeba histolytica is the causative agent of amoebiasis, a disease of severe diarrhoea and liver abscesses. Amoebiasis kills approximately 55.5 thousand people annually [122] and is the third most common cause of death by a parasite [123]. Developing countries are the most vulnerable due to poor sanitation and lack of available treatment. It is also one of the most common causes of traveller's diarrhoea in those that travel to tropical countries [124].

E. histolytica has two stages to its lifecycle, with humans as their definitive host after an inactive, cyst stage in the outdoor environment. Infection occurs by ingestion of faecal contaminated water containing cysts. These cysts can survive in the environment for weeks and when ingested by a host they undergo excystation in the large intestine and become trophozoites [125]. The trophozoite stage parasites are mobile and feed from bacteria and food in the intestine [125]. Trophozoites then undergo encystation in the colon, forming cysts that are ready to be expelled to the environment and await to be ingested by a new host. It is the cyst stage that is infectious to new hosts but it is the trophozoite stage that can release the pore-forming toxin and cause amoebiasis.

Toxins are ubiquitous in nature and have various functions and mechanisms of action. Amoebapore functions by destroying both the human host cells and any other cells (e.g. bacteria) that it can reach. There are three amoebapore isoforms, all approximately 8 kDa in mass, for which amoebapore A is the most abundant [126]. Amoebapore A, and likely B and C also, is made up fully of alpha-helices [126, 127]. Importantly, amoebapore mechanism of action is to form pores in the lipid bilayer membrane leading to ionic imbalance, a rush of water into the cell, and cell lysis. Therefore, it falls into the class of pore-forming toxins.

7.2.2 Amoebiasis disease and treatment

Infection with *E. histolytica* in humans is asymptomatic in 90% of cases and is cleared by the immune system. However, for the 10% of those that develop symptoms, it can be a debilitating and fatal disease. Amoebic colitis symptoms

are similar to those of inflammatory bowel disease (IBD) with abdominal pain and bloody diarrhoea and therefore can be mis-diagnosed [128]. This mis-diagnosis is dangerous because the treatment of steroids for IBD suppresses the immune system and therefore increases the survival of the amoeba, resulting in likely death of the patient [128]. A rare complication can occur where patients develop sudden-onset (fulminant) amoebic colitis which has a high mortality rate [129-131].

The amoeba can also leave the intestinal area and cause disease elsewhere. The most common extra-intestinal manifestation is amoebic liver abscess (ALA). This occurs when amoebae break through the colon mucosal wall (Fig. 1) and enter the portal venous system. Patients can develop ALA 8-20 weeks after exposure to the parasite [132]. Other extra-intestinal manifestations include lung abscess and brain abscess.

Figure 7.1 Characteristic amoebic colitis. The mucosal wall has been breached and amoeba have spread below [133].

7.2.3 How *Entamoeba* destroys human cells - Pore-forming toxins A, B, and C

E. histolytica was named such because of its ability to lyse host cells. The process of cell lysis was observed to involve a fall in the transmembrane potential and so it was thought that a membrane-active substance was secreted from the parasite [134, 135]. This substance was subsequently found to be the amoebapore toxin for which there are three isoforms: A, B, and C [126, 135].

7.2.4 Amoebapore Structure

Amoebapore A is the most abundant with an A:B:C ratio of 35:10:1 detected in a population of trophozoites [126]. It is not certain whether single parasites

produce all three isoforms at once. All three amoebapores are 77 residues long and analysis by mass spectrometry revealed the molecular masses of the isoforms are 8.2, 8.3, and 8.0 kDa of A, B, and C respectively [126]. They have variations in their residues but also share some similarities [126]. All three amoebapores contain the six cysteine residues that are involved in the 3 disulphide bonds found in the characterised secondary structure of amoebapore A [127]. Amoebapore A appears to be fully made up of alpha-helices [127] and this is likely to be the case with B and C as well [126].

7.2.5 Amoebapore Function

After amoebapore A inhibition the parasite was found to be less pathogenic after there was a decrease in cell lysis [136]. In addition, when the amoebapore A gene, ap-a, was silenced at the transcription level, the parasites also became avirulent [137]. A study showed that amoebapore A was not the only protein involved in pore-forming activity [138] Subsequently amoebapores B and C were also found to be potent through an assay measuring depolarisation of a membrane after toxin addition [126]. Therefore, despite amoebapore A being far more abundant, B and C also can contribute to virulence.

The cytolytic activity of amoebapore is dependent on *E. histolytica* binding to the host cell membrane. This process is carried out via a lectin on the *E. histolytica* surface which binds to galactose and N-acetyl-D-galactosamine on the host membrane [139, 140]. A histidine residue at the C-terminal of amoebapore allows dimerisation of the molecules and this is dependent on pH, with the optimum at 5.2 [141, 142]. Dimers then oligomerise to form a hexameric pore in the membrane [143].

While the biological function and structure of amoebapore have been investigated to an extent, much less is known about the physical interactions behind pore formation. Previous experiments have shown that amoebapore A preferentially inserts into negatively charged membranes [144]. However, questions on how physical properties of the cell membrane such as lipid composition affect toxin activity are largely unanswered and the aim was to produce amoebapore to investigate this.

7.2.6 In summary

Amoebiasis is a disease that causes death in the world's lowest-income areas as well as causing severe diarrhoea in travellers to these regions. There are drugs to treat the parasite infection however resistance has been observed [24] and appropriate treatment is often hard to access in endemic areas. Therefore, it is important to be continuously looking at what factors are essential to *E. histolytica* survival that may inform future therapeutic strategies. Pore-forming toxins are common virulence factors to many pathogens and studying the *E. histolytica* toxin amoebapore will aid understanding of how this parasite causes destruction in the human host. Using biophysical methods to analyse this system is important because it could answer questions that are not able to be addressed by solely biological approaches.

7.3 Methods

As the DNA sequence information of amoebapore is available online, the gene was cloned into a plasmid which was transferred to, and expressed in, *Escherichia coli* in the laboratory similar to a previous publication [145]. The amoebapore protein will then be purified from *E. coli* using chromatography to separate all the proteins. Sodium dodecyl sulphate-polyacrylamide gel electrophoresis (SDS-PAGE) was performed on the protein fraction to see if it contain amoebapore.

7.3.1 Plasmid construct of *Entamoeba histolytica* amoebapore A with a cleavable His-tag for protein expression

The DNA sequence of amoebapore A can be found on Genbank, NCBI, with the accession number M83945 (https://www.ncbi.nlm.nih.gov/nuccore/M83945). Expression of the amoebapore gene alone would produce the target protein however it would be difficult to isolate it from other protein products in the mixture. Therefore, the gene was designed to contain a His tag which is commonly used to isolate a target protein from a mixture. In addition, the gene was designed to contain a cleavage site to cleave off the His tag after the purification steps. A Tobacco etch virus (TEV) cleavage site [146], which is targeted by TEV protease, was incorporated into the gene (Fig. 2 and 3). The DNA sequence was optimised for production in *E. coli*.

His tag	TEV cleavage site	**Amoebapore gene**
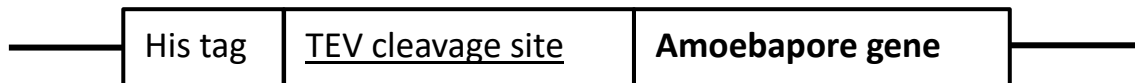
Figure 7.2 Schematic of the gene design set up. The cleavage site is positioned between the amoebapore gene and the His tag. The horizontal lines on either side represent the plasmid that this gene is cloned into. The plasmid construct was designed based on a previous method [145], however, here a TEV cleavage site is used (Figure 2).

```
MSGSHHHHHHSSGENLYFQGGEILCNLCTGLINTLENLLTTKGADKVKD
YISSLCNKASGFIATLCTKVLDFGIDKLIQLIEDKVDANAICAKIHAC
```

Figure 7.3 Amino acid sequence of the plasmid construct. The His-tag is in regular font, the TEV cleavage site underlined and the amoebapore A protein in bold.

```
ATGAGCGGCAGCCACCACCACCATCACCATAGCAGCGGCGAAAACCTGT
ACTTCCAAGGCGGCGAAATCCTGTGCAATCTGTGCACCGGTCTGATCAA
CACCCTGGAGAACCTGCTGACCACCAAGGGCGCGGACAAGGTGAAAGAT
TACATCAGCAGCCTGTGCAACAAAGCGAGCGGTTTCATTGCGACCCTGT
GCACCAAGGTTCTGGACTTTGGCATCGATAAACTGATTCAACTGATTGA
GGACAAGGTGGATGCGAATGCGATTTGCGCGAAGATTCATGCGTGCTAA
```

Figure 7.4 The DNA sequence was optimised for *E. coli* by Genscript a with a stop codon (TAA) at the end.

A pET9a plasmid (Novagen) (Figure 5), which is a standard T7 vector, was used and the gene cloned into Nde1 and BAMH1 cloning sites. The final DNA sequence ordered, with the cloning sites in green italics, is shown in Figure 6. As Nde 1 cloning site is CATATG and the first three bases of the sequence is ATG, there was no need to enter ATG twice in the sequence.
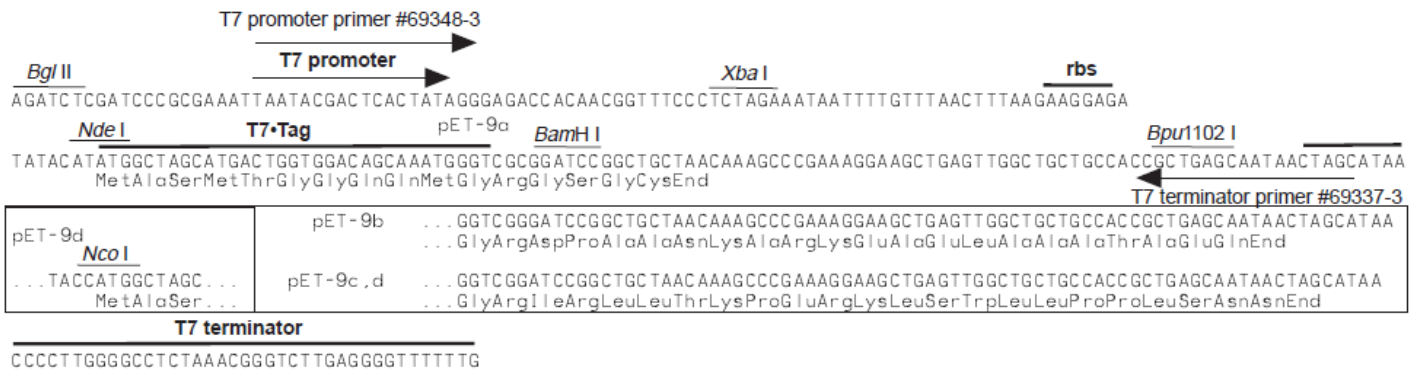
Figure 7.5 pET9a vector containing a T7 promoter (Novagen). The gene was cloned into the Nde1 and BAMH1 cloning sites.

Figure 7.6 DNA sequence with cloning sites in green italics

7.3.2 Cell free protein expression

As amoebapore is used by *E. histolytica* to lyse bacterial cells, it is assumed in the literature that producing this toxin in *E. coli* will not work. Therefore a cell-free system, based on a previous study [145], was tried.

In summary, 300 µl cell-free reaction mixture was placed in dialysis tubing (MWCO: 12-14 kDa) inside a polypropylene tube containing 3 ml outer buffer. Dialysis was performed at 30 °C with shaking over 16-20 hours. The insoluble fraction of the mixture was removed by centrifugation.

Cell free reaction ingredients:

- 55 mM HEPES/KOH pH 7.5
- 1.7 mM dithiothreitol
- 1.2 mM ATP

139

- 0.8 mM each of CTP, GTP and UTP
- 0.64 mM 3',5'-cyclic AMP
- 68 µM folinic acid
- 27.5 mM ammonium acetate
- 208 mM potassium glutamate
- 80 mM creatine phosphate
- 25 µg creatine kinase
- 1 mM of each of the twenty L-amino acids
- 19.3 mM magnesium acetate
- 87.5 µg/ml *E. coli* total tRNA
- 24 % (v/v) of S30 extract from BL21(DE3)
- 186 µg/ml of purified T7 RNAP from BL21(DE3)
- 16 µg/ml plasmid containing amoebapore DNA
- 500 units/ml of RNasin ribonuclease inhibitor (Promega)

Outer buffer:

- Is identical to the cell free reaction mixture excluding the S30 lysate, tRNA, plasmid DNA, T7 RNAP, creatine kinase and RNasin.

7.3.3 S30-ribosome-lysate and T7 RNAP extraction

This step is to extract two of the ingredients for the final cell-free expression mixture. S30-ribosome-lysate and T7 RNA polymerase (RNAP) was extracted from *E. coli* BL21(DE3) cells using the methods described (https://www.embl.de/pepcore/pepcore_services/protein_expression/ecoli/lysate/) with a modification of using a sonicator instead of a french press for cell lysis. The BL21(DE3) *E. coli* strain was used because it contains a copy T7 RNAP and therefore both compounds can be extracted in one experiment.

Briefly, T7-RNAP expression was induced in *E. coli* by adding 1 ml 0.5 M Isopropyl β-D-1-thiogalactopyranoside (IPTG). Cells were grown to optical density (OD) 3 or 4. The pellet was isolated by centrifugation and washed in buffer solutions. Cells were lysed by sonication and the insoluble fraction removed by ultracentrifugation. The supernatant was mixed with preincubation buffer at 37 °C using a roller. The resulting lysate was transferred to a high pure dialysis membrane with molecular weight cut off (MWCO): 5 Da and subject to

dialysis overnight. Lysate is centrifugated and supernatant is stored at -80°C. (method utilised from www.embl.de/pepcore/pepcore_services/protein_expression/ecoli/lysate/). The culture medium of *E. coli* BL21 was used for extraction of S30 lysate. This was done with *E. coli* strain BL21(DE3) as it contained the DE3 lysogen with a copy of T7 RNAP.

One litre culture:

- 5.6 g Potassium dihydrogen phosphate (KH_2PO_4)
- 28.9 g Dibasic potassium phosphate (K_2HPO_4)
- 10 g yeast extract
- 15 mg Thiamine (filtered sterile)
- 40 ml 25% Glucose (filtered sterile)
- DNAse/RNAse-free H_2O

Buffer solutions for S30-ribosome-lysate extraction

Buffer 1:

- 10 mM Tris ($C_4H_{11}NO_3$) pH 8.2
- 60 mM Potassium acetate
- 14 mM Magnesium acetate ($Mg(CH_3CO)_2$)
- 1 mM Dithiothreitol (DTT) ($C_4H_{10}O_2S_2$) (freshly prepared)
- 7 mM 2-Mercaptoethanol (β-ME) (C_2H_6OS) (freshly prepared)

Buffer 2:

- Identical to buffer 1, excluding β-ME

Buffer 3

- Identical to buffer 1, excluding DTT and β-ME

Preincubation Buffer: 750µl required per 1 litre culture

Ingredient	Stock
300 mM Tris Acetyl, pH 7.6	225 µl of 1 M stock
10 mM Magnesium acetate	7.5 µl of 1 M stock

10 mM Adenosine Triphosphate (ATP)   75 µl of 100 mM stock
$C_{10}H_{16}N_5O_{13}P_3$

80 mM Phosphoenol pyruvate (PEP)   60 µl of 1 M stock
$C_3H_4O_6PK$

5 mM DTT   3.75 µl of 1 M stock

40 µM Amino acid mix   6 µl of 5 mM stock

8 U/ml pyruvate kinase   3 µl of 2 U/µl stock

369.75 µl H_2O

Sequence:

- An overnight 10 ml preculture in a 100 ml Erlenmeyer-flask was prepared at 37°C at 250 rpm. This culture was inoculated in 1000 ml medium in a 5000 ml chicanery-flask and grown to OD_{600} 0.8 - 1 at 37°C on 150-180 rpm.
- The T7 RNAP was induced by adding 1 ml of 0.5 M IPTG and grown to OD_{600} 3 – 4.
- A pellet of the culture was obtained by centrifugation (SLA rotor at 6000 g for 30 min, 4°C) and stored at -80°C.

The following steps were performed on ice.

- The pellet was resuspended in buffer 1 (16.6 ml buffer per gram of pellet) by shaking, not pipetting up and down.
- The resuspended pellet centrifugated at 5.000 g for 20 minutes at 4°C and the supernatant discarded.
- This pellet was resuspended, in the same manner as before, in buffer 1 but with 6.6 ml per gram pellet.
- The suspension was centrifugated again at 5.000 g for 20 minutes at 4 °C and the supernatant discarded.
- The pellet was resuspended in buffer 2 (1.3 ml buffer per gram pellet) by shaking and not pipetting up and down.
- The cells were then lysed using a sonicator

142

- The lysate was subjected to ultracentrifugation at 30.000 *g* with a Ti60? rotor for 30 minutes and 4 °C. This produces a large grey-green pellet. The supernatant was transferred to new tubes and centrifugated again to produce a small, clear pellet.
- The supernatant was transferred in to 15 ml tubes using a pipette and incubated in pre-incubation buffer (1 ml buffer per 10 ml lysate) at 37 °C for 90 minutes. The incubation should be performed using a test tube roller in order to keep the liquid in motion (mid-speed) with the tube wrapped in tin foil to prevent light shining on it. This produces a cloudy lysate.
- The lysate was run through a high pure dialysis membrane (without heavy metals or glycerine), with a molecular weight cut off (MWCO): 5.000 Da. It was then subjected to dialysis with buffer 3 (100 ml buffer per 1 ml lysate) for 1 hour at 4 °C. The buffer was replaced and the lysate subjected to dialysis overnight at 4 °C.
- The lysate was transferred into 15 ml tubes and centrifugated at 4.000 *g* for 10 minutes at 4 °C.
- The supernatant was stored in 500 µl aliquots and shock frozen in liquid nitrogen and stored at -80 °C.

7.3.4 Expression & Purification of TEV protease

Protocol provided by Nic Harmer (University of Exeter) using BL21 cells containing pRK793, the plasmid construct containing the TEV protease gene, as previously produced [146]. The S219V strain of TEV protease is used because it is more stable and does not cleave itself as much as wild type TEV protease (Kapust 2001). Cells are grown at 37 °C in LB broth containing 100 µg/ml ampicillin and 30 µg/ml chloramphenicol. When the cells reach mid log phase (OD600 ~ 0.3-0.8), IPTG is added to a final concentration of 1 mM and the temperature reduced to 20 °C overnight with shaking at 180 rpm.

After overnight induction, the cells are collected by centrifugation (4700 *g* on swing bucket rotor 3608 (Thermofisher)). The pellet is resuspended in buffer A and the cells lysed using a sonicator (6 x 25 seconds on and 35 seconds off) at

17 µm amplitude. The solution is mixed by inversion and centrifugated at 24000 g (FI5 rotor) for 30 minutes to separate the soluble and insoluble fractions.

The supernatant is applied to an ÄKTA protein purification system (GE LifeSciences) with a HisTrap™ Fast Flow (FF) crude 1 ml Nickel column (GE Healthcare). Buffer A is used to wash the column, and buffer B for TEV protease elution from the nickel column. A HiLoad 16/600 Superdex™ 200 pg column equilibrated with gel filtration (GF) buffer is used for size exclusion chromatography.

The fractions of interest are run on SDS PAGE using GenScript ExpressPlus™ Bis-tris 4-20 % gel with Tris-MOPS-SDS running buffer (GenScript). The membrane is stained with Coomassie blue (InstantBlue™, Expedeon). The fractions containing only TEV protease are pooled together the TEV protease is stored in aliquots of 1 mg/ml in buffer (10 % glycerol, 2 mM EDTA, 10 mM DTT) and frozen in -80 ºC.

Buffer A:

- 20 mM Tris
- 0.5 M Nacl,
- 20 mM imidazole
- pH 8

Buffer B:

- 20 mM Tris HCL
- 0.5 M NaCl,
- 250 mM imidazole
- pH 8

Gel filtration (GF) buffer:

- 10 mM HEPES,
- 0.5 M NaCl,
- 1 mM EDTA
- 1 mM DTT
- pH 7

One litre culture:

- 5.6 g Potassium dihydrogen phosphate (KH_2PO_4)
- 28.9 g Dibasic potassium phosphate (K_2HPO_4)
- 10 g yeast extract
- 15 mg Thiamine (filtered sterile)
- 40 ml 25% Glucose (filtered sterile)
- DNAse/RNAse-free H_2O

Buffer solutions for S30-ribosome-lysate extraction:

Buffer 1:

- 10 mM Tris ($C_4H_{11}NO_3$)/Acetoxy group (OAc), pH 8.2
- 60 mM Potassium acetate (KOAc)
- 14 mM Magnesium acetate ($Mg(C_2H_3O_2)_2$
- 1 mM Dithiothreitol (DTT) ($C_4H_{10}O_2S_2$) (freshly prepared)
- 7 mM 2-Mercaptoethanol (β-ME) (C_2H_6OS) (freshly prepared)

Buffer 2:

- Identical to buffer 1, excluding β-ME

Buffer 3

- Identical to buffer 1, excluding DTT and β-ME

Preincubation Buffer: 750µl required per 1 litre culture

- 300 mM Tris Acetyl, pH 7.6
- 10 mM Magnesium acetate
- 10 mM Adenosine Triphosphate (ATP) $C_{10}H_{16}N_5O_{13}P_3$
- 80 mM Phosphoenol pyruvate (PEP) $C_3H_4O_6PK$
- 5 mM DTT
- 40 µM Amino acid mix
- 8 U/ml pyruvate kinase
- 369.75 µl H_2O

7.4 Results

7.4.1 Expression & Purification of TEV protease

The TEV protease protein extraction output created several bands of molecular weight 28 kDa (Fig. 7), consistent with TEV protease. A yield of 1.35 mg/ml TEV protease was obtained.
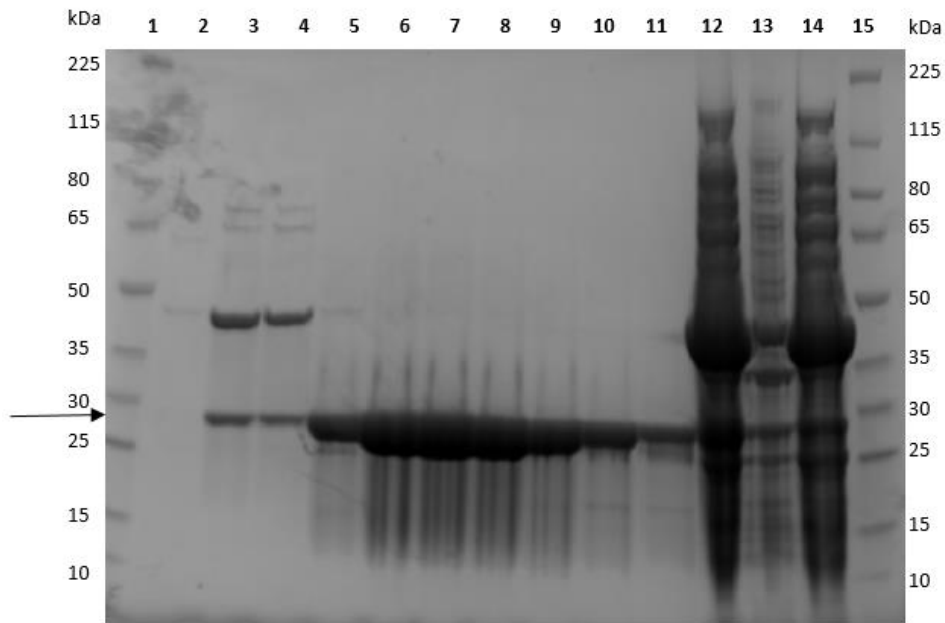
Figure 7.7 SDS PAGE with Coomassie blue staining of protein fractions from E. coli TEV protease expression followed by protein purification using an ÄKTA system with HisTrapTM FF crude nickel column and superdex chromatography column. Molecular weight of TEV protease = 28.6 kDa (indicated by arrow). Lanes 1 and 15: Spectra BR protein ladder, 2-11: fractions of interest eluted from superdex column, 12: soluble fraction of lysed E. coli cells, 13: insoluble fraction of lysed E. coli cells, 14: AKTA flow-through

7.4.2 Cell-free amoebapore expression

- + : positive control (His-tagged protein)
- M: molecular weight ladder
- P: Pellet
- SN: Supernatant
- FT: Flow through
- W1: Wash 1
- W2: Wash 2
- E: Elution (where amoebapore would be)

Amoebapore would be 10 kDa
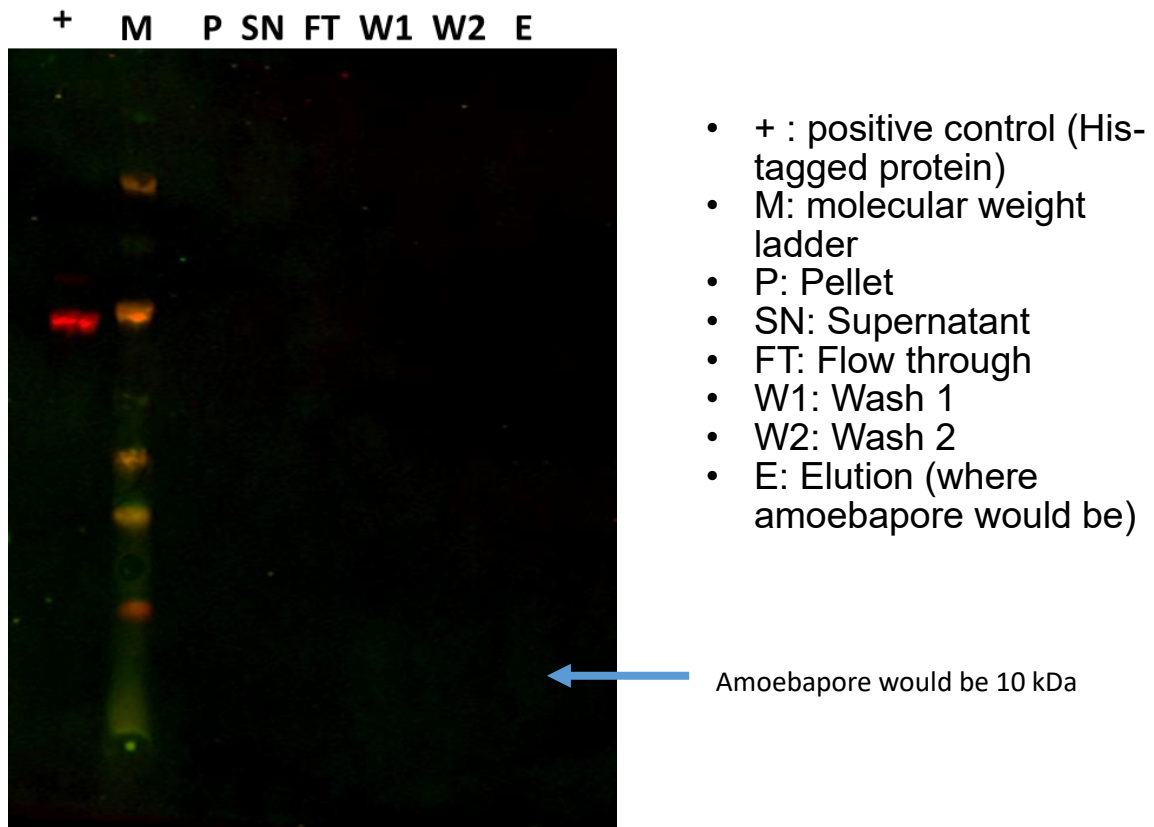
Figure 7.8 Western blot after nickel column protein purification of cell-free expression reaction. Column 1 is a His-tagged positive control to show the western blot protocol worked.
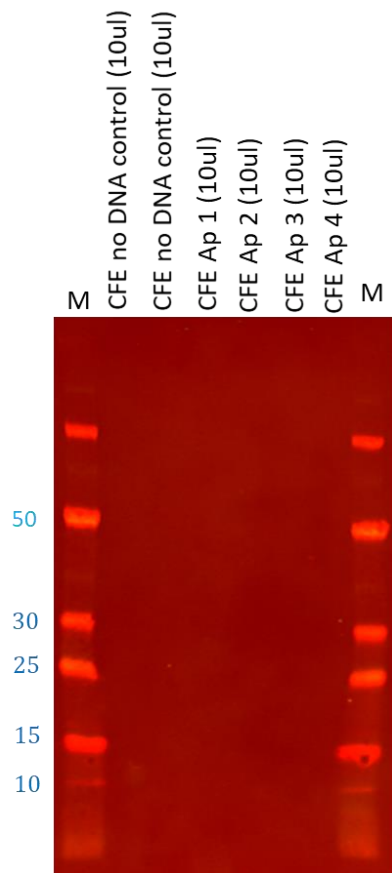
Figure 7.9 Western blot of cell-free expression reactions, before protein purification, with increasing concentrations of plasmid DNA (Ap 1, 2 ng/ul; Ap 2, 5 ng/ul; Ap 3, 10 ng/ul; Ap 4, 15 ng/ul).

7.4.3 Amoebapore expression using E. coli live cells
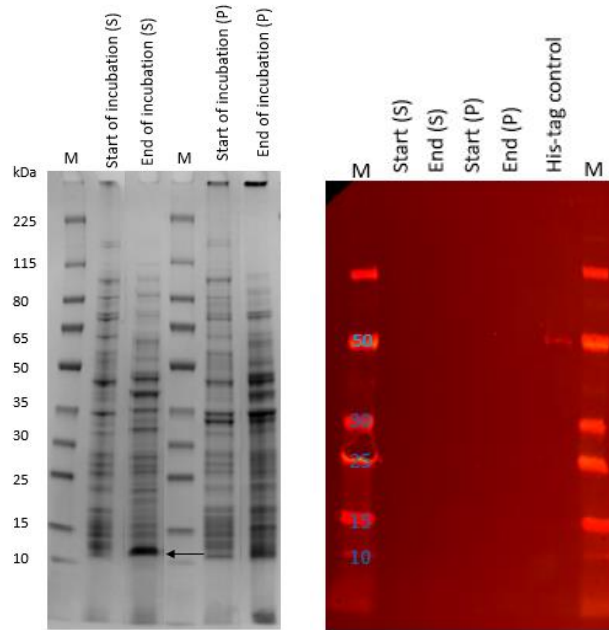
Figure 7.10 On the left, SDS-PAGE analysis of *E. coli* amoebapore expression. On the right, western blot of the same *E. coli* amoebapore expression reactions, probing for His-tagged protein. A control His-tagged protein of molecular weight 50 kDa was used to test success of the western blot protocol.
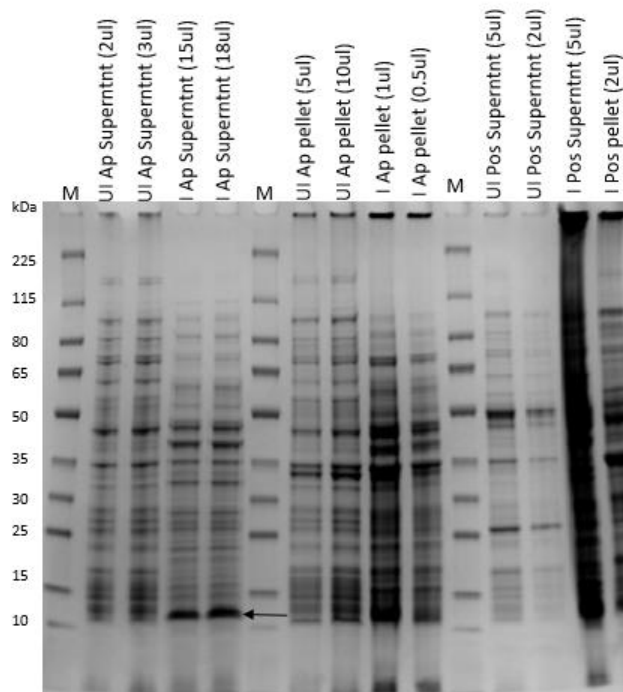
Figure 7.11 SDS-PAGE (4-20 %) analysis of *E. coli* expression of amoebapore. Lanes 2-5 show proteins in the supernatant, lanes 7-10 show those in the cell-lysate pellet and lanes 13-16 show the positive control supernatant and pellet.

7.4.4 Amoebapore expression using cell-free expression kits

7.4.4.i NEB kit PURExpress
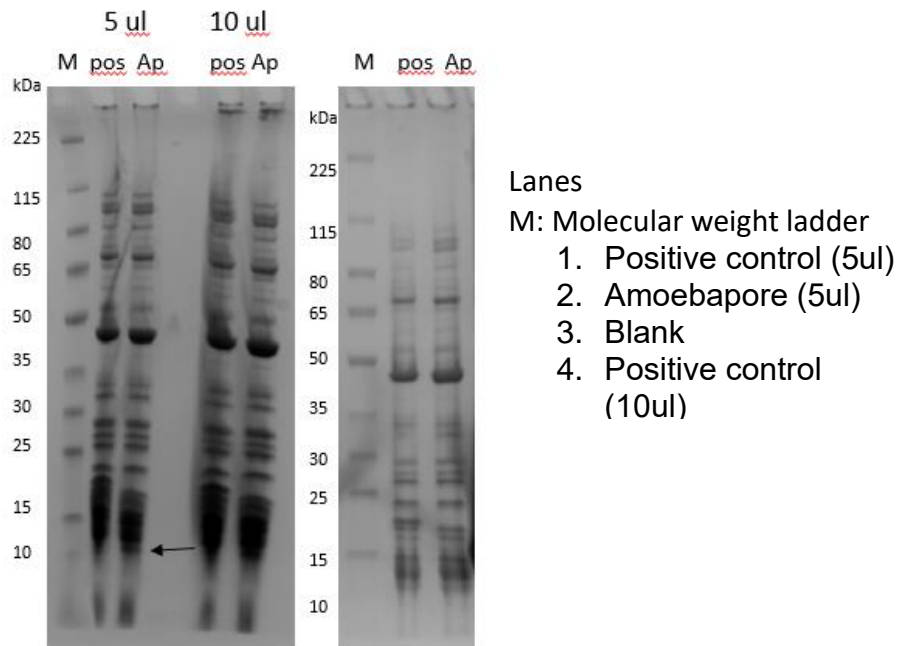
Figure 7.12 Electrophoresis of NEB PURExpress kit reaction on a 4-20 % SDS PAGE gel. The first gel shows the first experiment but with different volumes inserted. The second gel shows the reaction repeated but with an overnight incubation. The positive control can be seen at approx. 18 kDa.

Lanes
M: molecular weight ladder
1: Amoebapore from promega kit (T7 Quick coupled TX/TL)
2: Amoebapore from promega kit (Coupled wheat germ extract system)
3: Amoebapore from promega kit (E. coli T7 S30 extract system for circular DNA)
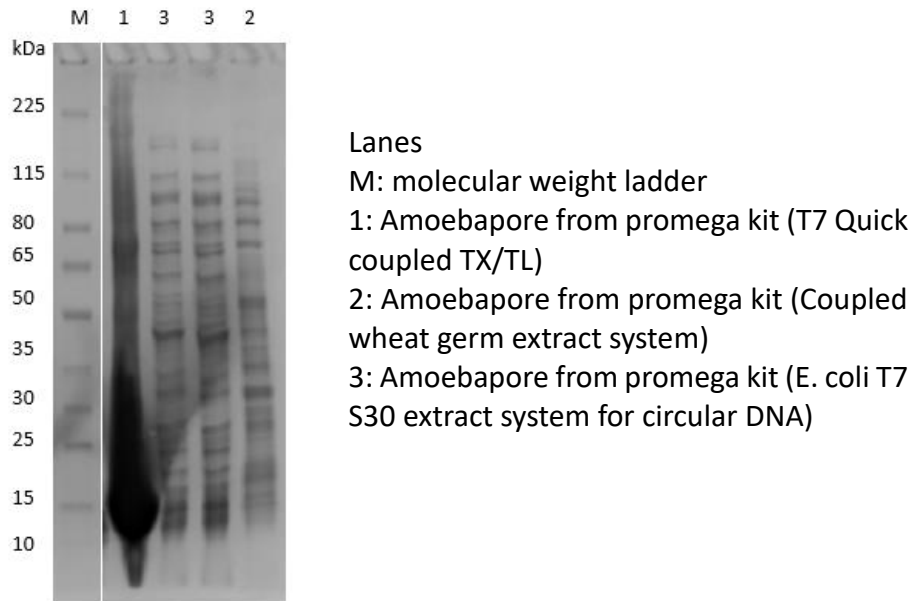
Figure 7.13 SDS-PAGE analysis of Promega T7 samples system cell-free reactions (4-20 % gel).

M: Molecular weight marker
Neg: Negative control
Ap: Amoebapore

← Amoebapore would be 10 kDa
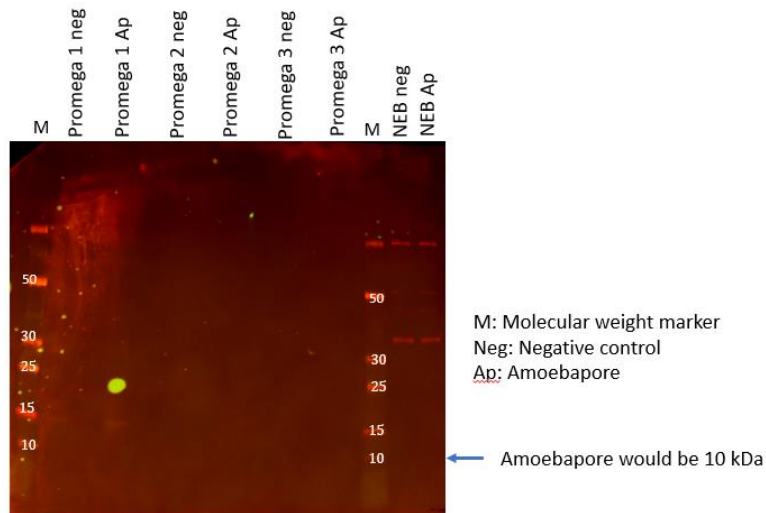
Figure 7.14 Western blot for His-tagged protein of cell-free expression kit reaction mixtures. The Promega negative controls consisted of all the same ingredient mixture but without the DNA. The NEB negative was the mixture with a DNA for a protein of known size (17 kDa) that is not His-tagged and therefore will not show up on the western blot.

7.5 Discussion

7.5.1 Troubleshooting – NEB kit

It is important that the DNA template is pure, with minimal DNases and RNases present (NEB kit manual). It is possible that the expression reaction has not been successful so far because I have not taken steps to purify my plasmid. To clear RNase from plasmid DNA it is recommended to perform a phenol:chloroform extraction and ethanol precipitation (NEB kit manual). Running the template in an agarose gel may show where contaminants are present or if the template has been degraded.

The NEB kit recommends supplementing with a disulphide bond enhancer (e.g. PDBE, NEB #E6820) for the production of proteins that have disulphide bonds. Amoebapore has 3 disulphide bonds and therefore the experiment could have been improved by including this.

Other explanations for no target protein synthesis are provided by the NEB kit manual. These include that the template design is not optimal, for example that the coding and regulatory sequences should be in frame. Another explanation is that the template DNA is contaminated. This could have been tested by mixing the template DNA with the control DNA to see the reaction is then inhibited. The template DNA concentration could also affect the efficiency of reaction with too much causing high concentration of mRNA which may overwhelm the translation molecules (NEB kit manual).

7.5.2 Troubleshooting - TNT® T7 quick coupled TX/TL system (Promega)

This system was one of the two recommended for circular plasmid DNA. This system provides all the ingredients, apart from methionine, for cell-free expression of a plasmid within one tube (TNT® T7 Quick Master Mix). This master mix contains RNA polymerase, nucleotides, amino acids, salts, RNasin, and reticulocyte lysate. The reticulocyte lysate is an extract from mammalian cells, which is one of the main differences between this system and the NEB PURExpress, and the other two Promega systems below. A key difference between E. coli-based and mammalian-based systems is that the latter enables post-transcriptional modification of proteins.

The known post-transcriptional modification of amoebapore A is that some sequence is cleaved off however the amoebapore plasmid construct does not

include the cleavable section and therefore no post-transcriptional modifications are needed.

The cell-free expression kits provide guidelines for the ideal plasmid construct. These guidelines include that there should be approximately 11 base pairs (bp) (TNT® T7 quick coupled TX/TL system manual (Promega)) upstream of the T7 RNA polymerase promotor site. The amoebapore construct has 20 bp before the promotor and therefore fits this guideline. A stop codon is also needed to separate the ribosomes from the RNA and the end of sequence transcription (TNT® T7 quick coupled TX/TL system manual (Promega)). The amoebapore construct contains the stop codon TAA and the end of the target sequence.

The S30 system needs DNA with *E. coli* promotor sequence and a prokaryotic ribosome binding site (GGAGG) (TNT® Coupled Wheat Germ Extract manual (Promega)). The amoebapore plasmid, pET9a, has a ribosome binding site of AAGGAG which is from the phage T7 major capsid protein (Novagen pET system manual). The T7 phage gene ribosome binding site has been found to enable higher production of foreign genes in *E. coli* [147, 148]. As these genes were still expressed in *E. coli* it is therefore a prokaryotic system and so this phage ribosome binding site should be appropriate for the S30 system.

7.5.3 Conclusion

The protocol for cell-free amoebapore expression was designed and several unsuccessful variations tested. The TEV protease, a protein needed in the final stages of protein purification of amoebapore, had been successfully isolated from *E. coli* cells. It can be seen from the protein gel (Fig. 7) that the protein has a high level of purity.

The amoebapore expression plasmid was designed and ordered through Genscript and transformed into *E. coli* cells (without inducing protein production) to obtain a high yield store of the plasmid, which is now stored in the Mark van der Giezen laboratory.

As no amoebapore was detected in any of the experiments, this work was stopped and work on the other *E. histolytica* virulence factor, chitosan, became the main focus of this part of the thesis.

8 <u>References</u>

1. Lombard, J., *Once upon a time the cell membranes: 175 years of cell boundary research.* Biology direct, 2014. **9**(1): p. 1-35.
2. Singer, S.J. and G.L. Nicolson, *The fluid mosaic model of the structure of cell membranes.* Science, 1972. **175**(4023): p. 720-731.
3. Bezanilla, M., et al., *Cytoskeletal dynamics: a view from the membrane.* Journal of Cell Biology, 2015. **209**(3): p. 329-337.
4. Roberts, K., et al., *Molecular biology of the cell.* New York: Garland Science, 2002.
5. Quinn, P.J., *Plasma membrane phospholipid asymmetry*, in *Phospholipid Metabolism in Apoptosis*. 2004, Springer. p. 39-60.
6. Kuypers, F.A., *Membrane lipid alterations in hemoglobinopathies.* ASH Education Program Book, 2007. **2007**(1): p. 68-73.
7. Yeagle, P.L., *The Lipids of Biological Membranes*, in *The membranes of cells*, P.L. Yeagle, Editor. 2016, Academic Press.
8. Borrell, J.H., Ò. Domènech, and K.M. Keough, *Membrane Protein–Lipid Interactions: Physics and Chemistry in the Bilayer*. 2016: Springer.
9. Zhao, H. and P. Lappalainen, *A simple guide to biochemical approaches for analyzing protein–lipid interactions.* Molecular biology of the cell, 2012. **23**(15): p. 2823-2830.
10. Peetla, C., S. Vijayaraghavalu, and V. Labhasetwar, *Biophysics of cell membrane lipids in cancer drug resistance: implications for drug transport and drug delivery with nanoparticles.* Advanced drug delivery reviews, 2013. **65**(13): p. 1686-1698.
11. Redwood, W., et al., *Physical properties of bilayer membranes formed from a synthetic saturated phospholipid in n-decane.* Biochimica et Biophysica Acta (BBA)-Biomembranes, 1971. **233**(1): p. 1-6.
12. Wang, L., *Measurements and implications of the membrane dipole potential.* Annual review of biochemistry, 2012. **81**: p. 615-635.
13. Dupuy, A.D. and D.M. Engelman, *Protein area occupancy at the center of the red blood cell membrane.* Proceedings of the National Academy of Sciences, 2008. **105**(8): p. 2848-2852.
14. Pratt, L.R. and D. Chandler, *Theory of the hydrophobic effect.* The Journal of chemical physics, 1977. **67**(8): p. 3683-3704.
15. Tanford, C., *The hydrophobic effect and the organization of living matter.* Science, 1978. **200**(4345): p. 1012-1018.
16. Sonnino, S. and A. Prinetti, *Membrane domains and the "lipid raft" concept.* Current medicinal chemistry, 2013. **20**(1): p. 4-21.
17. Simons, K. and J.L. Sampaio, *Membrane organization and lipid rafts.* Cold Spring Harbor perspectives in biology, 2011. **3**(10): p. a004697.
18. Bischofberger, M., I. Iacovache, and F.G. van der Goot, *Pathogenic pore-forming proteins: function and host response.* Cell host & microbe, 2012. **12**(3): p. 266-275.

19. Gleason, T.G., et al., *Hemolytically active (acylated) alpha-hemolysin elicits interleukin-1β (IL-1β) but augments the lethality of Escherichia coli by an IL-1-and tumor necrosis factor-independent mechanism.* Infection and immunity, 1998. **66**(9): p. 4215-4221.

20. Derrick, S.C. and S.L. Morris, *The ESAT6 protein of Mycobacterium tuberculosis induces apoptosis of macrophages by activating caspase expression.* Cellular microbiology, 2007. **9**(6): p. 1547-1555.

21. del Mar García-Suárez, M., et al., *The role of pneumolysin in mediating lung damage in a lethal pneumococcal pneumonia murine model.* Respiratory research, 2007. **8**(1): p. 1.

22. WHO, *Antimicrobial resistance global report on surveillance: 2014 summary.* World Health Organisation, 2014.

23. Klopper, M., et al., *Emergence and spread of extensively and totally drug-resistant tuberculosis, South Africa.* Emergence, 2013.

24. Samarawickrema, N., et al., *Involvement of superoxide dismutase and pyruvate: ferredoxin oxidoreductase in mechanisms of metronidazole resistance in Entamoeba histolytica.* Journal of Antimicrobial Chemotherapy, 1997. **40**(6): p. 833-840.

25. Law, R.H., et al., *The structural basis for membrane binding and pore formation by lymphocyte perforin.* Nature, 2010. **468**(7322): p. 447-451.

26. Rojko, N. and G. Anderluh, *How lipid membranes affect pore forming toxin activity.* Accounts of chemical research, 2015. **48**(12): p. 3073-3079.

27. Bokori-Brown, M., et al., *Red Blood Cell Susceptibility to Pneumolysin CORRELATION WITH MEMBRANE BIOCHEMICAL AND PHYSICAL PROPERTIES.* Journal of Biological Chemistry, 2016. **291**(19): p. 10210-10227.

28. Israelachvili, J., S. Marcelja, and R. Horn, *Physical principles of membrane organization.* Q. Rev. Biophys, 1980. **13**(2): p. 121-200.

29. Leung, C., et al., *Stepwise visualization of membrane pore formation by suilysin, a bacterial cholesterol-dependent cytolysin.* Elife, 2014. **3**: p. e04247.

30. Sonnen, A.F.-P., J.M. Plitzko, and R.J. Gilbert, *Incomplete pneumolysin oligomers form membrane pores.* Open biology, 2014. **4**(4): p. 140044.

31. Songer, J.G., *Clostridial enteric diseases of domestic animals.* Clinical microbiology reviews, 1996. **9**(2): p. 216.

32. McDonel, J.L., *Clostridium perfringens toxins (type a, b, c, d, e).* Pharmacology & therapeutics, 1980. **10**(3): p. 617-655.

33. Petit, L., M. Gibert, and M.R. Popoff, *Clostridium perfringens: toxinotype and genotype.* Trends in microbiology, 1999. **7**(3): p. 104-110.

34. Rumah, K.R., et al., *Isolation of Clostridium perfringens type B in an individual at first clinical presentation of multiple sclerosis provides clues for environmental triggers of the disease.* PloS one, 2013. **8**(10): p. e76359.

35. Rumah, K.R., et al., *The myelin and lymphocyte protein MAL is required for binding and activity of Clostridium perfringens ε-toxin.* PLoS pathogens, 2015. **11**(5): p. e1004896.

36. Wagley, S., et al., *Evidence of Clostridium perfringens epsilon toxin associated with multiple sclerosis.* Multiple Sclerosis Journal, 2019. **25**(5): p. 653-660.

37. Bokori-Brown, M., et al., *Molecular basis of toxicity of Clostridium perfringens epsilon toxin.* The FEBS journal, 2011. **278**(23): p. 4589-4601.

38. Popoff, M.R., *Clostridial pore-forming toxins: powerful virulence factors.* Anaerobe, 2014. **30**: p. 220-238.

39. Knapp, O., B. Stiles, and M. Popoff, *The aerolysin-like toxin family of cytolytic, pore-forming toxins.* 2010.

40. Petit, L., et al., *Clostridium perfringens epsilon toxin induces a rapid change of cell membrane permeability to ions and forms channels in artificial lipid bilayers.* Journal of Biological chemistry, 2001. **276**(19): p. 15736-15740.

41. Petit, L., et al., *Clostridium perfringens epsilon-toxin acts on MDCK cells by forming a large membrane complex.* Journal of bacteriology, 1997. **179**(20): p. 6480-6487.

42. Savva, C.G., et al., *The pore structure of Clostridium perfringens epsilon toxin.* Nature communications, 2019. **10**(1): p. 2641.

43. Cole, A.R., et al., *Clostridium perfringens ε-toxin shows structural similarity to the pore-forming toxin aerolysin.* Nature structural & molecular biology, 2004. **11**(8): p. 797-798.

44. Parker, M.W. and S.C. Feil, *Pore-forming protein toxins: from structure to function.* Progress in biophysics and molecular biology, 2005. **88**(1): p. 91-142.

45. Bokori-Brown, M., et al., *Clostridium perfringens epsilon toxin H149A mutant as a platform for receptor binding studies.* Protein Science, 2013. **22**(5): p. 650-659.

46. Ivie, S.E. and M.S. McClain, *Identification of amino acids important for binding of Clostridium perfringens epsilon toxin to host cells and to HAVCR1.* Biochemistry, 2012. **51**(38): p. 7588-7595.

47. Alves, G.G., et al., *Clostridium perfringens epsilon toxin: the third most potent bacterial toxin known.* Anaerobe, 2014. **30**: p. 102-107.

48. Miyata, S., et al., *Clostridium perfringens ε-toxin forms a heptameric pore within the detergent-insoluble microdomains of Madin-Darby canine kidney cells and rat synaptosomes.* Journal of Biological chemistry, 2002. **277**(42): p. 39463-39468.

49. Ivie, S.E., et al., *Gene-trap mutagenesis identifies mammalian genes contributing to intoxication by Clostridium perfringens ε-toxin.* PloS one, 2011. **6**(3): p. e17787.

50. Millan, J., et al., *The MAL proteolipid is a component of the detergent-insoluble membrane subdomains of human T-lymphocytes.* Biochemical Journal, 1997. **321**(1): p. 247-252.

51. Caduff, J., et al., *Characterization of GFP-MAL expression and incorporation in rafts.* Microscopy research and technique, 2001. **52**(6): p. 645-655.

52.   Gao, J., et al., *Hemolysis in human erythrocytes by Clostridium perfringens epsilon toxin requires activation of P2 receptors.* Virulence, 2018. **9**(1): p. 1601-1614.

53.   Fischetti, V.A. and K.R. Rumah, *Human blood exposure to Clostridium perfringens epsilon toxin may shed light on erythrocyte fragility during active multiple sclerosis.* bioRxiv, 2019: p. 789123.

54.   Geng, Z., et al., *Clostridium perfringens epsilon toxin binds to erythrocyte MAL receptors and triggers phosphatidylserine exposure.* Journal of cellular and molecular medicine, 2020. **24**(13): p. 7341-7352.

55.   Nagahama, M., et al., *Oligomerization of Clostridium perfringens ε-toxin is dependent upon membrane fluidity in liposomes.* Biochemistry, 2006. **45**(1): p. 296-302.

56.   Nestorovich, E.M., V.A. Karginov, and S.M. Bezrukov, *Polymer partitioning and ion selectivity suggest asymmetrical shape for the membrane pore formed by epsilon toxin.* Biophysical journal, 2010. **99**(3): p. 782-789.

57.   Das, S., et al., *The cyst wall of Entamoeba invadens contains chitosan (deacetylated chitin).* Molecular and biochemical parasitology, 2006. **148**(1): p. 86-92.

58.   Tsigos, I., et al., *Chitin deacetylases: new, versatile tools in biotechnology.* Trends in biotechnology, 2000. **18**(7): p. 305-312.

59.   Elsabee, M.Z., R.E. Morsi, and A. Al-Sabagh, *Surface active properties of chitosan and its derivatives.* Colloids and Surfaces B: Biointerfaces, 2009. **74**(1): p. 1-16.

60.   Wang, Q.Z., et al., *Protonation constants of chitosan with different molecular weight and degree of deacetylation.* Carbohydrate polymers, 2006. **65**(2): p. 194-201.

61.   Pavinatto, A., F.J. Pavinatto, and A. Barros-Timmons, *Electrostatic interactions are not sufficient to account for chitosan bioactivity.* ACS applied materials & interfaces, 2010. **2**(1): p. 246-251.

62.   Goy, R.C., D.d. Britto, and O.B. Assis, *A review of the antimicrobial activity of chitosan.* Polímeros, 2009. **19**(3): p. 241-247.

63.   Zhou, X., et al., *An investigation of chitosan and its derivatives on red blood cell agglutination.* RSC advances, 2017. **7**(20): p. 12247-12254.

64.   Ylitalo, R., et al., *Cholesterol-lowering properties and safety of chitosan.* Arzneimittelforschung, 2002. **52**(1): p. E1.

65.   Wydro, P., B. Krajewska, and K. Hac-Wydro, *Chitosan as a lipid binder: a Langmuir monolayer study of chitosan– lipid interactions.* Biomacromolecules, 2007. **8**(8): p. 2611-2617.

66.   Pavinatto, F.J., et al., *Probing chitosan and phospholipid interactions using Langmuir and Langmuir– Blodgett films as cell membrane models.* Langmuir, 2007. **23**(14): p. 7666-7671.

67.   Krajewska, B., P. Wydro, and A. Kyzioł, *Chitosan as a subphase disturbant of membrane lipid monolayers. The effect of temperature at varying pH: I. DPPG.* Colloids and Surfaces A: Physicochemical and Engineering Aspects, 2013. **434**: p. 349-358.

68. Krajewska, B., A. Kyzioł, and P. Wydro, *Chitosan as a subphase disturbant of membrane lipid monolayers. The effect of temperature at varying pH: II. DPPC and cholesterol.* Colloids and Surfaces A: Physicochemical and Engineering Aspects, 2013. **434**: p. 359-364.

69. Pavinatto, F.J., D.S.d. Santos Jr, and O.N. Oliveira Jr, *Interaction between cholesterol and chitosan in Langmuir monolayers.* Polímeros, 2005. **15**: p. 91-94.

70. Pavinatto, A., et al., *Experimental evidence for the mode of action based on electrostatic and hydrophobic forces to explain interaction between chitosans and phospholipid Langmuir monolayers.* Colloids and Surfaces B: Biointerfaces, 2016. **145**: p. 201-207.

71. de Oliveira Pedro, R., et al., *Interaction of chitosan derivatives with cell membrane models in a biologically relevant medium.* Colloids and Surfaces B: Biointerfaces, 2020: p. 111048.

72. Pavinatto, F.J., et al., *Interaction of chitosan with cell membrane models at the air– water interface.* Biomacromolecules, 2007. **8**(5): p. 1633-1640.

73. Betts, M.J. and R.B. Russell, *Amino acid properties and consequences of substitutions.* Bioinformatics for geneticists, 2003. **317**: p. 289.

74. Sherman, F., J.W. Stewart, and S. Tsunasawa, *Methionine or not methionine at the beginning of a protein.* Bioessays, 1985. **3**(1): p. 27-31.

75. Minami, J., et al., *Lambda-toxin of Clostridium perfringens activates the precursor of epsilon-toxin by releasing its N-and C-terminal peptides.* Microbiology and immunology, 1997. **41**(7): p. 527-535.

76. Fedosov, D.A., B. Caswell, and G.E. Karniadakis. *Coarse-grained red blood cell model with accurate mechanical properties, rheology and dynamics*. in *2009 Annual International Conference of the IEEE Engineering in Medicine and Biology Society*. 2009. IEEE.

77. Hale, J.P., C.P. Winlove, and P.G. Petrov, *Effect of hydroperoxides on red blood cell membrane mechanical properties.* Biophysical journal, 2011. **101**(8): p. 1921-1929.

78. Hale, J.P., et al., *Red blood cell thermal fluctuations: comparison between experiment and molecular dynamics simulations.* Soft Matter, 2009. **5**(19): p. 3603-3606.

79. Jewell, S.A., et al., *Clostridium perfringens α-toxin interaction with red cells and model membranes.* Soft matter, 2015. **11**(39): p. 7748-7761.

80. Jewell, S., P. Petrov, and C. Winlove, *The effect of oxidative stress on the membrane dipole potential of human red blood cells.* Biochimica et Biophysica Acta (BBA)-Biomembranes, 2013. **1828**(4): p. 1250-1258.

81. Bokori-Brown, M., et al., *Interactions between Pseudomonas immunotoxins and the plasma membrane: Implications for CAT-8015 immunotoxin therapy.* Frontiers in oncology, 2018. **8**: p. 553.

82. Mueller, P., et al., *Reconstitution of excitable cell membrane structure in vitro.* Circulation, 1962. **26**(5): p. 1167-1171.

83. Montal, M. and P. Mueller, *Formation of bimolecular membranes from lipid monolayers and a study of their electrical properties.* Proceedings of the National Academy of Sciences, 1972. **69**(12): p. 3561-3566.

84. Yeagle, P., *Laboratory Membrane Systems*, in *The Membranes of Cells*, P. Yeagle, Editor. 2016, Academic Press: USA. p. 95-113.

85. Moehwald, H. and G. Brezesinski, *From Langmuir Monolayers to Multilayer Films.* Langmuir, 2016.

86. Dynarowicz-Łątka, P., A. Dhanabalan, and O.N. Oliveira, *Modern physicochemical research on Langmuir monolayers.* Advances in colloid and interface science, 2001. **91**(2): p. 221-293.

87. Lösche, M., H.-P. Duwe, and H. Möhwald, *Quantitative analysis of surface textures in phospholipid monolayer phase transitions.* Journal of colloid and interface science, 1988. **126**(2): p. 432-444.

88. Janmey, P. and P. Kinnunen, *Biophysical properties of lipids and dynamic membranes.* Trends in cell biology, 2006. **16**(10): p. 538-546.

89. Stottrup, B.L., D.S. Stevens, and S.L. Keller, *Miscibility of ternary mixtures of phospholipids and cholesterol in monolayers, and application to bilayer systems.* Biophysical journal, 2005. **88**(1): p. 269-276.

90. Demel, R., et al., *Relation between various phospholipase actions on human red cell membranes and the interfacial phospholipid pressure in monolayers.* Biochimica et Biophysica Acta (BBA)-Biomembranes, 1975. **406**(1): p. 97-107.

91. Marsh, D., *Lateral pressure in membranes.* Biochimica et Biophysica Acta (BBA)-Reviews on Biomembranes, 1996. **1286**(3): p. 183-223.

92. Boumann, H.A., et al., *Biophysical properties of membrane lipids of anammox bacteria: II. Impact of temperature and bacteriohopanoids.* Biochimica et Biophysica Acta (BBA)-Biomembranes, 2009. **1788**(7): p. 1452-1457.

93. Virtanen, J.A., K.H. Cheng, and P. Somerharju, *Phospholipid composition of the mammalian red cell membrane can be rationalized by a superlattice model.* Proceedings of the National Academy of Sciences, 1998. **95**(9): p. 4964-4969.

94. Georgiev, G.A., et al., *Surface relaxations as a tool to distinguish the dynamic interfacial properties of films formed by normal and diseased meibomian lipids.* Soft Matter, 2014. **10**(30): p. 5579-5588.

95. Tschoegl, N., *The Phenomenological Theory of Linear Viscoelastic Behaviour An Introduction Springer-Verlag.* New York, 1989.

96. Nencheva, Y., et al., *Effects of lipid saturation on the surface properties of human meibum films.* International journal of molecular sciences, 2018. **19**(8): p. 2209.

97. Yasaka, M., *X-ray thin-film measurement techniques.* The Rigaku Journal, 2010. **26**(2): p. 1-9.

98. Konovalov, O. *ID10 beamline overview*. [cited 2021; ID10EH1 overview]. Available from:

http://www.esrf.eu/UsersAndScience/Experiments/SoftMatter/ID10/ID10 EH1/BeamlineOverview.

99. Gibaud, A., Vignaud, G., *Specular Reflectivity from Smooth and Rough Surfaces*, in *X-ray and Neutron Reflectivity, Principles and Applications, Lecture Notes in Physics*, J. Daillant, Gibaud, Alain., Editor. 2009, Springer: Berlin Heidelberg. p. 85-131.

100. Als-Nielsen, J., et al., *Principles and applications of grazing incidence x-ray and neutron scattering from ordered molecular monolayers at the air-water interface.* Physics Reports, 1994. **246**(5): p. 254.

101. Helm, C., et al., *Phases of phosphatidyl ethanolamine monolayers studied by synchrotron x-ray scattering.* Biophysical journal, 1991. **60**(6): p. 1457-1476.

102. Jensen, T.R., et al., *Novel methods for studying lipids and lipases and their mutual interaction at interfaces. Part II. Surface sensitive synchrotron X-ray scattering.* Biochimie, 2001. **83**(5): p. 399-408.

103. Kaganer, V.M., H. Möhwald, and P. Dutta, *Structure and phase transitions in Langmuir monolayers.* Reviews of Modern Physics, 1999. **71**(3): p. 779.

104. Gologan, P., *Red blood cell as an elastic probe: interaction with drugs and toxins.* 2013.

105. Goh, J.B. and S.K. Ng, *Impact of host cell line choice on glycan profile.* Critical reviews in biotechnology, 2018. **38**(6): p. 851-867.

106. Claesson, P.M., et al., *Direct measurement of temperature-dependent interactions between non-ionic surfactant layers.* Journal of the Chemical Society, Faraday Transactions 1: Physical Chemistry in Condensed Phases, 1986. **82**(9): p. 2735-2746.

107. Hawkins, R.J. and T.C. McLeish, *Coupling of global and local vibrational modes in dynamic allostery of proteins.* Biophysical journal, 2006. **91**(6): p. 2055-2062.

108. Cirauqui, N., et al., *Structural, physicochemical and dynamic features conserved within the aerolysin pore-forming toxin family.* Scientific reports, 2017. **7**(1): p. 1-12.

109. Tristram-Nagle, S., et al., *Structure and water permeability of fully hydrated diphytanoylPC.* Chemistry and physics of lipids, 2010. **163**(6): p. 630-637.

110. Degiacomi, M.T., et al., *Molecular assembly of the aerolysin pore reveals a swirling membrane-insertion mechanism.* Nature chemical biology, 2013. **9**(10): p. 623-629.

111. Iacovache, I., et al., *Dual chaperone role of the C-terminal propeptide in folding and oligomerization of the pore-forming toxin aerolysin.* PLoS Pathog, 2011. **7**(7): p. e1002135.

112. Georgiev, G.A., et al., *Surface chemistry interactions of cationorm with films by human meibum and tear film compounds.* International journal of molecular sciences, 2017. **18**(7): p. 1558.

113. Leekumjorn, S. and A.K. Sum, *Molecular simulation study of structural and dynamic properties of mixed DPPC/DPPE bilayers.* Biophysical journal, 2006. **90**(11): p. 3951-3965.

114. Dyck, M., P. Krüger, and M. Lösche, *Headgroup organization and hydration of methylated phosphatidylethanolamines in Langmuir monolayers.* Physical Chemistry Chemical Physics, 2005. **7**(1): p. 150-156.

115. García-Sáez, A.J., S. Chiantia, and P. Schwille, *Effect of line tension on the lateral organization of lipid membranes.* Journal of Biological Chemistry, 2007. **282**(46): p. 33537-33544.

116. Pavinatto, A., F.J. Pavinatto, and A. Barros-Timmons, *Electrostatic interactions are not sufficient to account for chitosan bioactivity.* ACS applied materials & interfaces, 2009. **2**(1): p. 246-251.

117. Majewski, J. and B. Stec, *X-ray scattering studies of model lipid membrane interacting with purothionin provide support for a previously proposed mechanism of membrane lysis.* European biophysics journal, 2010. **39**(8): p. 1155-1165.

118. Epand, R.M., *Hydrogen bonding and the thermotropic transitions of phosphatidylethanolamines.* Chemistry and physics of lipids, 1990. **52**(3-4): p. 227-230.

119. Chen, X., et al., *Reorganization and caging of DPPC, DPPE, DPPG, and DPPS monolayers caused by dimethylsulfoxide observed using Brewster angle microscopy.* Langmuir, 2010. **26**(24): p. 18902-18908.

120. Leekumjorn, S. and A. Sum, *Molecular investigation of the interactions of trehalose with lipid bilayers of DPPC, DPPE and their mixture.* Molecular Simulation, 2006. **32**(3-4): p. 219-230.

121. Dahmen-Levison, U., G. Brezesinski, and H. Möhwald, *Specific adsorption of PLA2 at monolayers.* Thin Solid Films, 1998. **327**: p. 616-620.

122. Lozano, R., et al., *Global and regional mortality from 235 causes of death for 20 age groups in 1990 and 2010: a systematic analysis for the Global Burden of Disease Study 2010.* The Lancet, 2013. **380**(9859): p. 2095-2128.

123. Ackers, J., et al., *WHO/PAHO/UNESCO report. A consultation with experts on amoebiasis. Mexico City, Mexico 28–29 January, 1997.* Epidemiol. Bull. PAHO, 1997. **18**: p. 13-14.

124. Ross, A.G., et al., *Enteropathogens and chronic illness in returning travelers.* New England Journal of Medicine, 2013. **368**(19): p. 1817-1825.

125. Stanley, S.L., *Amoebiasis.* The Lancet, 2003. **361**(9362): p. 1025-1034.

126. Leippe, M., et al., *Amoebapores, a family of membranolytic peptides from cytoplasmic granules of Entamoeba histolytica: isolation, primary structure, and pore bacterial cytoplasmic membranes.* Molecular microbiology, 1994. **14**(5): p. 895-904.

127. Leippe, M., et al., *Primary and secondary structure of the pore-forming peptide of pathogenic Entamoeba histolytica.* The EMBO journal, 1992. **11**(10): p. 3501.

128. Gupta, S.S., et al., *Acute fulminant necrotizing amoebic colitis: a rare and fatal complication of amoebiasis: a case report.* Cases journal, 2009. **2**(1): p. 1.

129. Aristizábal, H., J. Acevedo, and M. Botero, *Fulminant amebic colitis.* World journal of surgery, 1991. **15**(2): p. 216-221.

130. Ellyson, J.H., et al., *Necrotizing amebic colitis: a frequently fatal complication.* The American journal of surgery, 1986. **152**(1): p. 21-26.

131. Takahashi, T., et al., *Fulminant amebic colitis.* Diseases of the colon & rectum, 1997. **40**(11): p. 1362-1367.

132. Knobloch, J. and E. Mannweiler, *Development and persistence of antibodies to Entamoeba histolytica in patients with amebic liver abscess. Analysis of 216 cases.* The American journal of tropical medicine and hygiene, 1983. **32**(4): p. 727-732.

133. Dhawan, V.K. *Amebiasis Workup.* 2016 24.03.16 [cited 2016 15.12.16]; Available from: http://emedicine.medscape.com/article/212029-workup.

134. Young, J.D.E. and Z.A. Cohn, *Molecular mechanisms of cytotoxicity mediated by Entamoeba histolytica: Characterization of a pore-forming protein (PFP).* Journal of cellular biochemistry, 1985. **29**(4): p. 299-308.

135. Gitler, C., E. Calef, and I. Rosenberg, *Cytopathogenicity of Entamoeba histolytica.* Philosophical Transactions of the Royal Society of London B: Biological Sciences, 1984. **307**(1131): p. 73-85.

136. Bracha, R., et al., *Antisense inhibition of amoebapore expression in Entamoeba histolytica causes a decrease in amoebic virulence.* Molecular microbiology, 1999. **34**(3): p. 463-472.

137. Bracha, R., Y. Nuchamowitz, and D. Mirelman, *Transcriptional silencing of an amoebapore gene in Entamoeba histolytica: molecular analysis and effect on pathogenicity.* Eukaryotic cell, 2003. **2**(2): p. 295-305.

138. Rosenberg, I., et al., *Isolation, characterization and partial purification of a transferable membrane channel (amoebapore) produced by Entamoeba histolytica.* Molecular and biochemical parasitology, 1989. **33**(3): p. 237-247.

139. Petri Jr, W., et al., *Isolation of the galactose-binding lectin that mediates the in vitro adherence of Entamoeba histolytica.* Journal of Clinical Investigation, 1987. **80**(5): p. 1238.

140. Ravdin, J.I. and R.L. Guerrant, *Role of adherence in cytopathogenic mechanisms of Entamoeba histolytica: study with mammalian tissue culture cells and human erythrocytes.* Journal of Clinical Investigation, 1981. **68**(5): p. 1305.

141. Andrä, J. and M. Leippe, *Pore-forming peptide of Entamoeba histolytica significance of positively charged amino acid residues for its mode of action.* FEBS letters, 1994. **354**(1): p. 97-102.

142. Hecht, O., et al., *Solution structure of the pore-forming protein of Entamoeba histolytica.* Journal of Biological Chemistry, 2004. **279**(17): p. 17834-17841.

143. Leippe, M., et al., *Ancient weapons: the three-dimensional structure of amoebapore A.* Trends in parasitology, 2005. **21**(1): p. 5-7.

144. Leippe, M., et al., *Pore-forming peptide of pathogenic Entamoeba histolytica.* Proceedings of the National Academy of Sciences, 1991. **88**(17): p. 7659-7663.

145. Xun, Y., et al., *Cell-free synthesis and combinatorial selective 15 N-labeling of the cytotoxic protein amoebapore A from Entamoeba histolytica.* Protein expression and purification, 2009. **68**(1): p. 22-27.

146. Kapust, R.B., et al., *Tobacco etch virus protease: mechanism of autolysis and rational design of stable mutants with wild-type catalytic proficiency.* Protein engineering, 2001. **14**(12): p. 993-1000.

147. Olins, P.O. and S. Rangwala, *A novel sequence element derived from bacteriophage T7 mRNA acts as an enhancer of translation of the lacZ gene in Escherichia coli.* Journal of Biological Chemistry, 1989. **264**(29): p. 16973-16976.

148. Olins, P.O., et al., *The T7 phage gene 10 leader RNA, a ribosome-binding site that dramatically enhances the expression of foreign genes in Escherichia coli.* Gene, 1988. **73**(1): p. 227-235.